2017

RENEWABLE CARBON FROM LIGNIN BIOMASS AND ITS ELECTRODE AND CATALYST APPLICATIONS IN BATTERIES, SUPERCAPACITORS, AND FUEL CELLS

muslum demir

RENEWABLE CARBON FROM LIGNIN BIOMASS AND ITS ELECTRODE AND CATALYST APPLICATIONS IN BATTERIES, SUPERCAPACITORS, AND FUEL CELLS

A dissertation submitted in partial fulfillment of the requirements for the degree of Doctor of Philosophy at Virginia Commonwealth University.

by

MUSLUM DEMIR,

(M.Sc.) Rutgers University, USA, (2013)

Director: Ram B. Gupta, Professor,
Department of Chemical and Life Science Engineering

Virginia Commonwealth University
Richmond, Virginia
August 2017

Acknowledges and Dedication

Thanks to almighty ALLAH for his great mercy and accommodation that empowered me to get this work accomplished.

Through the studying at VCU and Auburn, there are many things happen in my life worthy memory, novel, happiness or sadness, whatever they are all my precious fortunes. The most important thing is that I met many people and made some good friends, they are giving me a lot of help and. Here I would like to give my sincere appreciation to them.

First and foremost I should thank my advisor, Dr. Ram B. Gupta. Through my application for Ph.D. position at Auburn than at VCU, choosing my Ph.D. plan, preparing the proposal until finalizing my dissertation, he has been poured a lot of works along with all my journeys. His perceptiveness and sharp intuition in academic not only make my work novelty but also make me feel that it is interesting and accessible. I always know where I should go with his guide. I am benefited not just from his academic capability which extending to his great personalities. His hard working, tolerance, and understanding always make my work easier and more important is that he has been setting a great example for us.

In addition to, I am very grateful to Dr. Hani El- Kaderi. He offered a lot of opportunities to improve me. I appreciate all of these from him. He takes care of my business in VCU. I feel lucky and pride under his supervision. He is a so nice and considerate person

Here, I should give my special gratitude to the committee members: Vamsi K. Yadavalli, Dr. Arunkumar Subramanian and Dr. Stephen S. Fong for their valuable comments and suggestions.

Thanks to my group members Dylan Rodene, Matthew Decuir, Dr. Mehmet Gonen, Dr. Emmanuel Nyankson, Dr. Sushil Saraswat, deserve special appreciation for their assistance and cooperation in making our experience in the laboratory enjoyable but fruitful. They give me many touching moments in my life.

I would also like to thank the "El-Kaderi" and 'Collinson' research groups, especially Dr. Ahmed Farghaly, Tsemre Tessema, Fatema Choudhury and Babak Ashourirad for their friendship that made my journey here so enjoyable. Our collaborators Dr. Burak gave us a lot of inspiration and help during my research work. We have a wonderful cooperation. I am very grateful to them.

I am thankful for the Ministry of National Educational of the Republic of Turkey for my graduate fellowship.

My gratitude goes to my wife (Nur), my new baby (Erva), my parents and family who have always believed in me and supported me in all my endeavors.

This dissertation is dedicated to the memory of my grandmother, ZAHRA DEMIR (1945-2014)

I still miss her every day…

TABLE OF CONTENTS

List of Figures

List of Tables

List of Abbreviations

AC	Activated carbon
BET	Brunauer Emmett and Teller
CD	Charge discharge
CNT	Carbon Nanotube
CO_2	Carbon dioxide
CV	Cyclic voltammograms
DEP	Dielectrophoretic
E	Energy
EIS	Electrochemical impedance spectroscopy
E_{max}	Maximum energy
FTIR	Fourier Transform Infrared Spectroscopy
GC	Graphitic carbon
GC	Glassy carbon
H_2O_2	Hydrogen peroxide
H_2SO_4	Sulfuric acid
HHV	High Heating Value
HOR	Hydrogen oxidation reaction
HTC	Hydrothermal carbonization
K-L	Koutecky-Levich equation
KOH	Potassium hydroxide
MeGCx	Metal catalyst used and x graphitization temperature in ^oC

MWNT	Multiwall Nanotube
NGCx	Nitrogen doped carbon synthesized at x temperature
nm	Nanometer
ORR	Oxygen reduction reaction
P	Power
pm	Picometre
Pmax	Maximum power
Pt	Platinum
PTFE	Polytetrafluoroethylene
QSDFT	Quenched Solid State Functional Theory
RRDE	Rotating ring disk electrode
SC	Specific capacitance
SEM	Scanning electron microscope
SGCx	Sulfur doped carbon synthesized at x temperature
SWCNT	Single walled carbon nanotube
TGA	Thermogravimetric analysis
Ti	Titanium
UHV	Ultrahigh vacuum
wt. %	Weight percentage
XPS	X-ray photoelectron spectroscopy
XRD	X-Ray diffraction
Δt	Time of discharge

Abstract

RENEWABLE CARBON FROM LIGNIN BIOMASS AND ITS ELECTRODE AND CATALYST APPLICATIONS IN BATTERIES, SUPERCAPACITORS, AND FUEL CELLS

By MUSLUM DEMIR, Ph.D.

A Dissertation submitted in partial fulfillment of the requirements for the degree of Doctor of Philosophy at Virginia Commonwealth University.

Virginia Commonwealth University, 2017.

Director: Ram B. Gupta, Professor, Department of Chemical and Life Science Engineering

Over the last century, almost all of the carbon materials developed for the energy industry are derived from fossil fuels. The growing global concerns about energy needs, fossil fuels consumption, and the related environmental issues have motived scientists to find new, green and sustainable energy resources such as the wind, solar and biomass energy. Essentially, biomass-derived materials can be utilized in energy storage and conversion devices such as Li-ion batteries, fuel cells, and supercapacitors. Among the biomass resources, lignin is a high volume byproduct from the pulp and paper industry and is currently burned to generate electricity and steam. The pulp and paper industry has been searching for high value-added uses of lignin to improve its overall process economics.

The importance of manufacturing valuable materials from lignin is, discussed in Chapter 2, demonstrating the need for a facile, green and scalable approach to synthesize bio-char and porous carbon for use in Li-ion batteries. From this context, lignin is first carbonized in water at 300 °C and 103 bar to produce bio-char, which is then graphitized using a metal nitrate catalyst at 900-1100 °C in an inert gas at 1 bar. Graphitization effectiveness of three different catalysts, iron, cobalt and manganese nitrates was examined. The obtained materials were analyzed for morphology, thermal stability, surface properties, and electrical conductivity. Both annealing temperature and the catalyst affects the degree of graphitization. High-quality graphitization is obtained by using $Mn(NO_3)_2$ at 900 °C or $Co(NO_3)_2$ catalysts at 1100 °C.

Research on various energy storage materials for supercapacitors has grown rapidly in the recent years. Various advanced materials have been shown as a promising candidate for future's high-energy supercapacitor electrodes. For a material in a supercapacitor electrode to be considered, it must show promising results for its specific power and energy density, electrical conductivity, surface properties, durability, surface area and pore-size distribution in order to design and develop high-performance supercapacitor devices. The industrial applications of supercapacitors have not been satisfied due to the low energy density (the commercially available supercapacitors have between 5 to 10 times less energy density than that of batteries) and moderate charge-discharge rate of supercapacitor electrode. Thus, chapter 3 was aimed to design and synthesize nitrogen-doped carbon materials that show the characteristic of high-energy and high-power density supercapacitor electrodes with a long cycle life. With this aim, organosol lignin was successfully converted into N-doped carbon materials using a two-step conversion process. The nitrogen content in the carbon was up to 5.6 wt.%. The synthesize materials exhibit high surface area up to 2957 m^2/g with micro/meso porosity and a sheet-like structure. The N-doped carbon

produced at 850 ^{o}C exhibited a high capacitance value of 440 F g^{-1} at a 1 mV s^{-1} scan rate and demonstrated excellent cyclic stability over 30,000 cycles in 1 M KOH. In addition, the NC-850 delivers a high energy density of 15.3 W h kg^{-1} and power density of 55.1 W kg^{-1} at 1 mV s^{-1}. Therefore, this study suggests that N-doped carbon materials synthesized from a pulp and paper byproduct, lignin, are promising environmentally-sustainable candidates for supercapacitor applications.

Challenges for commercialization of fuel cells include high operation cost, inadequate operational stability, and poisoning by H_2O_2. To address the challenge, costly Pt-based catalysts are needed in order to facilitate the oxygen reduction reaction (ORR) at the cathode and the hydrogen oxidation reaction (HOR) at the anode. In chapter 4, alternative metal-free ORR catalyst materials derived from lignin are studied in order to simultaneously enhance the catalytic activity, lessen the Pt dependency and reduce the excessive costs associated. Calcium sulfonate lignin was successfully converted into sulfur self-doped carbons via in-situ hydrothermal carbonization and followed by post-annealing treatment. The sulfur content in the as-prepared porous carbons is up to 3.2 wt.%. The resulting materials displayed high surface areas (up to 660 m^2 g^{-1}) with micro/meso porosity and graphitic/amorphous carbon structure. The as-prepared sulfur self-doped electrode materials (SC-850) were tested as a potential cathodic material for ORR. The number of electrons transferred per molecule was measured to be ~ 3.4 at 0.8 V, which approaches the optimum 4 electron pathway. Additionally, S-doped materials were also applied as a supercapacitor electrode material. The SC-850 electrode exhibited a high specific and volumetric capacitance values of 225 F g^{-1} and 300 F cm^{-3} at a scan rate of 0.5 A g^{-1}. The SC-850 electrode also exhibited consistent response over 10,000 cycles at harsh conditions. It was shown that the metal-free SC-850 is a promising electrode material for supercapacitors and ORR applications.

All of the studies presented in this dissertation involve the development and application of carbon-based materials derived from lignin and its application towards the Li-ion batteries, supercapacitor, and fuel cell. Insight into the applicability of lignin-derived carbon materials towards electrochemical applications is made readily available, supplemented by detailed physical, chemical and electrochemical characterization, to examine the specific factors influencing the Li-ion batteries, supercapacitor, and electrocatalysis of fuel cell activity.

1.Chapter 1. General Introduction

1.1.Global energy demand

Until the 20th century, most of the industrialized materials such as fuels, solvents, and chemical products were produced from sustainable natural resources (i.e., plant or crop).[4] (Figure 1-1). Unfortunately, today most of the industrial materials such as fuels, carbons polymers, packing chemicals, pharmaceuticals, and construction are being manufactured from un-sustainable fossil fuels. Petroleum resources still are preferred due to the production cost and convenience of transportation. However, the world will face serious conflicts in the control and distribution of energy due to the limited supply of fossil fuels. An additional concern is that, as long as humans consume fossil-fuel derived products, CO_2 levels will continue to increase in the Earth's atmosphere. In the last decades, certain studies have attributed climate change and global warming to the continued release of CO_2 into the atmosphere. More scientifically, the CO_2 level has been increasing over the last 150 years from 228 ppm to 400 ppm as of 2016.[3] It is predicted that fossil fuel consumption will lead an ecological collapse of unprecedented scale due to the degradation of natural capital and loss of ecosystem by 2050. Thus, we have urgent duty to overcome these dark and worrying prospect of an ecological fiasco.

Green energy manufacturing and renewable energy are the most promising solution in order to cure the world's crude oil dependence. Especially, solar and wind energy will play a crucial role in the future. However, the availability of solar and wind energy depends strongly on the geography and local climate as its variation with the weather, time of day and season, which causes unpredictability in production. Thus, these types of energies required another storage system to match supply and demand imbalances. This incurs additional cost for efficient energy

storage and transportations. To help lower the cost and enhance sustainability, advance materials in batteries, supercapacitor, solar cells, gas storage, or efficient catalysts for fuel cell need to be developed. Utilizing of biomass-based feedstock instead of the petroleum hydrocarbons will provide notable opportunities for production of sustainable advance materials. [4]

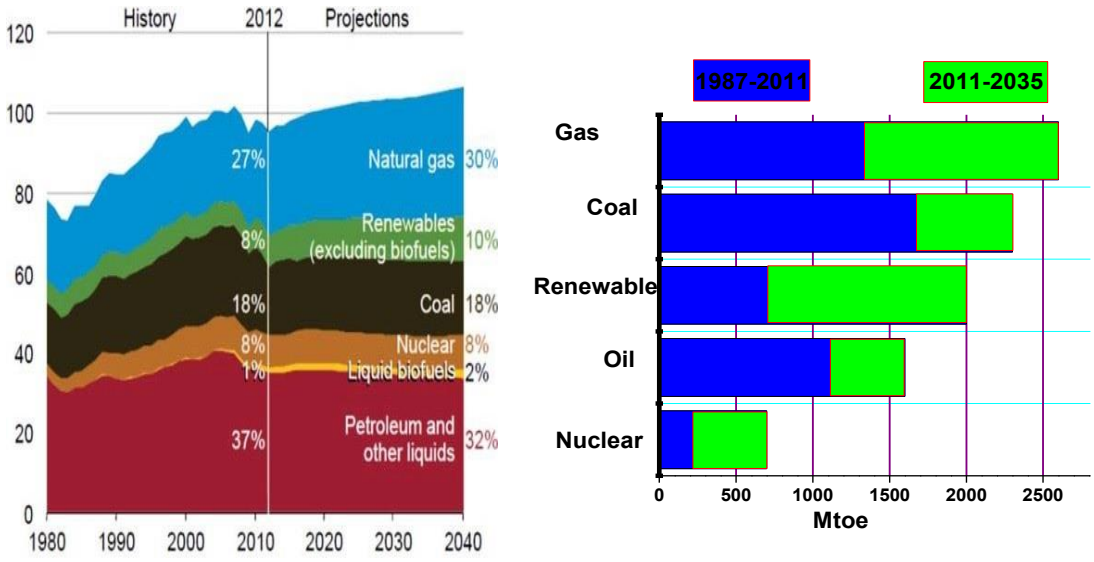

Figure 1-1. (a) U.S. energy consumption by fuels, 1980-2040 (quadrillion Btu) (Adopted from U.S. Energy information Administration, 2013) (b) World growth in total primary energy demand, 1987-2035.

1.2. Biomass

Biomass is a plant-derived material, such as forestry residues, agricultural wastes, and crops. In the context of various renewable resources, including a solar, wind energy, etc., biomass is the only renewable carbon resource in nature for utilizing value-added products.[10 8] Today's worldwide energy crisis and environmental concerns have prompted widespread research and development programs for biomass conversion.[6] In the context of the 2012 "International Year of Sustainable Energy for All" (SE4ALL), the International Renewable Energy Agency has produced a global roadmap called REMAP 2030 in order to increase the contribution of renewable energy around two times by 2030.[7] The Chinese National Energy Administration has stated a "National Twelfth Five-Year Plan" on biomass energy.[8] In this project, the consumption of biofuel (mainly ethanol and biodiesel) will reach 12 million metric tons by 2020. The U.S. Department of Energy also has launched an extensive target to produce at least 20% of transportation fuel from biomass 2030.[9]

Recently, approximately 10% of the world's energy is generated from biomass which is the fourth largest source of energy in the world after oil, coal, and natural gas. Essentially, most of the biomass is consumed to produce heat and power. Woody plants (lignocellulose), an annual harvesting of the most abundant source of biomass is produced at about 170 billion metric tons annually. Therefore, lignocellulose has been recognized as an alternative feedstock to replace fossil fuels.[13] Lignocellulose consists of three main molecular components: cellulose, hemicellulose, and lignin shown in Figure 1.2. Cellulose and hemicellulose have been industrially used in pulp and paper, biofuel and other important chemical technologies. On the other hand, the remaining part of biomass (lignin) is considered as a byproduct material.

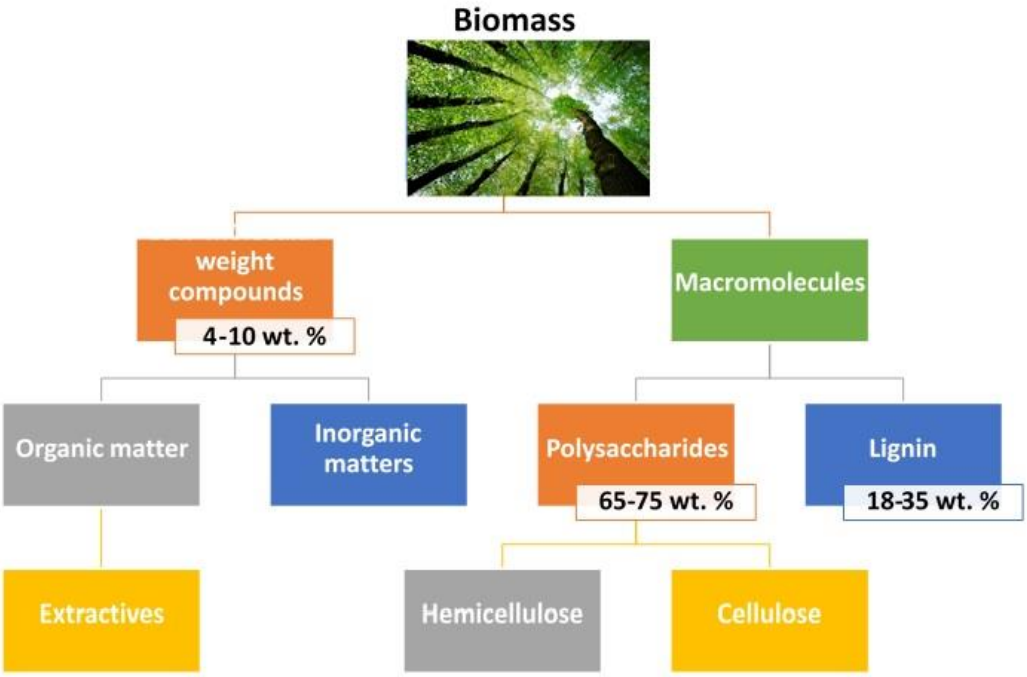

Figure 1-2 Composition of lignocellulosic biomass

1.3.Lignin

Lignin, a complex biopolymer of aromatic alcohols, is one of the most abundant natural polymeric material in nature.[12] Lignin is responsible for building up the cell walls which support the plant for standing. Lignin is a high volume byproduct generated in the pulp and paper industry. Most of the lignin is currently inefficiently burned to generate steam and electricity to sustain the needs of pulp and paper mills. Occasionally, additional power generated is sold out to the market. In recent years, intensive research efforts have been directed toward converting lignin into high value-added materials.[12,13,14]

1.3.1. Structure of Lignin

Lignin is a complex, amorphous, cyclic and random natural polymer. The structure, molecular weight, and composition of the lignin strongly depend on the source of biomass and the extraction process. The molecular weight of lignin ranges from 6000 to 12000 g/mol. Lignin is mainly composed of three primary units: coniferyl alcohol, sinapyl-based alcohols and with small amounts of coumaryl alcohol derivatives.[15] The monomeric units of lignin are linked to each other mostly by ether linkages and carbon-carbon bonds. The typical structure of lignin is shown in Figure 1-3.[15] In short, lignin possesses the following structural characteristics: (1) cross-linked structure of phenylpropane units, (2) amorphous and random structure, and (3) high molecular weight polymer.[15]

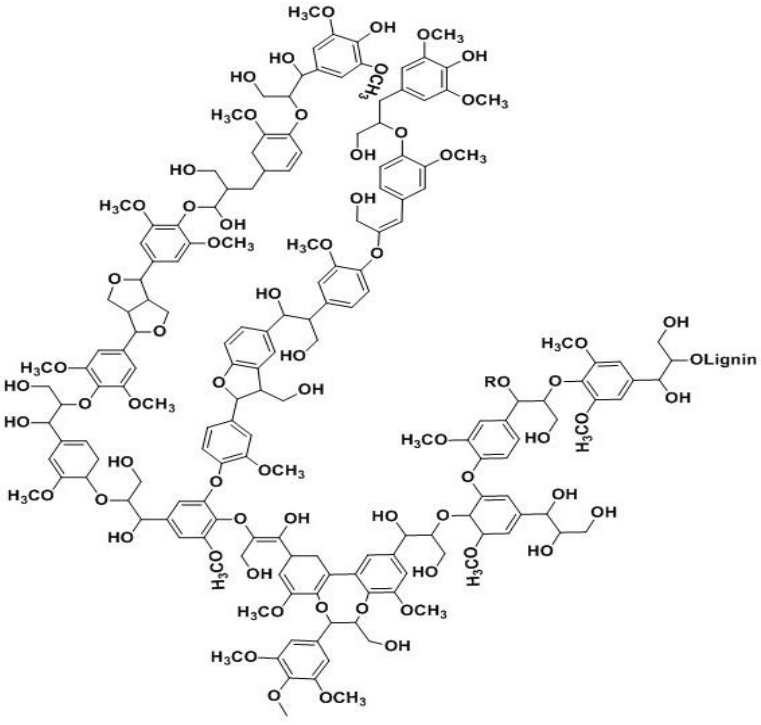

Figure 1-3. Molecular structure of lignin unit [5]

1.3.2. Sources of lignin

Lignin is the second most abundant polymer after cellulose in nature. Lignin, the main component of woody plants, and typically represents between 18-35 wt. percent of the dry mass. The production of lignin has been estimated about 45 million tons/year.[16]. The various industrial lignin is produced in large scale depending on the isolation process. For instance, Kraft lignin (KL), a well-known commercial lignin, is extracted from pulp mills in acidification process. Unlike lignosulfonate lignin, KL has poor solubility in water but can be hydrolyzed and converted to a soluble derivative. Recently, KL is majority commercial lignin which mainly manufactured in the USA and Canada. Most of KL is consumed as a fuel for pulp industry.[17] Lignosulphonate lignin are mainly generated from dissolving of woody plant in the water by adding hydrophilic sulfonate and hydrolytic ether groups as a soluble after hydrolytic removal of polysaccharides in the pulp and paper industry. India is the one of the main produces for sulfonated soda lignin.[18] Calcium lignosulfonate is new developing commercial lignin which extracted by hydrogen peroxide in alkali condition.[19] Calcium lignosulfonate is a good candidate for dispersant agent. In addition, lab-scale lignin isolation process from wood has been developed in last decade.[19] For instance, acid-catalyzed hydrolysis (HCl or HBr), organosols lignin (extracted by an organic solvent such as acetone, phenol), oxidation of wood by ligninolytic enzymes and, ionic liquid-extracted process. The obtained lignin generally have been produced as a pure, however, depends on pulping process, many minerals such as calcium and magnesium may be present on the final product.[20,21]

1.3.3. Application of lignin

Although lignin is generated in large quantities (>45 million tons) annually, most of the lignin is concentrated and burnt in pulp mills for steam generation. At present, only about 5 wt.% of the lignin produced in the pulp and paper industry is commercially used [22 23]. The second largest

utilizing of lignin is additives. Especially, calcium/magnesium lignosulfonates can be applied as water reducer additives which lessen the amount of water required for proper handling and mixing.[24,25] Moreover, over the past few decades, commercial utilization of modified lignin have been studied in various areas such as concrete admixtures, animal feed pellets, and roadside dust control, wetting, binding agents, etc.[26,27,27,28, 29,33,30,34] As the supply of the unused lignin is much more, there has been a renewed interest in the development of new value-added products from lignin [31].

1.4.Hydrothermal carbonization (HTC)

Hydrothermal carbonization (HTC) is a thermo-chemical processing for the conversion of biomass solid matters in water at a relatively elevated temperature and pressure. HTC is now a well-established technique used by many research groups for use in energy and environment applications. The mechanism for the HTC process is very similar to the natural formation of coal/carbon where a hundred million years is required to complete the process while the HTC only needs a few hours in the laboratory and offers a simple and green process to produce bio-char from biomass.[38,39] Biomass (or lignin) is non-conductive and amorphous and can be converted to carbon-rich bio-char[33] via pressurized water at elevated temperature and pressure. In this dissertation, the HTC method was used to synthesize bio-char from biomass similar to the method developed by Ramsurn and Gupta.[34] The sub-critical point of water was used for in this thesis. A high-pressure vessel equipped with sonication and temperature controller (Columbia instruments) is used. Usually, bio-char, CO_2, SO_2, methane gases are produced by the HTC process. The obtained compounds are separated from each other by different

techniques.[1] Schematic of a hydrothermal reactor equipped with sonicator and phase diagram of water at elevated temperatures are shown in Figure 1-4.

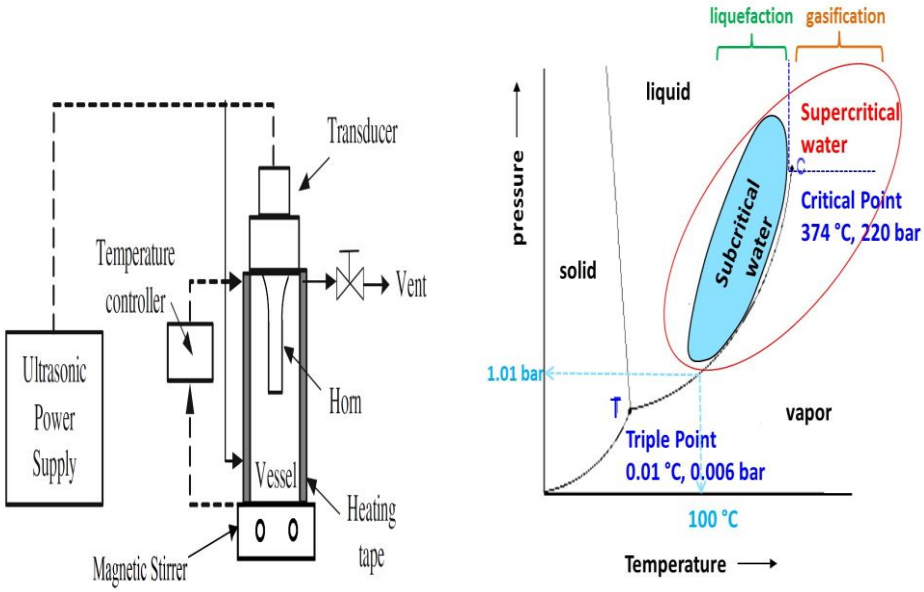

Figure 1-4 (a) Schematic of hydrothermal reactor equipped with sonicator and (b) phase diagram of water at elevated temperature.

1.5.Specific aims

Lignin is a high volume byproduct leftover from biomass in the pulp industry after removal of the cellulose and hemicelluloses to produce paper. Only about 5% of lignin is used in the industry to produce a valuable product, and rest is inefficiently burned to generate electricity and process heat. The pulp and paper industry is urgently seeking a value-added usage of their lignin to improve the process economics. On the other hand, supercapacitor, battery, and fuel cell manufacturers seek non-fossil fuel and low-cost sources of carbon for environmental. This

dissertation presents a pathway for the conversion of byproduct lignin into bio-char, graphitic carbon, N-doped or S-doped carbon. The morphology, surface and conductivity properties of lignin, bio-char, graphitic carbon and N-doped or S-doped carbon will be investigated. Also, electrochemical activity of the N-doped or S-doped materials will be examined for application as a supercapacitor electrode or ORR catalyst. Fundamental science questions that will be probed include: (a) the transformation of biomass hydrothermal carbonization, (b) the mechanism of catalytic graphitization, (c) how is surface and electrochemical properties controlled by the morphology via heteroatom doping into a carbon framework, (d) the dependence of the electrochemical performance of the surface and bulk properties of hetero-doped carbon materials, (e) the dependence of the electrochemical performance of the insertion of heteroatoms such nitrogen or sulfur for the ORR and supercapacitor application, and (f) how the conversion process impacts the electrochemical cycling of the material. Collectively, this proposal systematically will uncover simple and effective strategies to achieve with high conductivity and micro/mesoporous, electrochemically active of (N/S doped) graphitic carbon on the application of Li-ion batteries, supercapacitor, and fuel cell.

This research will be accomplished via the following aims:

(1) Morphology, surface, structural properties of lignin, bio-char graphitic carbon, and N-doped material will be studied,

(2) The degree of crystallinity and surface properties of graphitic carbon will be investigated by XRD and Raman spectroscopy. Also, the electrical properties of the graphitic carbon will be tested via a single-particle conductivity test. In addition, scalable and effective production of the graphitic porous carbon pathway will be studied in detail with variable metal catalyst and graphitization temperature,

(3) To improve specific capacitance of lignin-based carbon material through enhancing the affinity between the carbon and nitrogen molecules by intercalating of nitrogen atoms into the carbon structure and to explore and understand the roles of heteroatom doping in the electrochemical activity for supercapacitor electrode materials,

(4) Another important goal of this thesis is to synthesize sulfur-doped graphitic carbon in which sulfur molecules will introduce high-activity sites into the carbon framework. The S-doped carbon will be optimized regarding O_2 reduction activity toward fuel cell applications, then to investigate and recognize the roles of variable sulfur functional groups in carbon framework,

1.6. The layout of the dissertation

The chapters in the dissertation have been written in the style of American Chemical Society journal articles. As the chapters were written independently of each other, the reappearance of some basics and experimental results will lead to some duplication. Nevertheless, this does allow each chapter to be read independently, with each having its own introduction, experimental, results and conclusion sections. The outline of this dissertation is given below:

Chapter 1 provides context and motivation for this research work. The information related to global energy demand, global warming, and different eco-friendly energy source were briefly presented in this chapter. The main objectives of the study were also discussed in this chapter.

Chapter 2 gives a literature review of graphitic carbon, Li-ion batteries, and a transition metal as a catalyst support. Synthesizing pathway for graphitic carbon was shown in this chapter. The effect of three transition metal for formation of graphitization was compared. Mechanism of

graphitization by metal catalyst support was discussed. Furthermore, results from single particle conductivity measurement were presented.

Chapter 3 describes the application of the nitrogen-doped carbon for supercapacitor. It describes the synthetic procedure used and characterization of the nitrogen-doped carbon. In addition, doping of nitrogen was compared with pristine (i.e., un-doped carbon).

Chapter 4 describes the utilization of sulfur-doped carbon for the application on supercapacitor fuel cell application. Essentially, S-doped carbon was tested for the ORR catalysis and compared with commercial Pt/carbon catalyst.

Chapter 5 describes final conclusion and future directions of dissertation.

1.7. References

1. (a) Lichtenthaler, F. W.; Peters, S., Carbohydrates as green raw materials for the chemical industry. *Comptes Rendus Chimie* **2004,** *7* (2), 65-90; (b) Van Wyk, J. P., Biotechnology and the utilization of biowaste as a resource for bioproduct development. *TRENDS in Biotechnology* **2001,** *19* (5), 172-177.
2. Titirici, M.-M., 2 Green Carbon Nanomaterials. *Producing Fuels and Fine Chemicals from Biomass Using Nanomaterials* **2013**, 7.
3. Green, M. L.; Espinal, L.; Traversa, E.; Amis, E. J., Materials for sustainable development. *Mrs Bull* **2012,** *37* (04), 303-309.
4. (a) Huber, G. W.; Iborra, S.; Corma, A., Synthesis of transportation fuels from biomass: chemistry, catalysts, and engineering. *Chemical reviews* **2006,** *106* (9), 4044-4098; (b) Melero, J. A.; Iglesias, J.; Garcia, A., Biomass as renewable feedstock in standard refinery units. Feasibility, opportunities and challenges. *Energ Environ Sci* **2012,** *5* (6), 7393-7420.
5. Tuck, C. O.; Pérez, E.; Horváth, I. T.; Sheldon, R. A.; Poliakoff, M., Valorization of biomass: deriving more value from waste. *Science* **2012,** *337* (6095), 695-699.
6. Quadrelli, E. A., 25 years of energy and green chemistry: saving, storing, distributing and using energy responsibly. *Green Chem* **2016,** *18* (2), 328-330.
7. Liu, Z.; Guan, D.; Crawford-Brown, D.; Zhang, Q.; He, K.; Liu, J., Energy policy: A low-carbon road map for China. *Nature* **2013,** *500* (7461), 143-145.
8. Good, C.; Chen, J.; Dai, Y.; Hestnes, A. G., Hybrid Photovoltaic-thermal Systems in Buildings–A Review. *Energy Procedia* **2015,** *70*, 683-690.
9. (a) Carpenter, D.; Westover, T. L.; Czernik, S.; Jablonski, W., Biomass feedstocks for renewable fuel production: a review of the impacts of feedstock and pretreatment on the yield and product distribution of fast pyrolysis bio-oils and vapors. *Green Chem* **2014,** *16* (2), 384-406; (b) Dutta, S.; De, S.; Saha, B.; Alam, M. I., Advances in conversion of hemicellulosic biomass to furfural and upgrading to biofuels. *Catal Sci Technol* **2012,** *2* (10), 2025-2036.

10. (a) Ljubisa, R. R., Surface Chemical and Electrochemical Properties of Carbons. In *Carbons for Electrochemical Energy Storage and Conversion Systems*, CRC Press: 2009; pp 163-219; (b) Michio, I., Structure and Texture of Carbon Materials. In *Carbons for Electrochemical Energy Storage and Conversion Systems*, CRC Press: 2009; pp 37-76; (c) Jean-François, F.; Patrice, S., Principles of Electrochemistry and Electrochemical Methods. In *Carbons for Electrochemical Energy Storage and Conversion Systems*, CRC Press: 2009; pp 1-36; (d) Dolores, L.-C.; Fabián, S.-G.; Diego, C.-A.; ngel, L.-S., Porous Texture of Carbons. In *Carbons for Electrochemical Energy Storage and Conversion Systems*, CRC Press: 2009; pp 115-162; (e) Roland, G.; Hamid, G., Industrial Production of Double-Layer Capacitors. In *Carbons for Electrochemical Energy Storage and Conversion Systems*, CRC Press: 2009; pp 429-467; (f) Claude, L., Fuel Cell Systems. In *Carbons for Electrochemical Energy Storage and Conversion Systems*, CRC Press: 2009; pp 377-409; (g) Front Matter. In *Carbons for Electrochemical Energy Storage and Conversion Systems*, CRC Press: 2009; pp i-xii; (h) Toshiaki, E., Electronic Structures of Graphite and Related Materials. In *Carbons for Electrochemical Energy Storage and Conversion Systems*, CRC Press: 2009; pp 221-262; (i) François, B.; Encarnación, R.-P.; Elzbieta, F., Electrical Double-Layer Capacitors and Pseudocapacitors. In *Carbons for Electrochemical Energy Storage and Conversion Systems*, CRC Press: 2009; pp 329-375; (j) Petr, N.; Dietrich, G.; Michael, E. S., Carbon Materials in Lithium-Ion Batteries. In *Carbons for Electrochemical Energy Storage and Conversion Systems*, CRC Press: 2009; pp 263-328; (k) Ralph, J. B., Carbon in Batteries and Energy Conversion Devices. In *Carbons for Electrochemical Energy Storage and Conversion Systems*, CRC Press: 2009; pp 411-428; (l) Takashi, K.; John, C.; Yury, G., Carbide-Derived Carbons and Templated Carbons. In *Carbons for Electrochemical Energy Storage and Conversion Systems*, CRC Press: 2009; pp 77-113; (m) Morinobu, E.; YongJung, K.; KiChul, P., Advanced Battery Applications of Carbons. In *Carbons for Electrochemical Energy Storage and Conversion Systems*, CRC Press: 2009; pp 469-507.

11. Gosselink, R. J. A.; Abächerli, A.; Semke, H.; Malherbe, R.; Käuper, P.; Nadif, A.; van Dam, J. E. G., Analytical protocols for characterisation of sulphur-free lignin. *Industrial Crops and Products* **2004,** *19* (3), 271-281.

12. Cecilia, M., F. Toledo, and P. M. Kuznesof, Calcium lignosulfonate chemical and technical assessment. In *69th JECFA*, Rome, Italy, 2008; pp 40-65.

13. Gargulak, J. D.; Lebo, S. E.; McNally, T. J., Lignin. In *Kirk-Othmer Encyclopedia of Chemical Technology*, John Wiley & Sons, Inc.: 2000.

14. Duku, M. H.; Gu, S.; Hagan, E. B., A comprehensive review of biomass resources and biofuels potential in Ghana. *Renewable and Sustainable Energy Reviews* **2011,** *15* (1), 404-415.

15. Li, C.; Zhao, X.; Wang, A.; Huber, G. W.; Zhang, T., Catalytic Transformation of Lignin for the Production of Chemicals and Fuels. *Chemical Reviews* **2015**.

16. Agrawal, A.; Kaushik, N.; Biswas, S., Derivatives and Applications of Lignin–An Insight. *The SciTech Journal* **2014,** *1*, 30-36.

17. Fatehi, P.; Catalan, L.; Cave, G., Simulation analysis of producing xylitol from hemicelluloses of pre-hydrolysis liquor. *Chemical Engineering Research and Design* **2014,** *92* (8), 1563-1570.

18. Kong, F.; Wang, S.; Price, J. T.; Konduri, M. K.; Fatehi, P., Water soluble kraft lignin–acrylic acid copolymer: synthesis and characterization. *Green Chem* **2015,** *17* (8), 4355-4366.

19. Chakar, F. S.; Ragauskas, A. J., Review of current and future softwood kraft lignin process chemistry. *Industrial Crops and Products* **2004,** *20* (2), 131-141.

20. Carrott, P.; Carrott, M. R., Lignin–from natural adsorbent to activated carbon: a review. *Bioresource technology* **2007,** *98* (12), 2301-2312.

21. Smolarski, N., High-value opportunities for lignin: unlocking its potential. *Paris: Frost & Sullivan* **2012**.

22. Laurichesse, S.; Avérous, L., Chemical modification of lignins: Towards biobased polymers. *Progress in Polymer Science* **2014,** *39* (7), 1266-1290.

23. Zhou, S.; Brown, R. C.; Bai, X., The use of calcium hydroxide pretreatment to overcome agglomeration of technical lignin during fast pyrolysis. *Green Chem* **2015,** *17* (10), 4748-4759.
24. Hu, X.-Q.; Ye, D.-Z.; Tang, J.-B.; Zhang, L.-J.; Zhang, X., From waste to functional additives: thermal stabilization and toughening of PVA with lignin. *Rsc Adv* **2016,** *6* (17), 13797-13802.
25. Stewart, D., Lignin as a base material for materials applications: Chemistry, application and economics. *Industrial Crops and Products* **2008,** *27* (2), 202-207.
26. Mansouri, N.-E. E.; Salvadó, J., Structural characterization of technical lignins for the production of adhesives: Application to lignosulfonate, kraft, soda-anthraquinone, organosolv and ethanol process lignins. *Industrial Crops and Products* **2006,** *24* (1), 8-16.
27. Toledano, A.; Serrano, L.; Labidi, J.; Pineda, A.; Balu, A. M.; Luque, R., Heterogeneously Catalysed Mild Hydrogenolytic Depolymerisation of Lignin Under Microwave Irradiation with Hydrogen-Donating Solvents. *ChemCatChem* **2013,** *5* (4), 977-985.
28. http://www.ili-lignin.com/.
29. Kadam, K. L.; Chin, C. Y.; Brown, L. W., Continuous biomass fractionation process for producing ethanol and low-molecular-weight lignin. *Environmental Progress & Sustainable Energy* **2009,** *28* (1), 89-99.
30. Suhas; Carrott, P. J. M.; Ribeiro Carrott, M. M. L., Lignin – from natural adsorbent to activated carbon: A review. *Bioresource Technology* **2007,** *98* (12), 2301-2312.
31. (a) Fechete, I.; Wang, Y.; Védrine, J. C., The past, present and future of heterogeneous catalysis. *Catal Today* **2012,** *189* (1), 2-27; (b) Yu, G.; Sun, B.; Pei, Y.; Xie, S.; Yan, S.; Qiao, M.; Fan, K.; Zhang, X.; Zong, B., Fe x O y@ C spheres as an excellent catalyst for Fischer− Tropsch synthesis. *Journal of the American Chemical Society* **2009,** *132* (3), 935-937; (c) Qian, H. S.; Antonietti, M.; Yu, S. H., Hybrid "Golden Fleece": Synthesis and Catalytic Performance of Uniform Carbon Nanofibers and Silica Nanotubes Embedded with a High Population of Noble-Metal Nanoparticles. *Adv Funct Mater* **2007,** *17* (4), 637-643.
32. (a) Xiang, X.; Bai, L.; Li, F., Formation and catalytic performance of supported ni nanoparticles via self-reduction of hybrid NiAl-LDH/C composites. *AIChE journal* **2010,** *56* (11), 2934-2945; (b) Ming, J.; Liu, R.; Liang, G.; Cheng, H.; Yu, Y.; Zhao, F., Knitting an oxygenated network-coat on carbon nanotubes from biomass and their applications in catalysis. *J Mater Chem* **2011,** *21* (29), 10929-10934.
33. Ramsurn, H.; Kumar, S.; Gupta, R. B., Enhancement of biochar gasification in alkali hydrothermal medium by passivation of inorganic components using Ca (OH) 2. *Energy & Fuels* **2011,** *25* (5), 2389-2398.
34. Titirici, M.-M. Hydrothermal Carbonisation: A Sustainable Alternative to Versatile Carbon Materials. Universität Potsdam Potsdam, 2012.

2.Chapter 2. Graphitic bio-carbon from metal-catalyzed hydrothermal carbonization of lignin

2.1. Energy storage devices and Li-ion batteries

In the last century, energy storage has become very popular science area due to its importance for humanity to balance supply and demand of energy.[2] Energy can be stored in different ways such as fuels for combustion, water for hydroelectricity, or electrochemically in batteries, supercapacitors, and fuel cells.[3] Li-ion batteries are most popular power storage media since they were launched in 1981 due to due to widespread use in portable electronic devices, electric cars, and hybrid cars.[3b,3a,4]

Energy storage/conversion technology devices are evaluated based on the energy and the power density so-called Ragone plot and competition of batteries with a supercapacitor, shown in Figure 2-1 and Table2-1.[15] Ragone chart provides information for comparing of various energy storage/conversion devices. The X-axis presents the energy density while Y-axis shows the power density. Notably, the capacitors have very high power density and very low energy density. Supercapacitors have the potential for optimum level power and energy densities for energy storage device due to storing electron for short time. On the other hand, Li-ion batteries have high specific energy density but low specific power density which chemical reaction supply electron. Fuel cells (an energy conversion device) have even higher specific energy density with very low specific power due to the efficiency of the electrochemical reaction.[6] For practical application, it is desired that the energy device has high specific along with high power density.

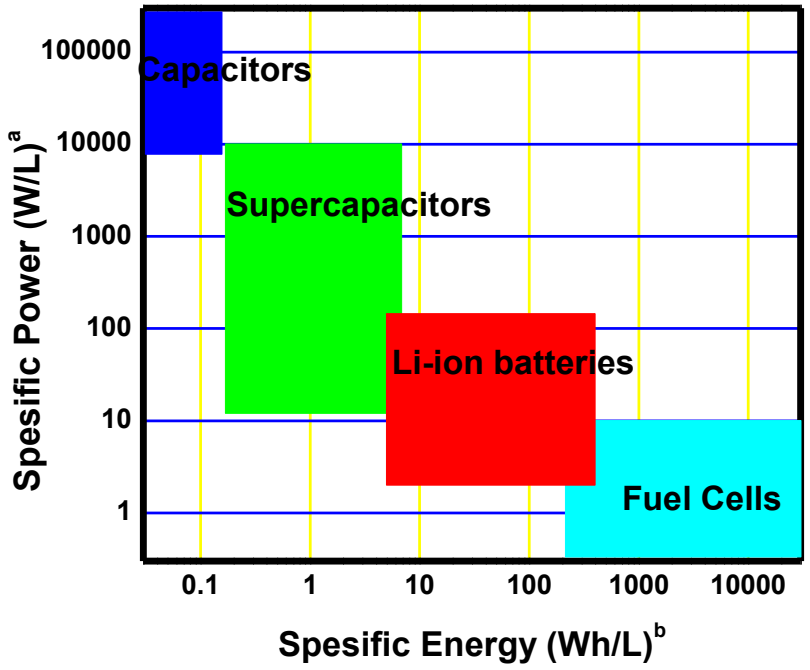

Figure 2-1. Ragone plot of energy storage/conversion technology (a per volume of power, b per volume of energy)1

Li-ion cell consists of two electrodes (anode and cathode) and one separator soaked in conductive electrolyte. Metal oxide ($LiCo_2$) has been widely used as a cathode electrode while an anode material graphite. In a typical discharge process, Li ions are a shuttle from the negative electrode through the electrolyte to the positive electrode, meanwhile, electrons flow in the external circuit which creates an electrical current. In the charging process, opposite flow takes place. In this circulation, the electrochemical redox reaction occurs in positive and negative electrodes.[7,8] Commercially, carbon (graphite) and metal oxide materials have been utilized as a negative and positive electrodes, respectively. Due to the limited theoretical capacity (372 mA h g^{-1}), poor rate and economic viability of pure graphite, novel, porous and inexpensive electrode materials need to be studied for higher performances.[9,10,11]

In Li-ion battery arena, much non-carbonaceous have been explored as anode materials such as Si[12] Sn[13] and transition metal oxides[14] due to their high specific capacity. However, these materials have certain drawbacks. For instance, during the charge/discharge process, significant volumetric expansion cause a large irreversible capacity and poor cycling stability[14,15] Therefore, It is challenging to commercialize non-carbonaceous material in Li-ion batteries. These disadvantages divert researchers again to focus carbon-based materials for high-capacity.

Table 2-1 Comparative Data of Batteries and Supercapacitors

	Batteries	**Supercapacitors**
	Not capacitive properties. Electrochemical reaction of anode and cathode in electrolyte	Capacitive properties: Only
		Reversible
	The potential difference is ideally constant throughout the charge/discharge cycle which leads a thermodynamic potential	The potential difference thermodynamically depends on charge accumulation on the
		Low: from 1 to
Power Density	Low:	Extremely High:
Cyclability	Poor due to the redox and phase-change processes	Life time cyclibility
	Poor, because of degradation	Long
Electrolyte	Variable depends on cell reaction	May consume due the ion adsorption on the surface

Typically, carbon consists of four main allotropes (amorphous carbon, graphite, diamond, and C_{60}) shown in Figure 2-2. Graphite has low surface area and is highly conductive (both, thermally and electrically) due to its unique electronic structure where carbon atoms covalently bonds to the three neighbor atom. One spare electron is delocalized in the whole sheets which are responsible for high conductivity. On the other hand, amorphous carbon contains high surface, but poor conductivity due to the disordered bonding of carbon atoms. Graphitic carbon is a combination of amorphous carbon with graphite sheets disordered carbon particles.[16] Due to the synergistic effect of the two, graphitic carbon has received more attention.[17,18,

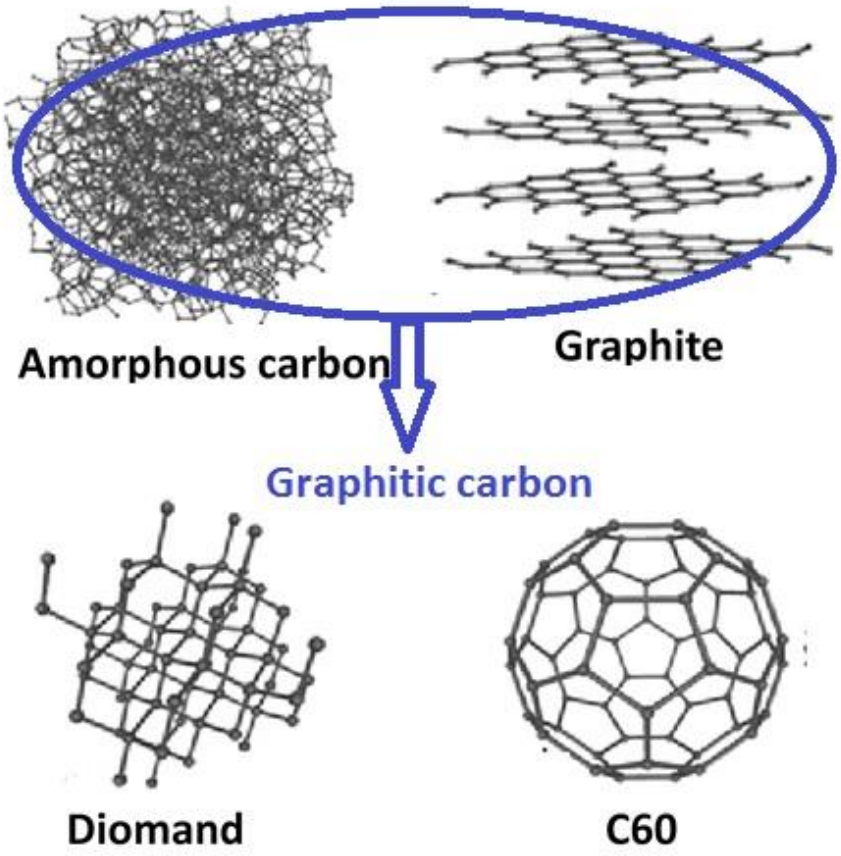

Figure 2-2. Basic allotropes of carbon (adapted from Wikipedia and modified)

2.2. Graphitic carbon

In the last decade, graphitic carbon materials have received much attention due to their attractive physical and chemical properties such as high surface area, chemical resistivity, high thermal and electrical conductivity.[19] There are much potential application of graphitic carbon. For instance, as gas storage material, catalytic support, specific adsorbents and electrode materials for Li-ion batteries and supercapacitor.[20,20,21] Optimum performance of carbon materials for application in these fields rely on their physical properties, surface activities, morphology, and

precursors used, which allows for the material to be modified for specific application [22,23,24]. A number of methods have been developed to prepare carbon materials of controlled physical characteristics, such as the degree of crystallinity, morphology, particle size, or porosity.[25,26] Specifically, the degree of crystallinity of the carbon framework plays a critical role in many electronic applications. The ratio of graphite sheet and amorphous structure determine the degree of crystallinity in carbon framework. Graphitic carbon has many advantages over amorphous and graphite structure because of the well-developed crystalline structure, high electronic conductivity and thermal stability [27,28,29]. Thus, manufacturing of graphitic carbon with a large and accessible surface area is of great interest in the many applications.

2.3. Production of graphitic carbon from biomass

Pure graphite is conventionally produced by high heat treatment (~3000 °C) or stress graphitization of carbon-rich feedstocks.[30] Due to the severity of process conditions, this method is expensive, complex, and limited in scalability. In addition, the as-prepared graphite has a low surface area and poor porosity due to non-existent pore activation agent during the graphitization process. The BET surface area of graphite is only 43 $m^2 g^{-1}$.[30] In order to reduce the severity of process conditions, transition metals have been applied as a catalyst for conversion of amorphous carbon into graphite sheet at relatively low temperatures. The temperature in graphitization can be significantly reduced (down to ~1000 °C) by use of transition metals such as Fe, Ti, Co, Ni, and Mn.[31,32,33,34,35] In addition, metal impregnation during the graphitization treatment can enhance surface properties.[27,28,36,36,37] Many carbon-based materials have been investigated as anode materials such as carbon nanotubes (CNTs),[38] hollow nanospheres,[39] graphene[40] etc. However, the severity of the process, the usage of petroleum-derived feedstock and expensive

equipment and make them less attractive in scale-up applications. In recent years, several research groups have utilized biomass feedstock to produce graphitic porous carbons that have a certain graphitic order for lithium-ion batteries such as wheat straw,[41] agricultural waste,[42] banana peels,[43] ox horn,[44] peanut shells,[45] coconut shell,[46] honey,[47] fish scales, [4848] human hair[4949] and plant biomass[50]. Biomass-derived carbons are attractive alternatives due to the renewability, low-cost and low toxicity. In addition, biomass-derived carbons provide excellent porous and conductive structure which are key factors for high lithiation capacity and cyclability in Li-ion batteries.[51] However, there has been only limited work on the utilization of lignin as a feedstock using metal-based catalysts [52]. Lignin, due to its aromatic molecular structure, presents an exciting feedstock for graphitic carbon production.[53,54,55]

2.4. Experimental

2.4.1. Conversion of lignin to bio-char

Bio-char was prepared from lignin by hydrothermal treatment [55]. Lignin (14 grams) was mixed with de-ionized water (100 mL) and placed in a high-temperature, high-pressure Parr reactor. The conversion was carried out at 300 ^{o}C and 103 bar for 30 minutes. The reactor was then allowed to cool to room temperature; here bio-char, due to its hydrophobic nature, separates easily from the aqueous media. It is important to note that we have not used any catalyst during the bio-char synthesis step. The overall conversion scheme is shown in Figure 2-3.

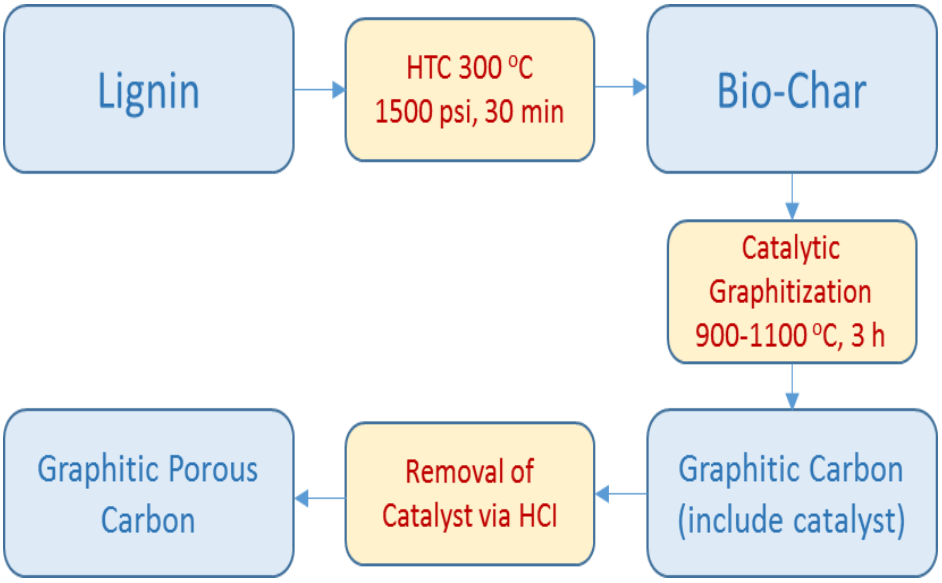

Figure 2-3: Synthesis scheme of lignin into graphitic carbon

2.4.2. Catalytic graphitization of bio-char

Metal salt catalysts were added to the bio-char by a solution impregnation method. Fe(II), Co(II) or Mn(II) nitrate solutions in ethanol, which were prepared in concentrations of 0.02 mole of Fe(II)NO_3 and 0.083 Mn(II)NO_3 and Co(II)NO_3 mole-metal/g, were added to bio-char. The resultant solutions were stirred at room temperature for 6 hours, and then ethanol was removed under vacuum. The obtained mixtures were heated under argon at a heating rate of 20 °C/min and kept at the graphitization temperature 900-1100 °C for 3 hours in a Carbolite (MTF-250) tubular furnace. Schematic illustration of the tubular furnace was shown in Figure 2-4. The product was then cooled and washed with 3 M HCl to remove the catalyst. The final carbon samples were labeled as MeGCx, where Me denotes the metal catalyst used and x graphitization temperature in °C). For comparison, a graphitic carbonization (GC1000) sample was processed in a similar manner but without the use of a catalyst.

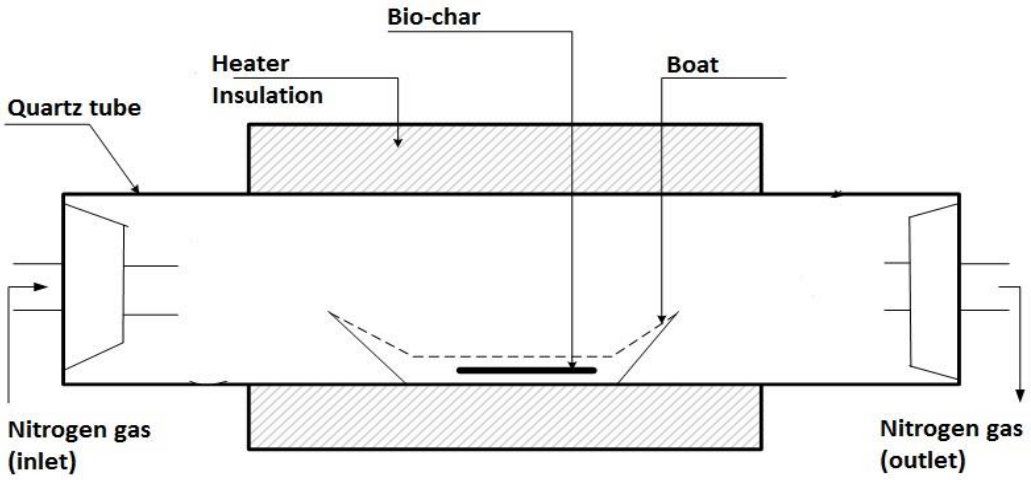

Figure 2-4: Schematic illustration of tubular furnace for annealing treantment of bio-char

2.4.3. Physical and chemical characterization

The degree of graphitization was determined by collecting X-ray diffraction (XRD) patterns on a Siemens D5000 instrument operating at 40 kV and 40 mA, using CuKa radiation (k = 0.15406 nm) by scanning 2Θ ranging 10-70°. X-ray diffraction was used as a base analysis for the degree of graphitization for experiments at all the temperature and catalyst studied; selected promising materials were investigated by further analysis. Raman spectra were obtained with a micro-Raman spectrophotometer (Horiba, Labram HR) applying an excitation wavelength of 32 nm as the light source. X-ray photoelectron spectroscopy (XPS) analysis was performed under an ultrahigh vacuum (UHV) on a ThermoFisher ESCALAB 250 imaging X-ray photoelectron spectrometer by applying a monochromatic Al Kα (1486.68 eV) X-ray source. An internal flood gun (2 eV) and a low-energy Ar^+ external flood gun were applied for charge compensation during

the data collection. Thermal stability analysis of lignin, bio-char and graphitic carbon materials was carried out on a Perkin thermo-gravimetric analyzer. The analyzer operated at a constant heating rate of 20 °C/min with N_2 flow (ranging from 50 to 1000 °C). FT-IR spectra were collected to observe the conversion of the reactants. A small amount of sample was placed directly on a Smart ATR using a Nicolet Nexus 670 FT-IR spectrometer and scanned from 4000 to 400 cm^{-1}, averaging 16 scans at 1 cm^{-1} intervals with a resolution of 4 cm^{-1}. Scanning electron microscope SEM (Hitachi SU-70 FE-SEM) was operated at 10 kV in order to investigate the graphitic porous carbon structure. The BET surface area and pore size distribution of graphitic carbon materials were deduced from the isotherm analysis in a relative pressure range of 0.04–0.20 by a NOVA surface analyzer. Pore size distributions (PSD) were calculated using Non-Local Density Functional Theory (NLDFT) on the adsorption branch. The high heating value (HHV) of materials were analyzed using an IKA C 200 calorimeter. Briefly, the solid powdered sample was put in a sample holder which is a transparent capsule include a known calorific value. The sample in the capsule was located in a stainless steel crucible in a bomb calorimeter and pressurized with oxygen at 34 bars. The HHV of the sample was automatically measured by the change of temperature of water by the heat generated from total combustion of the sample. The HHV value of sample obtained by subtracting the total HHV value from the HHV value of the capsule.

Electrical transport properties of GC1000 and MnGC1000 particles were characterized using two-terminal current-voltage (I-V) curves. The sample preparation process involved the dielectrophoretic (DEP) assembly of individual particles across spatially separated gold nanoelectrode pairs (Fig. 3), which was defined on top of thin-film nitride (100 nm) coated silicon chips using a combination of electron beam lithography and metal lift-off steps. The DEP process employed the use of non-uniform, AC electric fields to localize single graphitic particles and yield

their assembly at the electric-field maxima, which is located in the inter-electrode gap region near the electrode surface. The control parameters for yielding single particle localization have been published in detail elsewhere, as a part of previous studies involving one-dimensional constructs derived from manganese oxide and carbon material systems [56,57,58]. Briefly, an AC bias is applied across the nanoelectrode pair and a droplet, which contains a colloidal suspension of the graphitic particles in ethanol, is placed on the chip. As a result of the applied electric field, the particles become polarized and the induced dipole experiences a dielectrophoretic force. This DEP force attracts the particles towards the electric field maxima and yields their assembly on top of the gold nanoelectrodes. After assembly, the chip is dried using a nitrogen gun. The GC1000 particles were assembled by applying a 4 V bias at 1 kHz for 2 minutes. On the other hand, MnGC1000 particles were assembled using a 3 V bias at 1 kHz for 2 minutes. Representative images of the chip design and an assembled GC1000 particle are shown in Figure 2-5 (a-b).

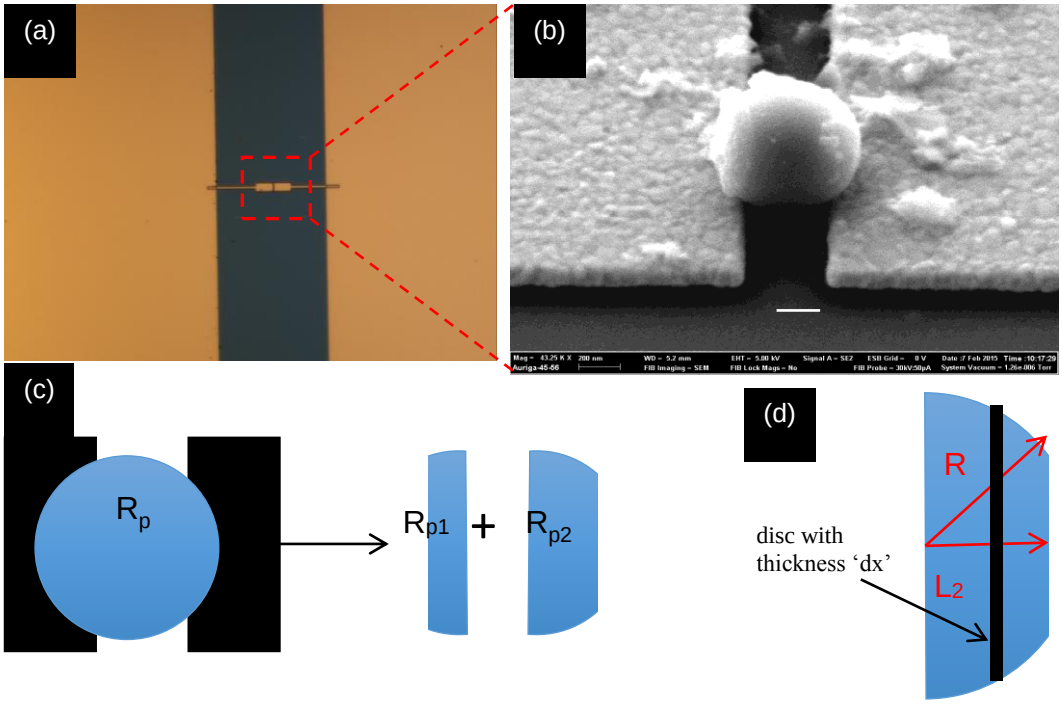

Figure 2-5 (a) An optical micrograph of the chip electrode design. (b) A zoomed-in region of the DEP assembly electrode region showing a single GC1000 particle bridging the electrodes. The scale bar represents 200nm. (c) A schematic illustration of the assembled particle and its resistance as a sum of the respective suspended, inter-electrode segments within the left and right hemispherical components of the particle. (d) An illustration of the geometric parameter definition used within the analytical model to extract particle conductivity values.

2.5. Result and discussion:

2.5.1. Performance of the graphitic carbon

In this work, we present a new approach based on the lignin graphitization to produce porous carbons with a graphitic framework. Our two-step conversion strategy is based on a combination of hydrothermal treatment (HTC) and catalytic graphitization steps. In the hydrothermal treatment step, lignin precursor is converted to bio-char. In the catalytic graphitization step, metal nitrates are used as catalysts at low temperatures (~1000 ºC). Here, the process of graphitization is thermodynamically favorable because bio-char is thermodynamically less stable than graphitic carbon. When thermally unstable bio-char is converted to a graphitic material, the electrical conductivity of the material improves.[59,59] The synthesized graphitic porous carbon exhibits a range of structural characteristics depending on this ability to separate each step during synthesis [36]. The calorimetric (High Heating Value, HHV) analysis results of lignin, bio-char and graphitic carbon materials are listed in Tables 1. The HHV content increased during the hydrothermal treatment and catalytic graphitization step. Similar trends occur with graphitization (non-catalyst) at 1000 °C with a value of 26 kJ/g. MnGC1000 shows the highest HHV values of 29 kJ/g, which is due to the removal of more oxygen during the catalytic graphitization steps.

Table 2-2: High heating values of lignin and obtained materials

Carbon sample	*HHV (kJ/g)*
Lignin	18
GC1000	26
MnGC900	26
MnGC1000	29

The XRD patterns in the wide-angle region (10°–70°) permit an evaluation of the graphitic nature of the synthesized carbons. The XRD patterns of the graphitic carbons are shown in Figure 2-6. As a reference, the XRD pattern of bio-char (a) and non-catalysis GC1000 sample (c) are also shown. As expected, bio-char (a) reveals almost no diffraction peak observed and GC1000 (c) exhibited only small characteristics of graphited carbon diffraction peak. These results are consistent with an amorphous framework. In contrast, the metal catalyzed carbons show intense XRD peaks at around $2\theta = 26°$ and 44°. These peaks can be assigned to the (002) and (101) diffractions of a graphitic framework.[60] These results indicate that the formation of graphitic structures is promoted by heat treatment in the presence of metal nitrate catalysts. Similar results have been reported previously for graphitic carbons generated from metal-impregnated polymeric gels, aerogels and bio-source materials.[28 27 36-37] As shown in Figure 2-6 (a), MnGCs exhibited the largest graphitic carbon peaks among the three types of metal nitrate catalysts. In the case of MnGCs, MnGC900 (f) showed a sharper peak than MnGC1000 (e) and MnGC1100 (d). It is found that the degree of bio-char graphitization by manganese (II) nitrate impregnation is greater at the lower temperature due to more amorphous carbon remain in the MnGC1000 structure. This is attributed to the high number of oxygenated functional groups in the carbons at low carbonization

temperatures [36]. This presumably favors the reduction of metallic salts and formation of metal particles at relatively low temperatures.

For the case of cobalt nitrate catalysis, the graphitization process started at 900 ^{o}C (h) and almost stopped at 1000 °C (i) shown in Figure 2-6 (b). As a result, increasing the temperature did not increase the graphitization. Graphitic carbon formation via iron nitrate catalysis requires a higher temperature of around 1100 °C (k) and shows a higher XRD peak than graphitic carbon at 1000 °C (l) presented in Figure 2-6 (c). The samples before acid wash still contain the metal originating from the catalyst; Mn, and MnO (b) particles located at around 39°, 45°, and 54°; and Co, CoO (g) particles placed at 49° and 58°, in XRD. [61]

The graphitic carbon structures are formed by a series of steps in the catalytic process. When the bio-char with a metal salt is heated, the salt decomposes to form the corresponding metallic oxides such as MnO and CoO. With continued heating, the carbon-oxygen-metal structure reduces to a metal-carbon structure. When the temperature reaches 900 °C or higher, the transformation of carbon from amorphous into a more ordered graphitic structure occurs, both catalyzed by metal and metal oxide particles.[36] Moreover, according to reference[62], Group IVb to VIIb metals on the periodic table known as graphitization metal catalysts since they have 2 to 5 electrons in the d-shell orbital which make them capable of forming strong bonds between metal carbides and carbon-based materials. On the other hand, group VIII metals have 6 to 10 electron in their d-shell orbital which makes them less active in terms of accepting electrons from carbon-based materials. This is consistent with our results that manganese (in VIIb group) show higher the degree of graphitization than cobalt and iron based catalysts (in VIII group).

The nature of graphitization of carbon materials was further evaluated by Raman spectroscopy. The application of Raman as an evaluation degree of graphite was first reported by

Tuinstra [63]. The D band located at around 1350 cm^{-1} corresponds to the disordered graphitic lattice (A_{1g} symmetry).The D band which is in Raman inactive mode is related to loss of hexagonal symmetry in the graphite structure. The G band placed at around 1578 cm^{-1} is associated with the vibration of the ideal graphite lattice (E_{2g} symmetry) [63] shown in Figure 2-6 (D). The G band which is in Raman active mode is referred to 2-dimensional high crystalline network structure. The intensity ratio of G band to D band (I_g/I_d) is a good indicator of the degree of graphitization for carbon-based materials. The I_g/I_d values were 1.1 and 1 for MnGC1000 and CoGC1000, respectively, which are higher or comparable than those reported data previously. [29], [27], [20], [59], [60], [64], [65]

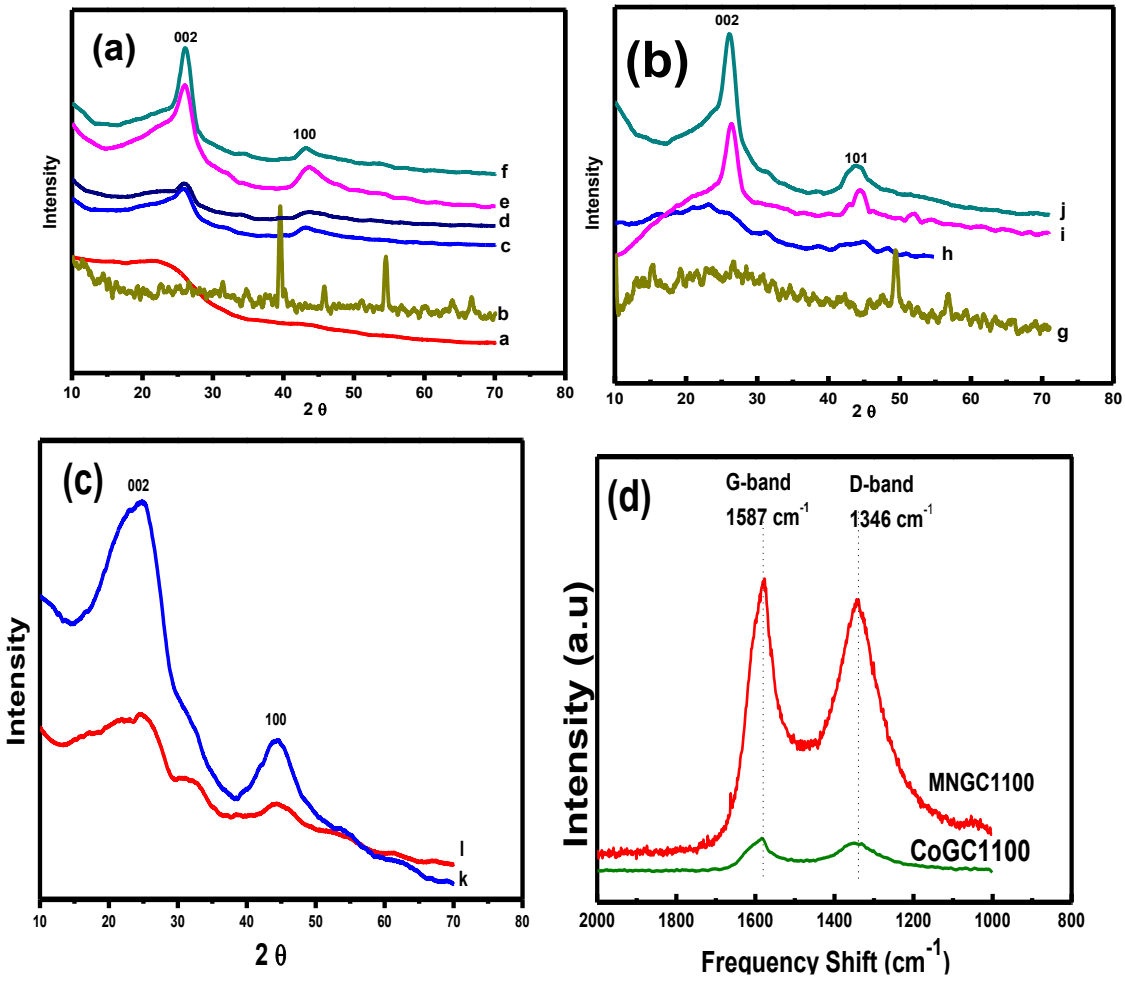

Figure 2-6: (a),(b), and (c) are the XRD patterns of the carbon samples: (a) bio-char, (b) MnGC1000 (before metal removal), (c) GC1000, (d) MnGC1100, (e) MnGC1000, (f) MnGC900, (g) CoGC1000 (before metal removal), (h) CoGC900, (i) CoGC1000, (j) CoGC1100, (k) FeGC1100, and (l) FeGC1000. (D) Raman spectrum of the MnGC9000 and CoGC1100.

The elemental analysis and the functional groups of carbon materials were detected by XPS spectroscopy shown in Figure 2-7 and Table 2.3. The carbon content of materials were 64.1, 64.9 and 50.4 for GC1100, CoGC1100 and MnGC900, respectively. The carbon types of materials classified such as graphitized carbon that is the C=C groups (E_B = 284.4 eV) and other natures of

carbon (amorphous carbons) which are i.e. C–C/CHx groups (E_B = 285.1 eV) , -C-O (E_B = 286.2 eV) and >C=O (E_B = 287.2 eV). [19], [66] Although the GC1100 has higher carbon content on the surface than the metal catalyzed graphitic carbons, the MnGC900 and CoGC1100 show a higher ratio of the graphitized carbon to amorphous carbon than the GC1100. The ratio of the graphitized carbon to amorphous carbon was found to be 0.45, 0.53 and 0.60 for GC1100, CoGC1100 and MnGC900, respectively, which demonstrate that the formation of graphitic carbon enhanced by including metal nitrate catalyst in the graphitization step.

Table 2-3: Elemental and functional group analysis of the CoGC1100, MnGC900 and GC1100

Materials	**C (wt. %)[a]**	**O (wt. %)[a]**	**Metal catalyst (wt. %)[a]**	**C=C (at. %)**	**C-C (at. %)**	**-C-O (at. %)**
GC1100	64	27.7	-	45.3	16.8	20.8
CoGC1100	64.9	32.3	2.1	53.7	20.8	13.7
MnGC900	50.4	39.8	9.6	60.7	21.9	9.4

a: Run by XPS

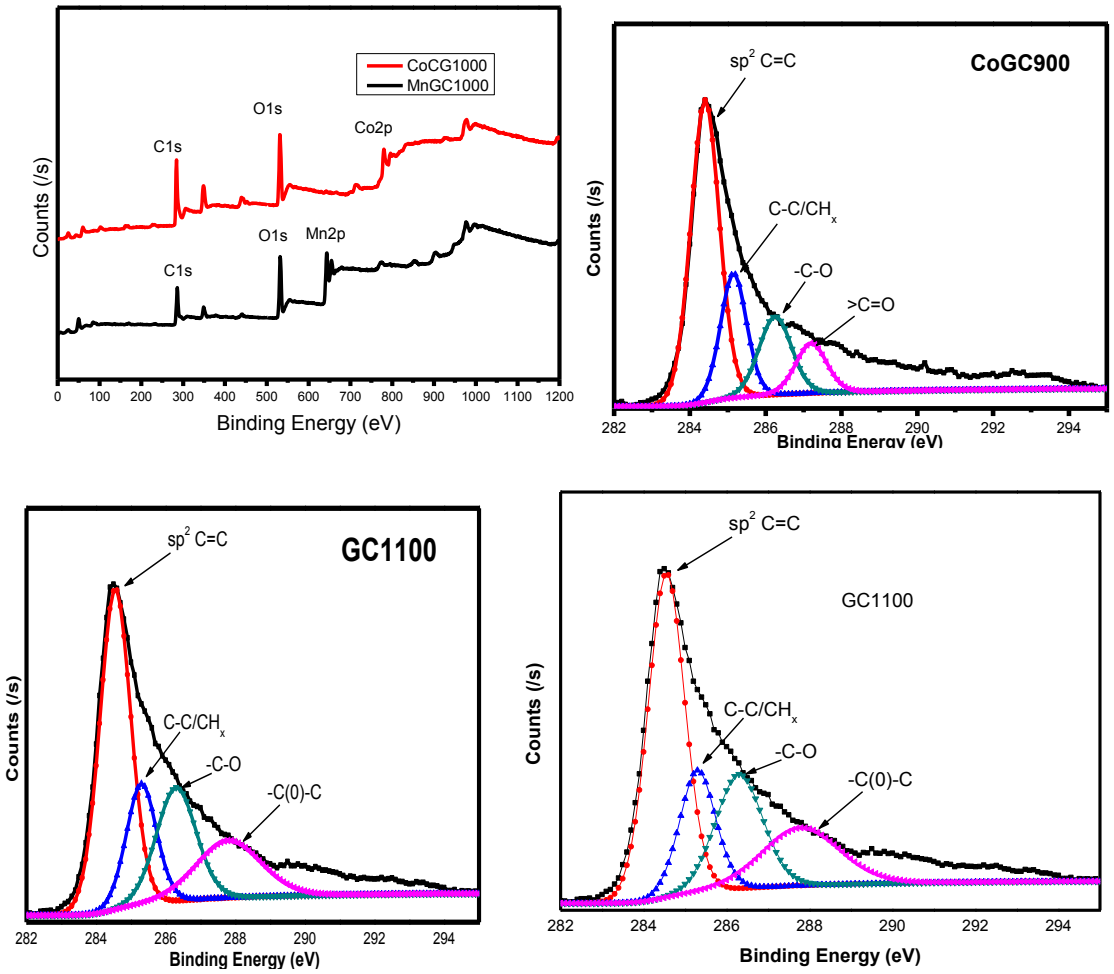

Figure 2-7: XPS spectra of the CoGC1100, MnGC900 and GC1100

2.5.2. Morphology and pore structure

The scanning electron microscope (SEM) micrographs of bio-char, GC1000, MnGC900 (with metal), MnGC900 (without metal) are shown in Figure 2-8 (A, B, C and D). Bio-char particles are spherical in shape and are 4 µm in diameter. GC1000 are globular precipitated solids with 1-3 µm diameters, and MnGC900 solids are also globular with 2 µm diameters. Figure 2-8

(B, C) shows SEM images of MnGC900 before acid washing, where a metal-carbon mixed structure is prominent. From the SEM micrographs of materials, the distribution of particle sizes within an order of magnitude is consistent with results observed for hydrothermal synthesis of particles. Also, we do not expect any size dependence on the properties of these materials because this is expected to occur only when their size extends within the nanometer-regime. At these size scales, we believe that the properties are largely determined by the degree of graphitization.

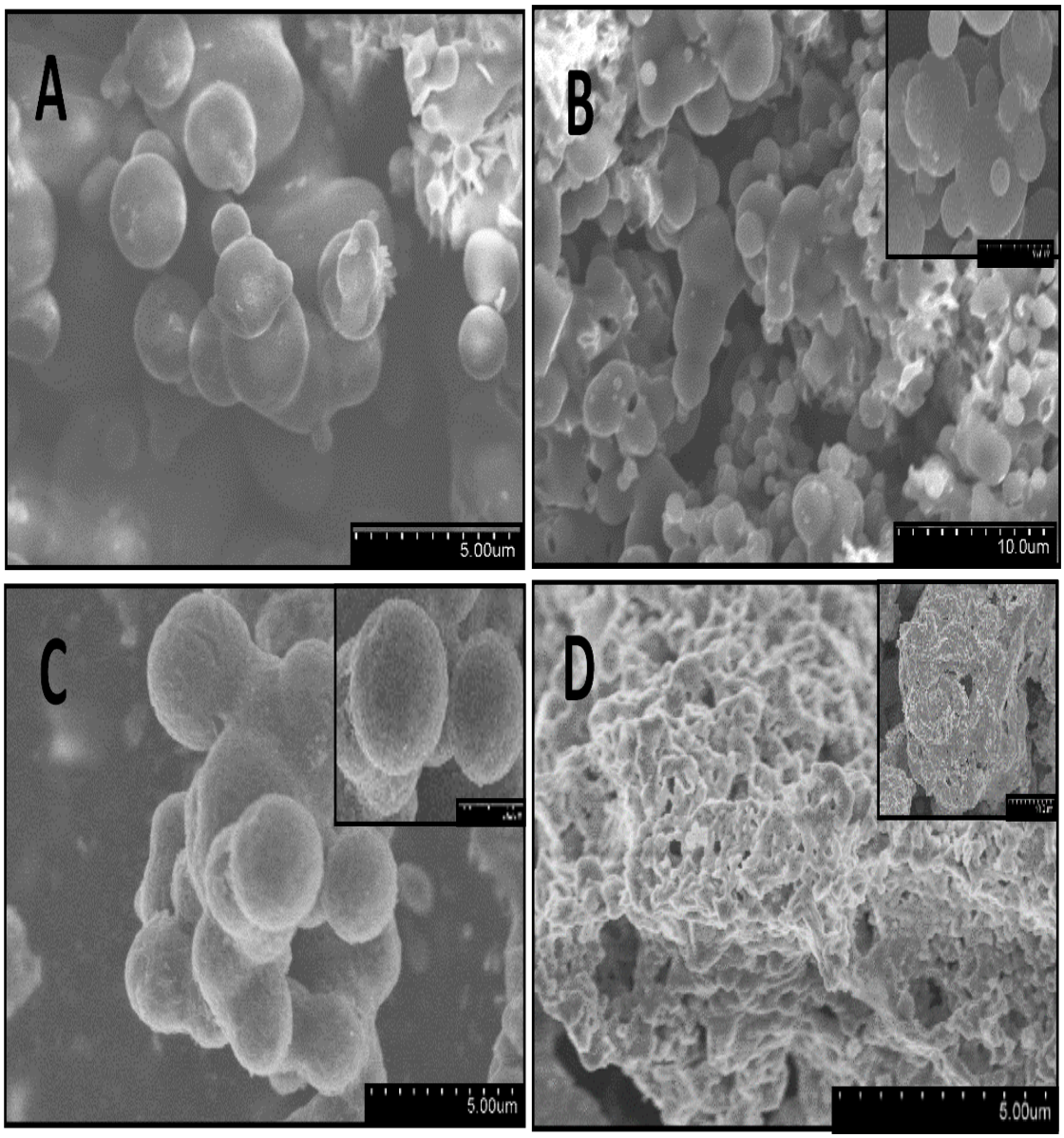

Figure 2-8: Scanning electron micrographs of (A) bio-char, (B) GC1000, (C) MnGC1000, (D) MnGC1000 (before metal removal) (**b)** Nitrogen sorption isotherm and pore size distribution (insets) of graphitic porous carbons.

To probe porosity, nitrogen sorption/desorption isotherms were collected for CoGC1000, FeGC900, GC1000, and MnGC1000 graphitic carbons, as depicted in Figure 2-9 (b). The Brunauer-Emmett-Teller surface area (SA_{BET}) of graphitic carbons was found to be in the range of 150 to 250 $m^2\ g^{-1}$. The surface area and pore size distributions of the GC1000 are similar to those of MnGC1000. FeGC1000 showed higher surface area than GC1000 most likely because Fe-based catalysis is a more effective agent as a surface activation. The pore size distribution curves (Figure 2-9 (b) inset) show that MeGCs and GC1000 have major PSD peaks in the micro-porous and mesoporous ranges suggesting that the resulting carbons have meso- and micro-porous structures.

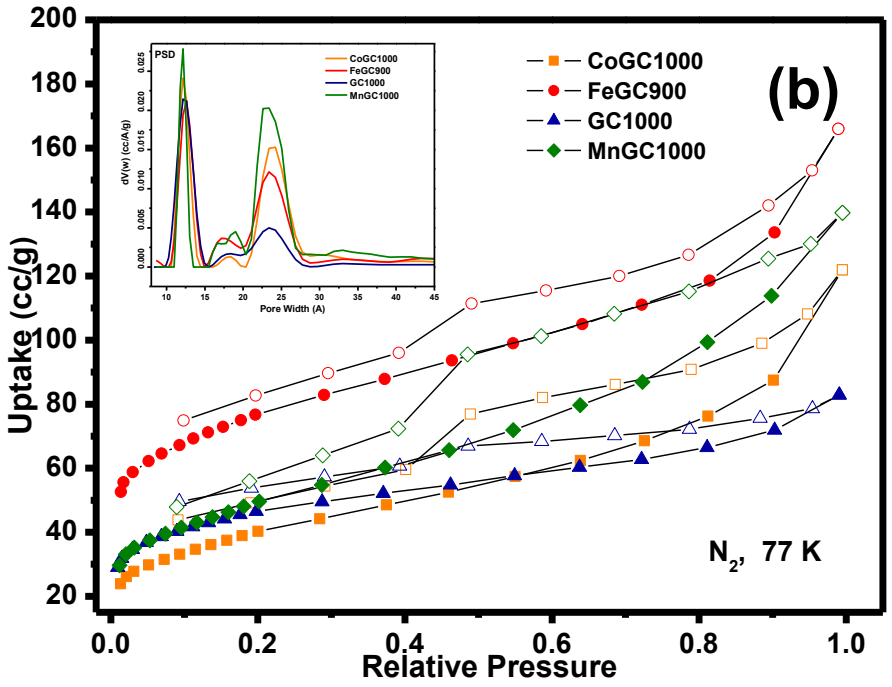

Figure 2-9: Nitrogen uptake at 77 K for metal catalyst graphitic carbons, and the pore size distributions calculated from carbon model using adsorption branch fitted with QSDFT (inset)

2.5.3. Electrical conductivity properties

A Keithley 2636B source-meter was employed to probe the I-V behavior of individual particles. For instance, the I-V curves extracted from representative, single GC1000, and MnGC1000 particles are shown in Figure 2-10. From the linear behavior of these plots, it is evident that an ohmic contact is established between the metal electrode and the graphitic particle. Furthermore, the MnGC1000 particle exhibits a much larger current (an order of magnitude higher) as compared to the GC1000 particle. This substantive increase in electric currents implies a higher electronic conductivity for the MnGC1000 particle, as compared to the GC1000 particle, and is attributed to its higher graphitic content as observed previously within the XRD data (Fig. 6). In order to extract the electronic conductivity of the particle from its resistance value, we have employed an analytical model for the resistance (R_p) of the particle segment, which spans the inter-electrode gap and contributes to electric transport within this device. This is schematically shown in Fig. 3(c-d), where the assembled particle has a radius R, and an inter-electrode suspended length of L_1 and L_2 within the left and right hemispherical components of the particle, respectively. The overall resistance of the particle is the sum of the individual contributions, which arise from the suspended segments of its left-side and right-side hemispherical components. The resistance of each hemispherical component of the particle is obtained by integrating the contributions from infinitesimally thin circular discs that span its thickness (Fig. 3(d)). For instance, the resistance of the suspended segment of the left-side hemispherical particle is calculated as:

$$R_{p1} = \int_0^{L_1} \frac{\rho dx}{A} = \frac{\rho}{\pi} \int_0^{L_1} \frac{dx}{R^2 - x^2} = \frac{\rho}{2\pi R} \ln\left(\frac{R+L_1}{R-L_1}\right) \qquad (2.1)$$

Thus, the overall resistance of the inter-electrode suspended segment of the particle is given as:

$$R_p = R_{p1} + R_{p2} = \frac{\rho}{2\pi R}\left\{\ln\left(\frac{R+L_1}{R-L_1}\right) + \ln\left(\frac{R+L_2}{R-L_2}\right)\right\} \qquad (2.2)$$

While the particle resistance is obtained from the I-V curves of Fig. 9, the geometric parameters such as R, L_1 and L_2 are extracted from the SEM image of the assembled particle (Fig. 3). Substituting these values in Eq. (2), the values for particle resistivity and conductivity have been obtained for representative GC1000 and MnGC1000 particles. These values, which are listed in Table 2, point to an order of magnitude higher value for the conductivity of a MnGC1000 particle as compared to GC1000 particle due to its higher graphitic content. It is important to note that this electrical conductivity measurement approach involving single particles represents an improvement over past reports, which have employed bulk-scale aggregates or powders of particles. This is because measurements with aggregates of particles are influenced not just by the intrinsic conductivity of the particle, but is also impacted by the inter-particle transport impedances. On the other hand, our approach with single particles provides insights into the conductivity of the particle while isolating the inter-particle transport impedance. Although the electrical conductivity of MnGC1000 is lower than pure graphite, graphene and carbo nanotubes, it is still conductivity value of obtained material is higher or comparable than metal oxides, activated carbon, and another type of carbon reported, previously.[5], [67], [68],[6969 7070] It is worthwhile to mention that though electrical conductivity is important criteria for Li-ion anode material, many other properties such as surface properties (area, meso/micro structure), surface functionality, ion-conductivity and mechanical stability.

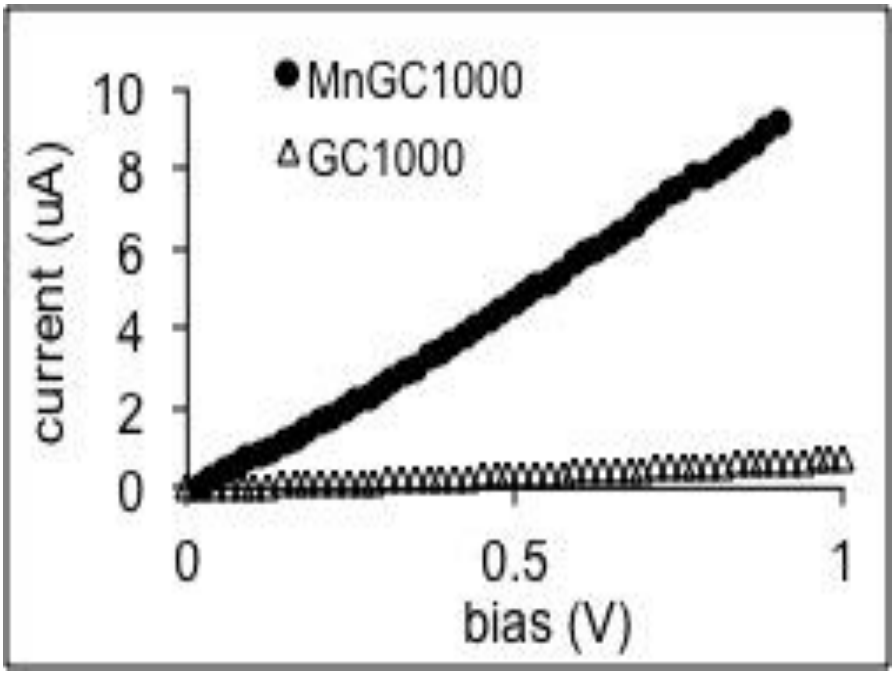

.

Figure 2-10: I-V data acquired from individual MnGC1000 and GC1000 particles

Table 2-4: Electronic conductivity results of MnGC1000 and GC1000 particles

Particle type	**Radius (*R*, nm)**	***L*$_1$ (nm)**	***L*$_2$ (nm)**	**Resistance (R_p, kohm)**	**Resistivity (ohm-m)**	**Conductivity (S-m^{-1})**
MnGC1000	430	362	81	98.8	0.094	10.6
GC1000	346	222	187	1306.8	1.04	0.96

2.6. Conclusions

Lignin can be successfully converted to graphitic carbon via hydrothermal carbonization followed by catalytic graphitization. Cobalt and manganese have been shown higher catalytic

activity than iron for graphitization. In addition, the extent of graphitization is depended on the temperature. A good quality graphitic carbon was obtained using catalysis by $Mn(NO_3)_2$ at 900 °C and $Co(NO_3)_2$ at 1100 °C. The produced material is free of lignin-functional groups, shows high electrical conductivity, has both micro- and mesoporous structures, and is thermally stable.

2.7.References

1. Gogotsi, Y.; Simon, P., True performance metrics in electrochemical energy storage. *Science* **2011,** *334* (6058), 917-918.
2. (a) Liang, J.; Jiao, Y.; Jaroniec, M.; Qiao, S. Z., Sulfur and nitrogen dual-doped mesoporous graphene electrocatalyst for oxygen reduction with synergistically enhanced performance. *Angewandte Chemie International Edition* **2012,** *51* (46), 11496-11500; (b) Nehrir, M.; Wang, C.; Strunz, K.; Aki, H.; Ramakumar, R.; Bing, J.; Miao, Z.; Salameh, Z., A review of hybrid renewable/alternative energy systems for electric power generation: Configurations, control, and applications. *IEEE Transactions on Sustainable Energy* **2011,** *2* (4), 392-403.
3. (a) Odkhuu, D.; Jung, D. H.; Lee, H.; Han, S. S.; Choi, S. H.; Ruoff, R. S.; Park, N., Negatively curved carbon as the anode for lithium ion batteries. *Carbon* **2014,** *66*, 39-47; (b) Armand, M.; Tarascon, J.-M., Building better batteries. *Nature* **2008,** *451* (7179), 652-657.
4. Zheng, H. H.; Qu, Q. T.; Zhang, L.; Liu, G.; Battaglia, V. S., Hard carbon: a promising lithium-ion battery anode for high temperature applications with ionic electrolyte. *Rsc Adv* **2012,** *2* (11), 4904-4912.
5. Wang, H. L.; Dai, H. J., Strongly coupled inorganic-nano-carbon hybrid materials for energy storage. *Chem Soc Rev* **2013,** *42* (7), 3088-3113.
6. (a) Liu, J.; Song, P.; Ning, Z. G.; Xu, W. L., Recent Advances in Heteroatom-Doped Metal-Free Electrocatalysts for Highly Efficient Oxygen Reduction Reaction. *Electrocatalysis-Us* **2015,** *6* (2), 132-147; (b) Dai, L. M.; Xue, Y. H.; Qu, L. T.; Choi, H. J.; Baek, J. B., Metal-Free Catalysts for Oxygen Reduction Reaction. *Chemical Reviews* **2015,** *115* (11), 4823-4892; (c) Zhang, Y.; Zhuang, X. D.; Su, Y. Z.; Zhang, F.; Feng, X. L., Polyaniline nanosheet derived B/N co-doped carbon nanosheets as efficient metal-free catalysts for oxygen reduction reaction. *J Mater Chem A* **2014,** *2* (21), 7742-7746; (d) Gao, S. Y.; Fan, H.; Zhang, S. X., Nitrogen-enriched carbon from bamboo fungus with superior oxygen reduction reaction activity. *J Mater Chem A* **2014,** *2* (43), 18263-18270; (e) Sasaki, K.; Wang, J. X.; Naohara, H.; Marinkovic, N.; More, K.; Inada, H.; Adzic, R. R., Recent advances in platinum monolayer electrocatalysts for oxygen reduction reaction: Scale-up synthesis, structure and activity of Pt shells on Pd cores. *Electrochimica Acta* **2010,** *55* (8), 2645-2652.
7. Buiel, E.; Dahn, J. R., Li-insertion in hard carbon anode materials for Li-ion batteries. *Electrochimica Acta* **1999,** *45* (1-2), 121-130.
8. Datta, M. K.; Kumta, P. N., Silicon and carbon based composite anodes for lithium ion batteries. *J Power Sources* **2006,** *158* (1), 557-563.
9. Li, X. Y.; Chen, Y. M.; Yao, H. M.; Zhou, X. Y.; Yang, J.; Huang, H. T.; Mai, Y. W.; Zhou, L. M., Core/shell TiO2-MnO2/MnO2 heterostructure anodes for high-performance lithium-ion batteries. *Rsc Adv* **2014,** *4* (75), 39906-39911.
10. Kim, Y. J.; Yang, H. J.; Yoon, S. H.; Korai, Y.; Mochida, I.; Ku, C. H., Anthracite as a candidate for lithium ion battery anode. *J Power Sources* **2003,** *113* (1), 157-165.

11. Ishihara, T.; Kawahara, A.; Nishiguchi, H.; Yoshio, M.; Takita, Y., Effects of synthesis condition of graphitic nanocabon tube on anodic property of Li-ion rechargeable battery. *J Power Sources* **2001,** *97-8*, 129-132.
12. Larcher, D.; Beattie, S.; Morcrette, M.; Edstroem, K.; Jumas, J.-C.; Tarascon, J.-M., Recent findings and prospects in the field of pure metals as negative electrodes for Li-ion batteries. *J Mater Chem* **2007,** *17* (36), 3759-3772.
13. Mao, O.; Dahn, J., Mechanically Alloyed Sn-Fe (-C) Powders as Anode Materials for Li-Ion Batteries: III. Sn2Fe: SnFe3 C Active/Inactive Composites. *Journal of The Electrochemical Society* **1999,** *146* (2), 423-427.
14. Poizot, P.; Laruelle, S.; Grugeon, S.; Dupont, L.; Tarascon, J., Nano-sized transition-metal oxides as negative-electrode materials for lithium-ion batteries. *Nature* **2000,** *407* (6803), 496-499.
15. Li, H.; Wang, Z.; Chen, L.; Huang, X., Research on Advanced Materials for Li-ion Batteries. *Adv Mater* **2009,** *21* (45), 4593-4607.
16. Hirsch, A., The era of carbon allotropes. *Nature materials* **2010,** *9* (11), 868-871.
17. Sevilla, M.; Mokaya, R., Energy storage applications of activated carbons: supercapacitors and hydrogen storage. *Energ Environ Sci* **2014,** *7* (4), 1250-1280.
18. Ponrouch, A.; Sevilla, M.; Marchante, E.; Palacin, M. R.; Fuertes, A. B., Facile synthesis of graphitic carbons decorated with SnO2 nanoparticles and their application as high capacity lithium-ion battery anodes. *J Appl Electrochem* **2012,** *42* (11), 901-908.
19. Sevilla, M.; Fuertes, A. B., Graphitic carbon nanostructures from cellulose. *Chemical Physics Letters* **2010,** *490* (1–3), 63-68.
20. Sevilla, M.; Sanchís, C.; Valdés-Solís, T.; Morallón, E.; Fuertes, A. B., Direct synthesis of graphitic carbon nanostructures from saccharides and their use as electrocatalytic supports. *Carbon* **2008,** *46* (6), 931-939.
21. Dillon, A.; Heben, M., Hydrogen storage using carbon adsorbents: past, present and future. *Applied Physics A* **2001,** *72* (2), 133-142.
22. Catalao, R.; Maldonado-Hódar, F.; Fernandes, A.; Henriques, C.; Ribeiro, M., Reduction of NO with metal-doped carbon aerogels. *Applied Catalysis B: Environmental* **2009,** *88* (1), 135-141.
23. Sevilla, M.; Martínez-de Lecea, C. S.; Valdés-Solís, T.; Morallón, E.; Fuertes, A., Solid-phase synthesis of graphitic carbon nanostructures from iron and cobalt gluconates and their utilization as electrocatalyst supports. *Phys Chem Chem Phys* **2008,** *10* (10), 1433-1442.
24. Sevilla, M.; Gu, W.; Falco, C.; Titirici, M. M.; Fuertes, A. B.; Yushin, G., Hydrothermal synthesis of microalgae-derived microporous carbons for electrochemical capacitors. *J Power Sources* **2014,** *267*, 26-32.
25. Jimenez-Morales, I.; Moreno-Recio, M.; Santamaria-Gonzalez, J.; Maireles-Torres, P.; Jimenez-Lopez, A., Production of 5-hydroxymethylfurfural from glucose using aluminium doped MCM-41 silica as acid catalyst. *Appl Catal B-Environ* **2015,** *164*, 70-76.
26. Liu, H.; Jin, L.-H.; He, P.; Wang, C.; Xia, Y., Direct synthesis of mesoporous carbon nanowires in nanotubes using MnO 2 nanotubes as a template and their application in supercapacitors. *Chem Commun* **2009,** (44), 6813-6815.
27. Liu, Y.; Liu, Q.; Gu, J.; Kang, D.; Zhou, F.; Zhang, W.; Wu, Y.; Zhang, D., Highly porous graphitic materials prepared by catalytic graphitization. *Carbon* **2013,** *64* (0), 132-140.
28. Zhai, D.; Du, H.; Li, B.; Zhu, Y.; Kang, F., Porous graphitic carbons prepared by combining chemical activation with catalytic graphitization. *Carbon* **2011,** *49* (2), 725-729.
29. Gutiérrez-Pardo, A.; Ramírez-Rico, J.; de Arellano-López, A. R.; Martínez-Fernández, J., Characterization of porous graphitic monoliths from pyrolyzed wood. *J Mater Sci* **2014,** *49* (22), 7688-7696.

30. Antisari, M. V.; Montone, A.; Jovic, N.; Piscopiello, E.; Alvani, C.; Pilloni, L., Low energy pure shear milling: a method for the preparation of graphite nano-sheets. *Scripta Mater* **2006,** *55* (11), 1047-1050.
31. Fu, T.; Lv, J.; Li, Z., Effect of Carbon Porosity and Cobalt Particle Size on the Catalytic Performance of Carbon Supported Cobalt Fischer–Tropsch Catalysts. *Ind Eng Chem Res* **2014,** *53* (4), 1342-1350.
32. Ōya, A.; Ōtani, S., Catalytic graphitization of carbons by various metals. *Carbon* **1979,** *17* (2), 131-137.
33. Marsh, H.; Crawford, D.; Taylor, D. W., Catalytic graphitization by iron of isotropic carbon from polyfurfuryl alcohol, 725–1090 K. A high resolution electron microscope study. *Carbon* **1983,** *21* (1), 81-87.
34. Logeswari, J.; Pandurangan, A.; Sangeetha, D., An Efficient Catalyst for the Large Scale Production of Multi-Walled Carbon Nanotubes. *Ind Eng Chem Res* **2011,** *50* (23), 13347-13354.
35. Lei, Z.; Xiao, Y.; Dang, L.; You, W.; Hu, G.; Zhang, J., Nickel-Catalyzed Fabrication of SiO2, TiO2/Graphitized Carbon, and the Resultant Graphitized Carbon with Periodically Macroporous Structure. *Chemistry of Materials* **2006,** *19* (3), 477-484.
36. Sevilla, M.; Fuertes, A. B., Catalytic graphitization of templated mesoporous carbons. *Carbon* **2006,** *44* (3), 468-474.
37. Huang, C.-h.; Doong, R.-a.; Gu, D.; Zhao, D., Dual-template synthesis of magnetically-separable hierarchically-ordered porous carbons by catalytic graphitization. *Carbon* **2011,** *49* (9), 3055-3064.
38. Zhang, Y.; Zhang, X.; Zhang, H.; Zhao, Z.; Li, F.; Liu, C.; Cheng, H., Composite anode material of silicon/graphite/carbon nanotubes for Li-ion batteries. *Electrochimica acta* **2006,** *51* (23), 4994-5000.
39. Liu, J.; Xue, D., Hollow nanostructured anode materials for Li-ion batteries. *Nanoscale Res Lett* **2010,** *5* (10), 1525.
40. Yoo, E.; Kim, J.; Hosono, E.; Zhou, H.-s.; Kudo, T.; Honma, I., Large reversible Li storage of graphene nanosheet families for use in rechargeable lithium ion batteries. *Nano letters* **2008,** *8* (8), 2277-2282.
41. Elizabeth, I.; Singh, B. P.; Trikha, S.; Gopukumar, S., Bio-derived hierarchically macro-meso-micro porous carbon anode for lithium/sodium ion batteries. *J Power Sources* **2016,** *329*, 412-421.
42. Praneetha, S.; Murugan, A. V., Development of Sustainable Rapid Microwave Assisted Process for Extracting Nanoporous Si from Earth Abundant Agricultural Residues and Their Carbon-based Nanohybrids for Lithium Energy Storage. *Acs Sustain Chem Eng* **2015,** *3* (2), 224-236.
43. Lotfabad, E. M.; Ding, J.; Cui, K.; Kohandehghan, A.; Kalisvaart, W. P.; Hazelton, M.; Mitlin, D., High-density sodium and lithium ion battery anodes from banana peels. *Acs Nano* **2014,** *8* (7), 7115-7129.
44. Ou, J.; Zhang, Y.; Chen, L.; Zhao, Q.; Meng, Y.; Guo, Y.; Xiao, D., Nitrogen-rich porous carbon derived from biomass as a high performance anode material for lithium ion batteries. *J Mater Chem A* **2015,** *3* (12), 6534-6541.
45. Li, Z.; Ding, J.; Mitlin, D., Tin and tin compounds for sodium ion battery anodes: phase transformations and performance. *Accounts of chemical research* **2015,** *48* (6), 1657-1665.
46. Penki, T. R.; Shanmughasundaram, D.; Kishore, B.; Munichandraiah, N., High rate capability of coconut kernel derived carbon as an anode material for lithium-ion batteries. *Adv Mat Lett* **2014,** *5* (4), 184-190.
47. Zhang, Y.; Chen, L.; Meng, Y.; Xie, J.; Guo, Y.; Xiao, D., Lithium and sodium storage in highly ordered mesoporous nitrogen-doped carbons derived from honey. *J Power Sources* **2016,** *335*, 20-30.
48. Selvamani, V.; Ravikumar, R.; Suryanarayanan, V.; Velayutham, D.; Gopukumar, S., Fish scale derived nitrogen doped hierarchical porous carbon—a high rate performing anode for lithium ion cell. *Electrochimica Acta* **2015,** *182*, 1-10.
49. Gu, H.; Zhu, Y. E.; Yang, J.; Wei, J.; Zhou, Z., Nanomaterials and Technologies for Lithium-Ion Hybrid Supercapacitors. *ChemNanoMat* **2016**.
50. (a) Zhang, L.; Liu, Z.; Cui, G.; Chen, L., Biomass-derived materials for electrochemical energy storages. *Progress in Polymer Science* **2015,** *43*, 136-164; (b) Jiang, J.; Zhu, J.; Ai, W.; Fan, Z.; Shen, X.; Zou,

C.; Liu, J.; Zhang, H.; Yu, T., Evolution of disposable bamboo chopsticks into uniform carbon fibers: a smart strategy to fabricate sustainable anodes for Li-ion batteries. *Energ Environ Sci* **2014,** *7* (8), 2670-2679; (c) Wang, P.; Qiao, B.; Du, Y.; Li, Y.; Zhou, X.; Dai, Z.; Bao, J., Fluorine-Doped Carbon Particles Derived from Lotus Petioles as High-Performance Anode Materials for Sodium-Ion Batteries. *The Journal of Physical Chemistry C* **2015,** *119* (37), 21336-21344.

51. Hou, J.; Cao, C.; Ma, X.; Idrees, F.; Xu, B.; Hao, X.; Lin, W., From Rice Bran to High Energy Density Supercapacitors: A New Route to Control Porous Structure of 3D Carbon. *Sci Rep-Uk* **2014,** *4*.

52. Kubo, S.; Uraki, Y.; Sano, Y., Catalytic graphitization of hardwood acetic acid lignin with nickel acetate. *J Wood Sci* **2003,** *49* (2), 188-192.

53. Chatterjee, S.; Jones, E. B.; Clingenpeel, A. C.; McKenna, A. M.; Rios, O.; McNutt, N. W.; Keffer, D. J.; Johs, A., Conversion of Lignin Precursors to Carbon Fibers with Nanoscale Graphitic Domains. *Acs Sustain Chem Eng* **2014,** *2* (8), 2002-2010.

54. Popova, O. V.; Serbinovskii, M. Y., Graphite from hydrolysis lignin: Preparation procedure, structure, properties, and application. *Russ. J. Appl. Chem.* **2014,** *87* (6), 818-823.

55. Ramsurn, H.; Kumar, S.; Gupta, R. B., Enhancement of biochar gasification in alkali hydrothermal medium by passivation of inorganic components using Ca (OH) 2. *Energy & Fuels* **2011,** *25* (5), 2389-2398.

56. Subramanian, A.; Hudak, N. S.; Huang, J. Y.; Zhan, Y.; Lou, J.; Sullivan, J. P., On-chip lithium cells for electrical and structural characterization of single nanowire electrodes. *Nanotechnology* **2014,** *25* (26), 265402.

57. Didi, X.; Subramanian, A.; Lixin, D.; Nelson, B. J., Shaping Nanoelectrodes for High-Precision Dielectrophoretic Assembly of Carbon Nanotubes. *Nanotechnology, IEEE Transactions on* **2009,** *8* (4), 449-456.

58. Palapati, N. K. R.; Pomerantseva, E.; Subramanian, A., Single nanowire manipulation within dielectrophoretic force fields in the sub-crossover frequency regime. *Nanoscale* **2015,** *7* (7), 3109-3116.

59. Tang, J.; Wang, T.; Sun, X.; Guo, Y.; Xue, H.; Guo, H.; Liu, M.; Zhang, X.; He, J., Effect of transition metal on catalytic graphitization of ordered mesoporous carbon and Pt/metal oxide synergistic electrocatalytic performance. *Microporous and Mesoporous Materials* **2013,** *177* (0), 105-112.

60. Wang, Z. L.; Zhang, X. B.; Liu, X. J.; Lv, M. F.; Yang, K. Y.; Meng, J. A., Co-gelation synthesis of porous graphitic carbons with high surface area and their applications. *Carbon* **2011,** *49* (1), 161-169.

61. Fu, R.; Baumann, T. F.; Cronin, S.; Dresselhaus, G.; Dresselhaus, M. S.; Satcher, J. H., Formation of Graphitic Structures in Cobalt- and Nickel-Doped Carbon Aerogels. *Langmuir* **2005,** *21* (7), 2647-2651.

62. Ōya, A.; Marsh, H., Phenomena of catalytic graphitization. *J Mater Sci* **1982,** *17* (2), 309-322.

63. Sadezky, A.; Muckenhuber, H.; Grothe, H.; Niessner, R.; Pöschl, U., Raman microspectroscopy of soot and related carbonaceous materials: spectral analysis and structural information. *Carbon* **2005,** *43* (8), 1731-1742.

64. Xiong, H.; Schwartz, T. J.; Andersen, N. I.; Dumesic, J. A.; Datye, A. K., Graphitic-Carbon Layers on Oxides: Toward Stable Heterogeneous Catalysts for Biomass Conversion Reactions. *Angewandte Chemie International Edition* **2015,** *54* (27), 7939-7943.

65. Qin, H.; Kang, S.; Huang, Y.; Liu, S.; Fang, Y.; Li, X.; Wang, Y., Lignin based synthesis of carbon nanocages assembled from graphitic layers with hierarchical pore structure. *Mater Lett* **2015,** *159*, 463-465.

66. Okpalugo, T. I. T.; Papakonstantinou, P.; Murphy, H.; McLaughlin, J.; Brown, N. M. D., High resolution XPS characterization of chemical functionalised MWCNTs and SWCNTs. *Carbon* **2005,** *43* (1), 153-161.

67. Roberts, A. D.; Li, X.; Zhang, H. F., Porous carbon spheres and monoliths: morphology control, pore size tuning and their applications as Li-ion battery anode materials. *Chem Soc Rev* **2014,** *43* (13), 4341-4356.

68. Li, B.; Zhang, Q. Y.; Zhang, C. L.; Kang, S. F.; Li, X.; Wang, Y. G., One-step Nanocasting Synthesis of Mesostructured TiO2/graphitic Carbon Composite as an Anode Material for Lithium-Ion Battery. *Int J Electrochem Sc* **2013,** *8* (6), 8414-8421.
69. Zhang, B. A.; Xu, Z. L.; Kim, J. K., In situ grown graphitic carbon/Fe2O3/carbon nanofiber composites for high performance freestanding anodes in Li-ion batteries. *Rsc Adv* **2014,** *4* (24), 12298-12301.
70. Ashourirad, B.; Arab, P.; Islamoglu, T.; Cychosz, K. A.; Thommes, M.; El-Kaderi, H. M., A cost-effective synthesis of heteroatom-doped porous carbons as efficient CO 2 sorbents. *J Mater Chem A* **2016,** *4* (38), 14693-14702.

3. Chapter 3. Lignin Biomass-derived N-doped Carbon Electrode Material for Supercapacitors

3.1.Supercapacitor

In last decade, energy storage and conversion technology have drawn a great deal of attention due to the growing demand for sustainable and renewable energy. Electrochemical Supercapacitor (ES), also known as electro-double layer capacitors, are high power storage devices.[1] In the last decades, ES has received much attention because of high power density, fast charge-discharge rate, and exceptional cyclability.[2,3] ES has been extensively implemented in variety applications such as electronic devices, hybrid electric vehicles, memory backup etc.[4] ES is different than traditional capacitor in regard to the energy and power density. The traditional capacitor has extreme power density which releases a plenty of energy in an instant time (high power output) however its energy density is too low to deliver energy output to accelerate vehicles constantly. Thus, the capacitor has been combined with the battery in order to supply the sufficient power requirements in electric vehicle systems. Because of lack of energy density in the traditional capacitor, the aim of ES is to enhance the energy density thereby a high-powered output can be delivered for a long period of time.

There are three types of supercapacitors classified according to the charge storage mechanism: electric double layer capacitors (EDLCs), pseudo-capacitors and hybrid capacitors[5,6] as shown in Figure 3-2. EDLCs are known as electrochemical capacitors, which store the charge electrostatically between the interface of the electrolyte and surface of active materials. The charge storage in EDLC is non-faradaic, slow and by reversible ion adsorption. Activated carbon is a well-known example for EDLC. In contrast, pseudo-capacitors (PC) store charge by reversible redox

reaction which is a faradaic and fast process.[7,8] The faradic process has been described as an electrochemical reaction on the electrode surface. Hence, this reaction changes the oxidation state of the surface during the charge/discharge process. For PC, the main portion of charge has been stored by EDLC while pseudocapacitance responsible for a small portion of capacitance. [9]

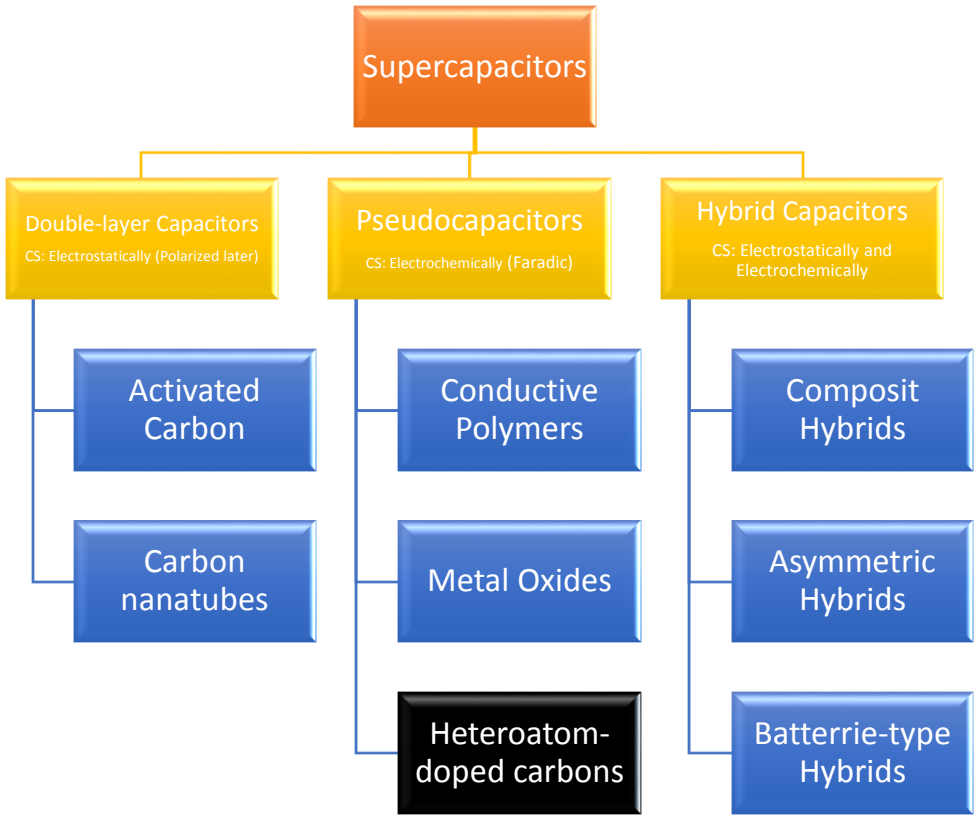

Figure 3-1: Hierarchical classification of supercapacitors

3.2.Performance of supercapacitor

The supercapacitor consists of an anode, a cathode and a current collector. Each electrode immersed in an electrolyte separated by a separator. When a voltage potential is applied across the current collectors, the negative electrode attracts positive ions in the electrolyte, while the potential

on the positive electrode attracts negative ions. The charge accumulated at both electrode surfaces generates energy when discharging.[10],[11] Working principle of electro double layer capacitor is depicted in Figure 3-1. Three component, including electrode, electrolyte, and separator, are key parameters to affect the high performance of supercapacitor device. Especially, the electrodes are an important element for charge/discharge process which is responsible for energy and power densities of a supercapacitor. Recently, porous activated carbon (PAC),[12] metal oxide,[13] conductive polymers,[14] graphene[15] and carbon nanotubes[16] have been utilized as a potential electrode materials in energy storage technology.[17,18] Desired supercapacitor electrode material needs to have following criteria,

(1) extremely high power density,

(2) high energy density,

(3) the high surface area with hierarchical porosity(especially for EDLC) ,

(4) long cycling durability of electrodes,

(5) fast charge/discharge processes within seconds

(6) Low cost,

(7) and safe operation[19],[20]

The following section discusses recent advancements in various electrode materials for supercapacitor applications.

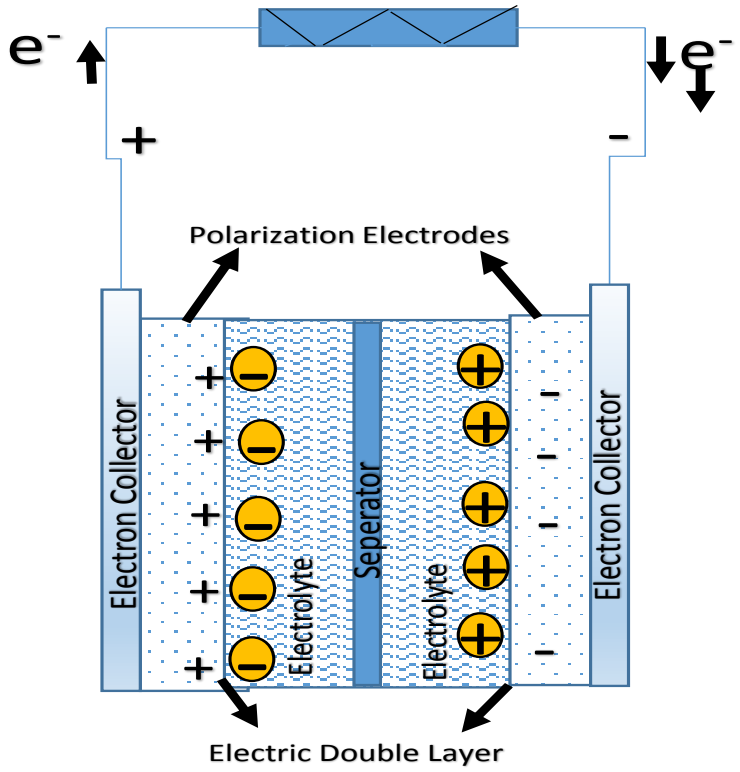

Figure 3-2: Working principle of supercapacitor

3.3.Metal Oxides

Metal oxides are known as a best active electrode material for pseudo type-capacitance. Application of metal oxide-based PC is limited due to their low surface area and high-cost production process.[21,22,23,24] As it mentioned above, pseudo-capacitance is electrochemical reaction faradic reaction where fast and reversible redox reactions take place between the electrolyte and certain electro-active sites on the electrode surface. Ruthenium oxide has been widely applied as a PC electrode material thanks to its intrinsic reversibility of surface redox couples and high conductivity. The specific capacitance of amorphous hydrous ruthenium oxide

(RuO2.*xH2O*) has been found up to 720 F/g (1300 to 2200 F g^{-1} theoretical capacitance). Following redox reaction has been proposed for this material,

$$RuO_x(OH)_y + \delta H^+ + \delta e^- \leftrightarrow RuO_{x-\delta}(OH)_{y+\delta} \quad (3.1)$$

where $RuO_x(OH)_y$ and $RuO_{x-\delta}(OH)_{y+\delta}$ represent at higher and lower oxidation states of ruthenium species. This reaction ensures reversible fast redox reaction due to the hydrous nature of ruthenium surface. In a short, the well-designed metal-oxide particle exhibits an advance electrode material for energy storage. However, the cost of precious metal oxide and harsh manufacturing condition for large scale process hinder widely marketplace applications. ·

3.4. Conductive Polymers

Conductive polymers have been explored as an electrode material in energy storage technology. Polyaniline (PANI) is a well-known example for a conductive polymer. The specific capacitance of modified PANI has been reached up to 100 F/g in a solid poly (vinylidene fluoride-co-hexafluoropropylene) electrolyte. Polyaniline electrodes had been used in combination with carbon nanotubes (CNT) that exhibited a capacitance of 328 F/g. In another example, as-synthetized polypyrrole/nanofiber composite reached a specific capacitance of 545 F/g. However, the most important drawback of conductive polymer electrode is their deficient cycling life due to faradic reaction through the charge/discharge process which limits practical application.[14,25]

3.5. Carbon based electrode materials

Carbon-based materials have been traditionally utilized as a supercapacitor electrodes due to the consequently high capacitance, large BET surface area, and relatively mild manufacturing conditions. Although commercially available carbons from such as Maxwell Technologies and Panasonic have shown capacitances in the 5 and 10 F g^{-1}, lab-scale carbons have reached a specific capacitance of over 200 F g^{-1}. , but these materials have not yet been turned into commercially viable products.[12] The oldest and most common of electric double layer capacitors material is activated carbon owing to its high BET surface area, excellent stability, an abundance of raw materials and moderate cost.[8,26,27] However, AC still suffers from its low electron/ionic conductivity, lack of pseudocapacitive properties which lead poor energy/power density, and low electrochemical performance for energy storage material. Low electrical conductivity for AC is because of its disordered structure, lacking graphene content.[6,7,28] Moreover, although the AC has large BET surface areas, pore size distribution of AC exhibits only microporous characteristics (micropore distributions ranging from 0.5 to 1.1 nm). This poor pore size distribution causes low performance of ion transport due to the inadequate ionic diffusion pathway within the narrow micropores. This limitation greatly hinders practical applications of AC in high energy/power density supercapacitors.[29,30] Therefore, it is essential to develop 3D hierarchically pore structure with abundant micropores (responsible for the charge accumulation), interconnected mesoporous (the role of decreasing the ion diffusion distance) and appropriate macropores (in charge of ion-buffering reservoirs to store more electrolyte ions).[31,32] Recently, many methods such as silica oxides or metallic compounds have been reported for synthesizing of hierarchically porous carbons[33,34]. However, these methods still have not been in practical application due to the

consumption of high-cost templates, and time. Thus, it is of the utmost importance to develop a simple and inexpensive method for fabricating of 3D hierarchically porous carbon.

3.6.Heteroatom-doped carbon electrodes

Due to shortcomings of ACs, the researchers have been examining alternative ways to enhance electrical conductivity, surface wettability and the specific capacitance of activated carbon materials. Heteroatom-doped carbons offer a possible solution to optimizing the performance of supercapacitors to have high surface area, high electrical conductivity and a high number of electrochemically active sites. Heteroatom doping leads enhancing the electrical and ionic conductivity of carbon molecules by supplying extra electron delocalization along with the structure. Such atoms provide extra pseudo-capacitance, increase the surface wettability and electronic conductivity of carbons, and hence increase the capacitance of the final material. [35,36,37,38] Thus, heteroatom-doped carbon structure is a promising way to enhance the electrochemical activity of electrode materials. The possible mechanism of N-doped carbon for pseudo-capacitance in aqueous solution was reported by following equations [39]

$$-CH\text{-}NH_2 + 2OH^- \Leftrightarrow -C{=}NH + H_2O + 2e^- \quad (3.2)$$

$$-C\text{-}NH_2 + 2OH^- + 2H^+ \Leftrightarrow -C\text{-}NHOH + H_2O + 2e^- \quad (3.3)$$

and oxygen-containing functional groups

$$>C\text{-}OH \Leftrightarrow >C{=}O + H^+ + e^- \quad (3.4)$$

$$-COOH \Leftrightarrow -COO + H^+ + e^- \quad (3.5)$$

$$>C{=}O + e^- \Leftrightarrow -C\text{-}O^- \quad (3.6)$$

3.7. Synthesis of heteroatom-doped carbon

There are two main techniques to prepare heteroatom-doped carbons. The first technique involves the carbonization of heteroatom-containing precursors such as polypyrrole[40], polyaniline[41], polyacrylonitrile[42] and melamine analogues[43] etc. The second technique involves heteroatom introduction through annealing treatment of carbon materials with nitrogen rich agents such as ammonia, pyrrole, nitrogen plasma or urea.[44,45,46]. Nonetheless, the reagents/chemicals used in both techniques are mainly produced from petroleum. Materials based on environmentally benign and sustainable renewable resources need to be produced to reduce the dependency on petroleum in the production of these materials.[47,48,49]. Significant research efforts have thus been devoted to preparing heteroatom-incorporated carbonaceous materials from natural resources like bacteria[26], fungi[50], and sucrose.[24] On the other hand, practical synthesis of this carbon source is still insufficient due to the limited resources thus, more abundant and sustainable biomass is necessary for large-scale manufacturing.

3.8. N-doped carbon from lignin

The capacitance property of carbonaceous materials derived from above natural sources still needs to be improved for practical applications. As such, it is important to develop high-performance supercapacitor electrode materials from an abundant, inexpensive, sustainable and renewable natural resource. To this end, byproduct lignin presents an excellent feedstock for production of supercapacitor electrode material. Lignin, a complex biopolymer composed of aromatic alcohols, is one of the most abundant materials in nature.[51] Lignin is a high volume byproduct generated in the pulp and paper industry. Most of the lignin is currently in-efficiently burned to generate steam and electricity.[52] In recent years, intensive research efforts have been

directed toward converting lignin into high added value materials. For instance, current applications of lignin are in concrete admixtures, graphitic carbon, animal feed pellets, road-side dust control, and as dispersing, wetting, binding agents, etc. [53],[54],[55] However, since the supply of the unused lignin is in great excess, it is highly desirable to convert lignin into additional high-value products.

Recently, several reports documented the use of lignin to generate porous carbons in supercapacitors.[56,57,58,59,60,61] However, to the best of our knowledge, lignin-derived N-doped carbon materials have not yet been reported as an electrode material for supercapacitors. In this dissertation, lignin was converted into N-doped carbon materials using a two-step conversion process. Lignin was first converted into bio-char by hydrothermal carbonization followed by conversion of the bio-char into N-doped carbons via annealing treatment in the presence of adenine and KOH. Here, it was also examined the effect of adding adenine and KOH into bio-char, and process conditions which can further increase the capacitance over what has been achieved so far.

Here the key objectives for this work are:

1) to construct electrode materials with high surface area with micro/meso porosity,

2) to explore and understand the roles of nitrogen doping in terms of the capacitive behavior,

3) to improve the capacitance properties through enhancing the affinity between the carbon and nitrogen molecules,

4) to construct stable electrode material which is important properties of supercapacitor materials, and

5) to device a scalable and effective production pathway.

3.9.Experimental

3.9.1. Materials

Organosolv Lignin was obtained from Lignol Innovation Company. Adenine ($C_5H_5N_5$, 99%), potassium hydroxide (KOH), and carbon black were purchased from Alfa Aesar. Ni foam was purchased from MTI Corporation. Polytetrafluoroethylene (PTFE, 60 wt.% dispersion in H_2O) was obtained from Aldrich. All chemicals were used as received. Deionized water (18.2 MΩ·cm) was used in the hydrothermal treatments.

3.9.2. Synthesis of bio-char

Bio-char was prepared by hydrothermal carbonization (HTC) of lignin using in-situ ultra-sonication (photography of reactor was depicted in Figure 3-1.). The reactor equipped with sonication increases mass transfer of solvent into the solid state materials; as a result, the removal of the oxygen content of lignin into solvent was enhanced. In a typical synthesis, 10 g of lignin were mixed with deionized water (80 mL) and charged into sonicated Col-Int reactor. The temperature and pressure of the reactor were maintained at 300 ℃ and 103 bar, respectively, for

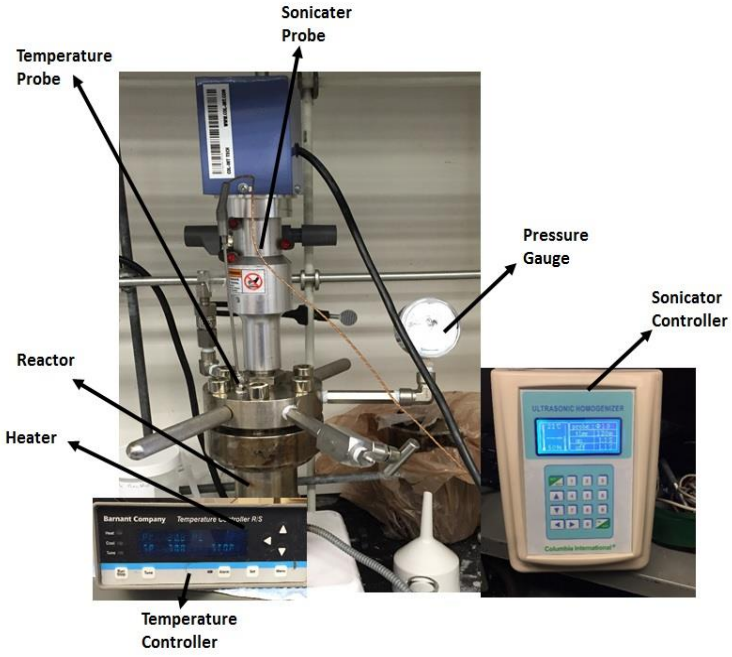

Figure 3-1: Photography of the HTC reactor

30 min soaking time.[62] The reactor was then allowed to cool down to room temperature and the resultant bio-char was removal by filtration.

3.9.3. Synthesis of N-doped carbon material

N-doped porous carbons were synthesized by the annealing treatment of the bio-char in presence of KOH and adenine as activation agent and a nitrogen source, respectively. In a typical procedure, KOH (6 g) was dissolved in deionized water (25 mL). Then, adenine (1.5 g) and bio-char (1.5 g) were added to the KOH aqueous solution and stirred for 30 min. The reaction mixture was transferred into a 50 mL Teflon-lined stainless autoclave and then heated to 90 ^{o}C for 10 h. The obtained brown product was filtered and dried at 90 ^{o}C overnight. The dried sample was annealed at a given temperature (700, 850 and 1000 ^{o}C) for 1 h under N_2 flow at a heating rate of 5 °C/min by using a Carbolite (MTF250) tubular furnace shown in Figure 3-2.

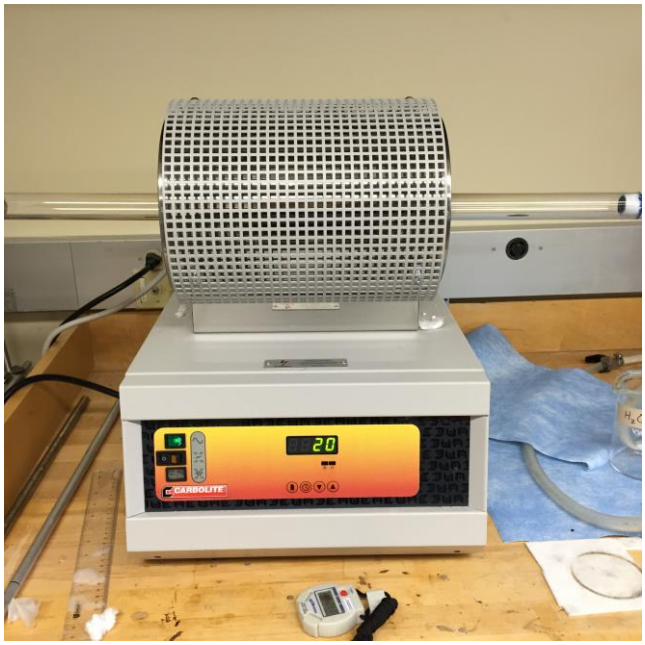

Figure 3-2: Photography of the tubular furnace

3.9.4. Characterization

FTIR spectra of samples were obtained using a Smart ATR Nicolet Nexus 670 FT-IR spectrometer. An adequate amount of sample was placed directly on a diamond tip and spectra obtained from 4000 to 400 cm^{-1} range with a resolution of 4 cm^{-1} and averaging 16 scans. The graphitic and amorphous carbon contents in the as-prepared materials were examined by Raman spectroscopy (Horiba LABRam HR; excitation wavelength = 532 nm). The Brunauer-Emmett-Teller (BET) specific surface area and pore size distributions were gathered by an Autosorb iQ (Qantachrome) surface analyzer. Pore size distribution maxima calculated using N_2 isotherm at 77 K on carbon model (slit/cylinder. pores, QSDFT adsorption branch). The micro pore volume was determined by cumulative pore volume at 2 nm maxima of the PSD assuming slit/cylindrical shaped pores and QSDFT model. Total pore volume was measured at P/Po equal 0.95. Thermal stability test of the synthesized materials was performed using a Perkin thermo-gravimetric analyzer. Operating conditions were fixed to a constant heating rate of 5 °C/min with N_2 flow (ranging from 50 to 800 °C). Scanning electron microscope (SEM) (Hitachi SU-70 FE-SEM) images were obtained to examine the morphology of the N-doped materials. The SEM instrument was operated at 5 kV under vacuum. X-ray photoelectron spectroscopy (ESCAlab 250) was conducted in order to examine the chemical composition (C, O, N) and nature of the functionalized groups on the surface of the prepared materials.

3.9.5. Electrochemical measurement

The electrochemical performance of the as-synthesized N-doped carbons was investigated by means of cyclic voltammetry (CV), galvanostatic charge-discharge measurements and electrochemical impedance spectroscopy (EIS) on a CHI 660E electrochemical workstation at room temperature. The supercapacitor working electrode (NC-x electrode), was fabricated as

following: an 80 wt.% active electrode material (NC-x), 10 wt.% carbon black (Alfa Aesar) and 10 wt.% binder (polytetrafluoroethylene: PTFE, 60 wt.% dispersion in H_2O, Aldrich) were mixed together until a slurry of proper viscosity obtained.[19] The viscous slurry was casted onto a current collector (nickel foam, 1.5 cm x 3 cm) and dried at 80 °C for 12 h in vacuum. In order to achieve a good electronic contact, the dried electrode was then uniaxially pressed at 5 tons. The geometric surface area of the prepared electrode was 0.32 cm^2. The as-prepared electrode before and after taping was illustrated in Figure3-3.

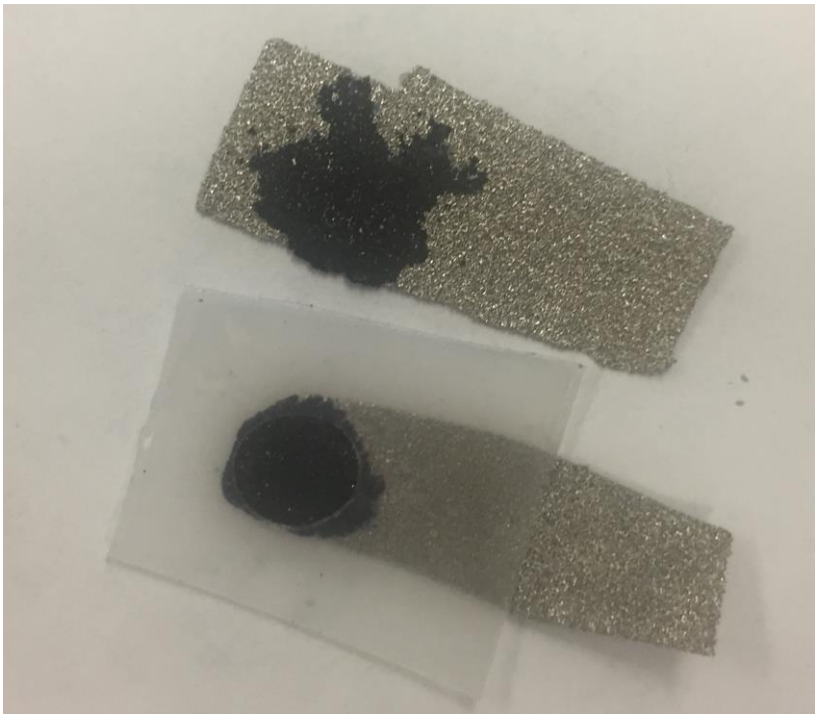

Figure 3-3: Photography of prepared electrodes (before and after taping)

All the electrochemical measurements were conducted in 1 M KOH aqueous solution with a three-electrode configuration equipped with the as-prepared NC-x working electrode, Pt wire (CH Instruments Inc.) auxiliary electrode and Ag/AgCl (1 M KCl solution) (CH Instruments Inc.) as reference electrodes depicted in Figure 3-4. The voltage range for CV measurements was -1.0 to 0.0 V (*vs*. Ag/AgCl) at scan rates of 1, 5, 10, 20, 50 and 100 mV s^{-1}. Galvanostatic charge-discharge tests were performed at current densities of 1, 2, 5, 8, 10, 15, and 20 A g^{-1} within the potential range of -1.0 to 0.0 V (vs. Ag/AgCl). The EIS data were collected in a frequency range of 10 MHz to 500 kHz with a 5 mV AC amplitude.

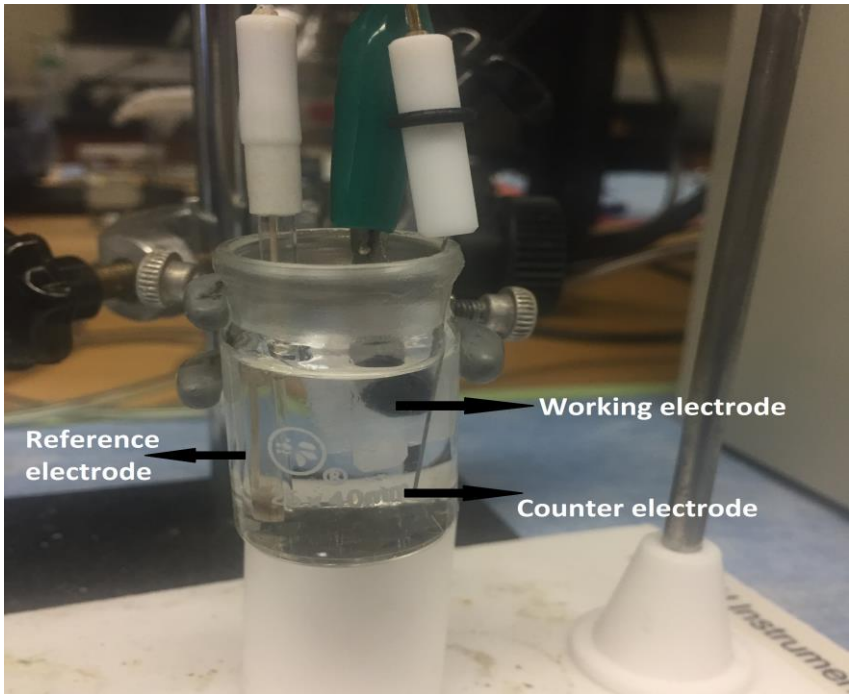

Figure 3-4: Scheme of a three electrode cell for electrochemical characterization

The gravimetric specific capacitance (C_s, F g^{-1}) of the NC-x electrodes was calculated from the galvanostatic discharge curves according to the equation (3.3).

$$C_s = \frac{I\Delta t}{m\Delta V} \qquad (3.3)$$

where I is the discharge current (A), ΔV is discharging voltage, m is the mass of the active electrode material (g) and Δt is the discharge time. The following equation (2) was also used to calculate the specific capacitance (C_s, F g^{-1}) from the cyclic voltammograms:

$$C_s = \frac{\int_{v_1}^{v_n} IdV}{mv\Delta V} \qquad (3.4)$$

where m is the mass of the active electrode material (g), v is the scan rate (V s^{-1}), ΔV is the potential window for the CV measurement and $\int_{v_1}^{v_n} IdV$ is from the integration of the cyclic voltammetry curve [63],

The volumetric specific capacitance (C_v, F/$cm^{3)}$ was calculated by the following equation:

$$C_v = \rho C_s \qquad (3.5)$$

where C_s is specific capacitance, ρ is particle density calculated by equation 4:

$$\rho = \frac{1}{V_t + (1/\rho_t)} \qquad (3.6)$$

V_t is total pore volume cm^3 /g and ρ_t is true density of carbon (2 g/cm^3).[64]

The specific capacitance (C_s, F g^{-1}) from the cyclic voltammetry was used to obtain the energy density (E, Wh kg^{-1}) and the power density (P, W kg^{-1}) as follows:

$$E = \frac{1}{8} C \left(\frac{F}{g}\right) \Delta V^2 (mvolt^2) \frac{1000\ g}{1\ kg} \frac{1\ h}{3600\ s} \qquad (3.7)$$

$$P = \frac{E\left(\frac{Wh}{kg}\right) v\left(\frac{mvolt}{s}\right) \frac{3600\ s}{1\ h} \frac{1\ volt}{1000\ mvolt}}{\Delta V\ (volt)} \qquad (3.8)$$

3.10. Results and discussion

3.10.1. Physical and chemical properties

The schematic illustration of the synthesis steps is shown in Figure 3-5. N-doped carbons were prepared from lignin via a two-step process. First, bio-char was synthesized from lignin by using *in-situ* ultra-sonication hydrothermal carbonization (HTC), then, as-prepared bio-char was converted into an N-doped material by an annealing treatment in selected temperature. In this process, lignin and adenine were consumed as carbon and nitrogen sources, respectively and KOH was used as a surface activation agent. The produced N-doped porous carbon samples were labeled as NC-*x*, where *N* denotes the nitrogen doping, C represents porous carbon and *x* reflects the annealing temperature in ^{o}C. For comparison, a pristine porous carbon C-850 sample was processed in the same manner but without the use of a nitrogen source.

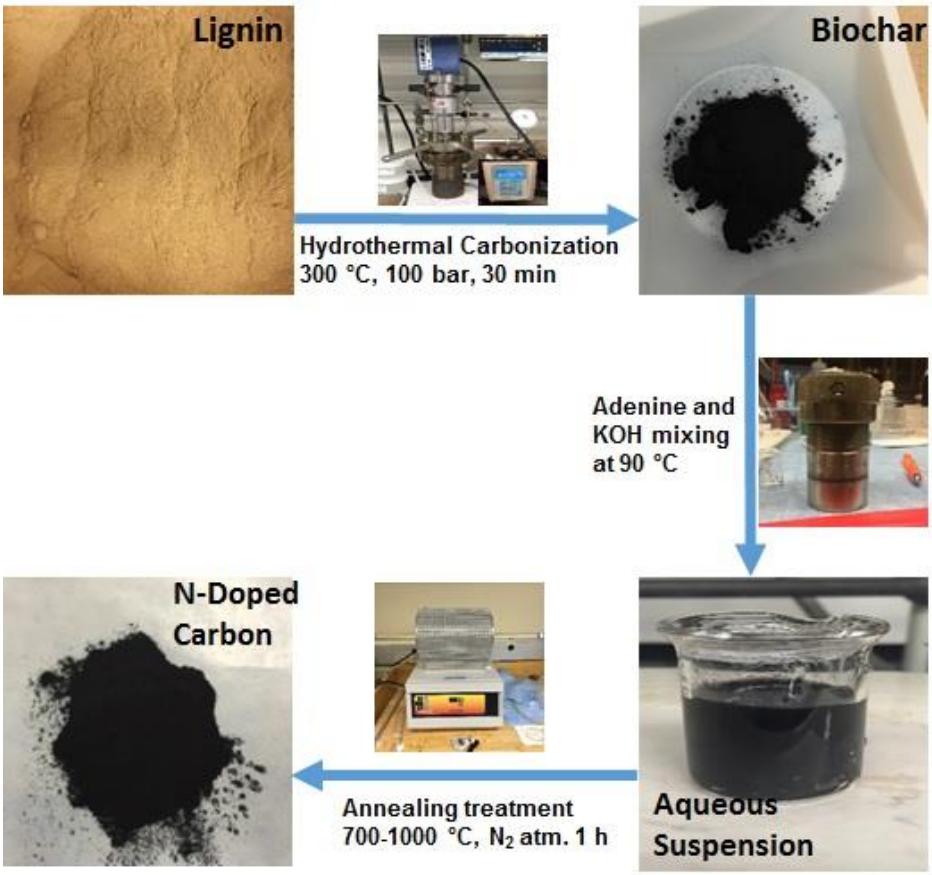

Figure 3-5 N-doped carbon synthesis scheme.

The thermogravimetric analysis of lignin, adenine, and biochar are shown in Figure 3-6(a). The weight loss up to 150 °C was attributed to adsorb water molecules while decomposition of lignin started at 200 °C and continued till 700 °C . The TGA analysis also shows that the residual mass of the biochar and lignin was found to be 64.1 and 16.3 wt.%, respectively. The high conversion yield indicates that lignin can be used as a sustainable carbon source. FTIR spectra of bio-char, C-850, NC-850, as well as lignin, are shown in Figure 3-6(b). Vibrational bands correspond to –OH (3418 cm^{-1}), methoxyl –CH_3O (2843 cm^{-1}), aliphatic –CH (3000–2861 cm^{-1}),

aromatic CH (3064 cm^{-1}), and aromatic rings (1512 and 1597 cm^{-1}) were identified in the IR spectrum of lignin. The IR peaks between 1513 and 1597 cm^{-1} (aromatic ring vibrations) and 1470 and 1460 cm^{-1} (CH deformation) are characteristic peaks for lignin.[65] It is clear that most of the vibrations of the oxygen functional groups such as –OH, $–OCH_3$ which are present in lignin and biochar disappeared after the annealing treatment. However, the peaks located at 1090 C-N (bending)[66] and 1620 cm^{-1} C=O are still visible in IR spectrum of the annealed material which confirms the presence of nitrogen/oxygen functional groups. N-doped carbons were also characterized by Raman spectroscopy. The D-band located at 1346 cm^{-1} corresponds to amorphous sp^3 hybridized carbon while the G-band at 1587 cm^{-1} refers to the presence of a well-ordered graphite structure as depicted in Figure 3-6(c). The intensity ratio of the D band to the G band ($R= I_D/I_G$) can be used to predict the ratio of the amorphous carbon to well-ordered graphite carbon in the resulting materials. The closer the R value of the unit, higher the amorphous carbon content in the material. In the present study, the intensity ratio $R= I_D/I_G$ was found to be 0.99, 0.98, 0.96 and 0.94 for NC-700, NC-850, NC-1000, and GC850, respectively. These results indicated that amorphous carbon content decreased with the increase in annealing temperature. The presence of both graphitic and amorphous carbons in materials are advantageous because it is presumed that specific capacitance of the materials increases with the high amorphous carbon content due to the high active surface while the poor electrical conductivity of the amorphous carbon can be compensated by the high electrical conductivity of graphitic carbon sheets.[67,68] Thus, the composition of the resulting materials was optimized by the combining the amorphous carbon and graphite sheet structure to get the best capacitive performance.

N_2 isotherms at 77 ˚K carried out for carbon samples revealed the mesoporous nature of the N-doped porous carbons where the combination of type-I/IV isotherms were obtained as shown

in Figure 2(d). The textural properties including surface area, pore volume and pore sizes of samples were summarized in Table 1.The Brunauer-Emmett-Teller surface areas (SA_{BET}) were found to be 1788, 2957, 1075 and 2396 m^2 g^{-1} for NC-700, NC-850, NC-1000 and GC850, respectively. Micro and total (in parenthesis) pore volumes were calculated to be 0.49 (0.91), 0.56 (1.79), 0.21 (0.75) and 0.73 (1.24) cm^3 g^{-1}, respectively. The pore size distribution of carbons indicates the presence of micro- and meso- porosity, Figure 3-6 (d)). The pore size in the NC-850 sample is ranging from 0.85 to 3.18 nm. It is noted that surface area, pore size, micro and total pore volume of the materials strongly depend on the annealing temperature. This resulted in the highest surface area along with the largest mesopore structure synthesized at 850 °C annealing temperature. At relatively low temperature, 700 °C, the formation of micro/meso porosity could not develop due to inadequate the KOH etching of carbon. [69] When annealing temperature rises from 850 to 1000 °C, surface area and porosity properties decreased significantly due to the collapsing of micro/meso porosity through the annealing process [70] It is worth noting that the surface area and micro/meso volume of NC-850 are approximately 23 % higher than C-850 (pristine). This is likely due to the fact that nitrogen molecules open extra nano pore structure while they discharge from carbon framework.[35] In addition, XPS results indicate that tangible amount of oxygen-functional groups are presented in the bio-char and N-doped material. While these oxygen-functional groups discharge from carbon structure at relatively higher temperature, they also contribute to the formation of mesoporous with in the structure.[71, 72, 73]

Potassium hydroxide was used as a surface activating agent. The typical mechanism of KOH activating (etching) on carbon based material was reported previously,[74]

$$= CH_2 + 4KOH \leftrightarrow K_2CO_3 + K_2O \ldots (3.1)$$

$$2C + 6KOH \leftrightarrow 2K + 3H_2 + 2K_2CO_3 \ldots (3.2)$$

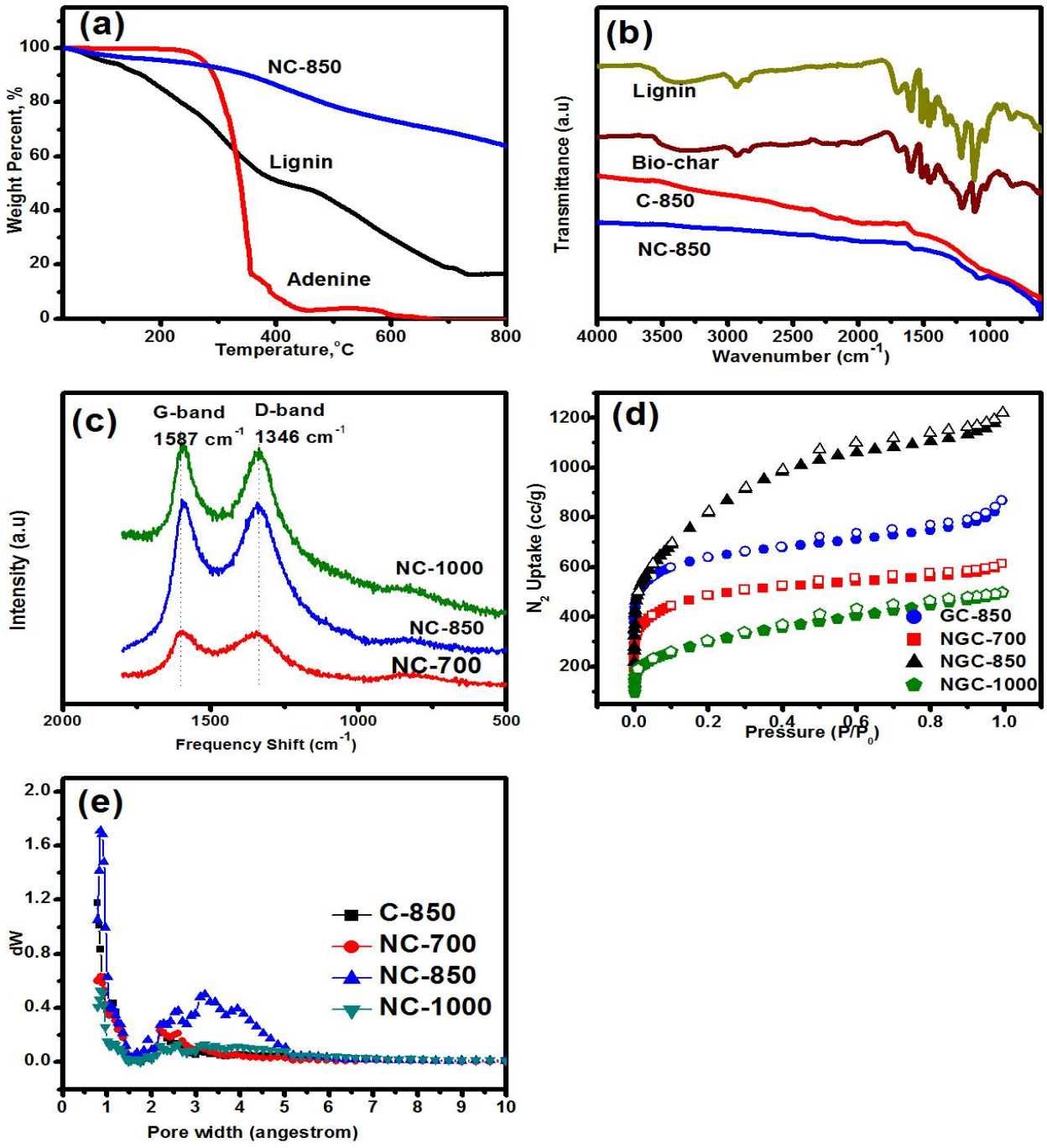

Figure 3-6 (a) TGA curves of lignin, adenine and bio-char (b) FTIR spectra of lignin, bio-char, C-850 and NC-850 (c) Raman spectra of N-doped carbons, (d) Nitrogen uptake at 77 K (e) the pore size distributions calculated from carbon model using adsorption branch fitted with QSDFT

The scanning electron microscope (SEM) micrographs of bio-char, NC-700, NC-850, NC-1000, and C-850 are shown in Figure 3(a- f). Regardless of annealing temperature, the surface topography of obtained materials exhibits sheet-like structures. The sheets, diameter ranging from 2 to 10 µm, are shed by bulky structures which consist of irregular polygons shapes. The macroscopic pore structure caused by KOH etching can be seen on high magnification image of NC-850 in Figure 3-7 (b,c,d).

Table 3-1 Specific capacitance, surface properties, N/C and ID/IG ratio of the obtained materials.

Sample	Capacitance (F/g) [a]	I_D/I_G	N/C ratio	BET surface area (m^2/g) [b]	PSD (nm) [c]	Pore Volume	
						Micro ($cm^3\ g^{-1}$) [d]	Total ($cm^3\ g^{-1}$) [e]
NC-700	240	0.99	0.12	1788	0.84-2.19	0.49 (54)	0.91
NC-850	440	0.98	0.07	2957	0.85-3.18	0.56 (31)	1.79
NC-1000	132	0.97	0.04	1075	0.84-3.20	0.21 (28)	0.75
C-850	375	0.94	-	2396	1.22	0.73 (59)	1.24

a Calculated at 1 m V-1 scan rate b Calculated in the partial pressure range which gives the best linear fitting. cPore size distribution maxima calculated using N2 isotherm at 77 K on carbon model (slit/cylinder. pores, QSDFT adsorption branch). d Determined by cumulative pore volume at 2 nm maxima of the PSD assuming slit/cylindrical shaped pores and QSDFT model; the values in parentheses are the percentage of micropores volume relative to total pore volume. eTotal pore volume at P/Po = 0.95.

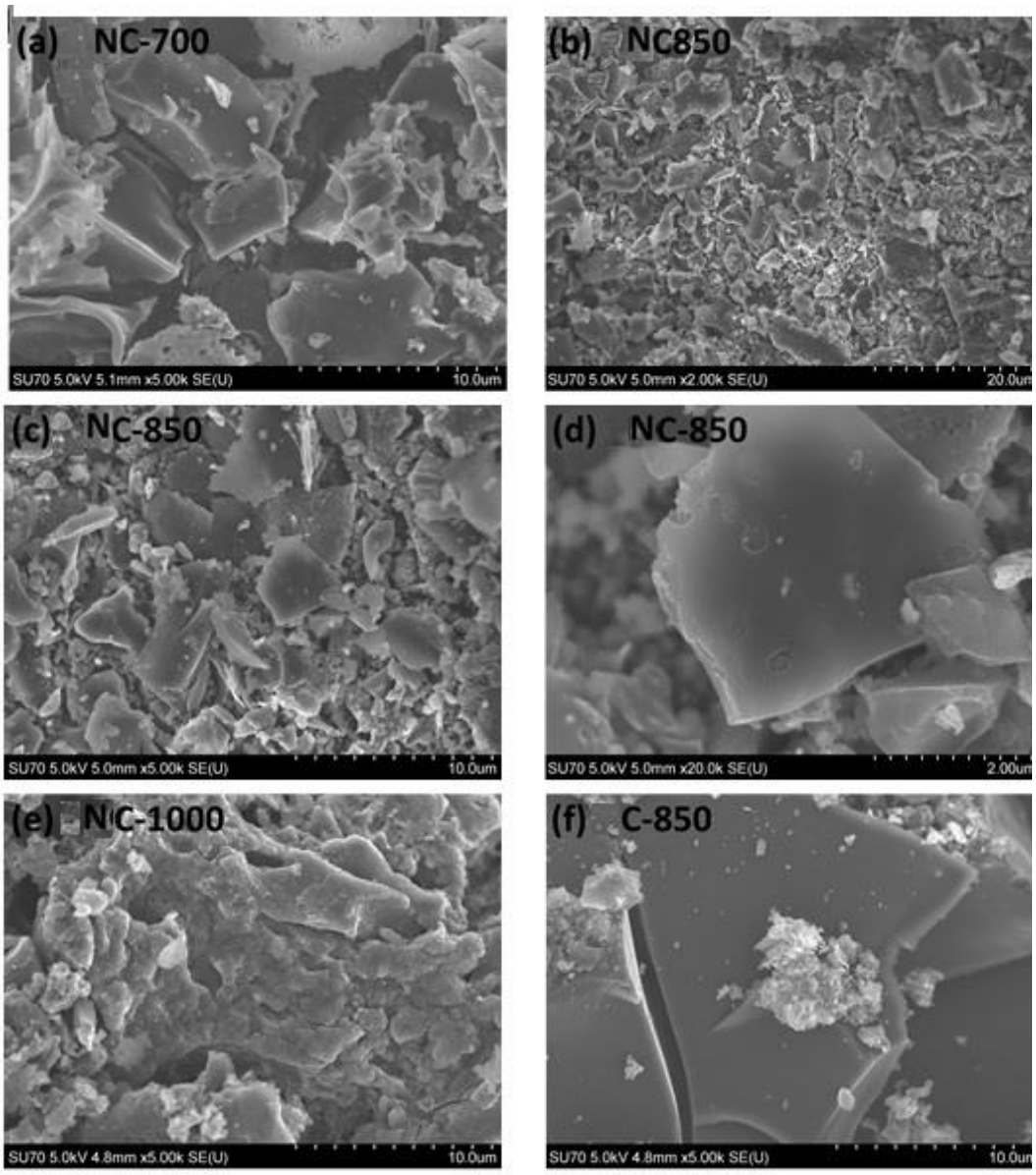

Figure 3-7: SEM image of (a) NC-700, (b), (c), (d) NC-850 at variable magnification (e) NGC100 and (f) C-850

3.10.2. Surface chemical composition by XPS

The surface chemical composition of the materials was investigated by XPS. The survey scan of the as-prepared materials is presented in Figure 3-10(a) and the elemental composition of resulting materials is summarized in Table 2. The carbon content of the prepared N-doped materials was found to be 40.4, 59.5, 64 and 50.4 for NC-700, NC-850, NC-1000 and GC850, respectively. The carbon content increases at higher annealing temperature due to deoxygenation or discharging of volatility molecules (nitrogen). As expected, the nitrogen content of the obtained materials decreased by higher annealing temperature and found to be 5.6, 2.5 and 2.4 % wt. for NC-700, NC-850 and NC-1000, respectively. These results also reflect the successful nitrogen-doping of bio-char by introducing adenine as a nitrogen source. A small amount of nitrogen presented in C-850 may come from reacting of N_2 with biochar through the annealing treatment or naturally existing of nitrogen in lignin. Although it is not seen in survey plot because of the small intensity of peaks, a trace amount of Ca, F were detected from the samples which exist from lignin production process.

The high-resolution deconvolution of C sp2 is presented in Figure 4(b) with the main peak located at 284.8 eV was assigned to C=C bonding. The other smaller fitted peaks placed at 286.3 and 288.9.6 eV were corresponding to C=O/CH_x/C=N and C-C=O bonding, respectively.[75],[76] XPS core-level scan of the O *1s* is presented in Figure 3-10(c), where three types of oxygen functional groups were identified from the spectrum. The main peak located at 531.2 eV refers to the C=O bond while the small peaks at 531.5 and 532.9 eV correspond to O-CO/C-OH (O-I and O-II) bonds.[77]. The high resolution deconvoluted of N1s spectrum of materials was analyzed to investigate the nature of the N atoms/functionality in the prepared N-doped materials. Three types of nitrogen functionalities were assigned in the N-doped materials which are pyridinic-(N-6)

(398.4 eV), pyrrolic-(N-5) (400.1 eV) and oxidized-(N-X) (402.5 eV)[72,78] exhibited in Figure 3-8. Among the three functional nitrogen groups, a combination of pyrrolic and pyridinic functional groups was found to be more active regarding enhancing the capacitance value.

Table 3-2. Elemental and surface composition of N-doped materials,

Sample	C (wt. %)	N (wt. %)	O (wt. %)	Pyridinic (at. %) 398.4 eV	Pyrrolic (at. %) 400.1 eV	Oxidized (at. %) 402.5 eV
NC-700	40.4	5.6	54	16.4	71.5	11.8
NC-850	59.5	2.5	38	34.8	50.8	14.1
NC-1000	64	2.2	33.8	27.5	50.7	21.7
C-850	82.5	0.62	11.9	-	-	-

Elemental analysis was run by XPS

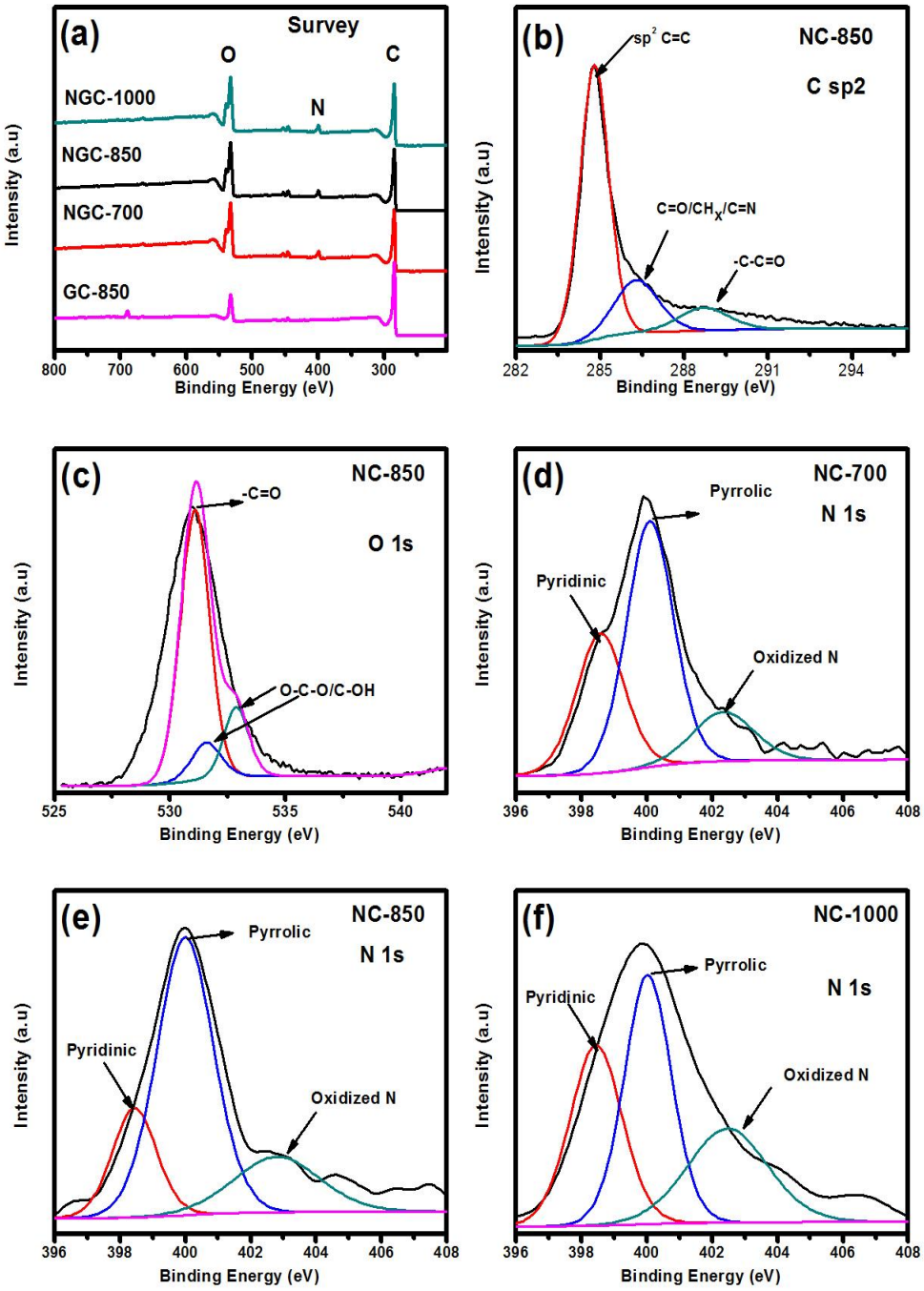

Figure 3-10: XPS analysis of obtained materials (a) survey spectra C-850, NC-700, NC-850 and NC-1000 (b) C1s core level analysis of NC-850 (c) High resolution O 1s core level analysis of NC-850 (d) N1s core level analysis of NC-700 (e) N1s core level analysis

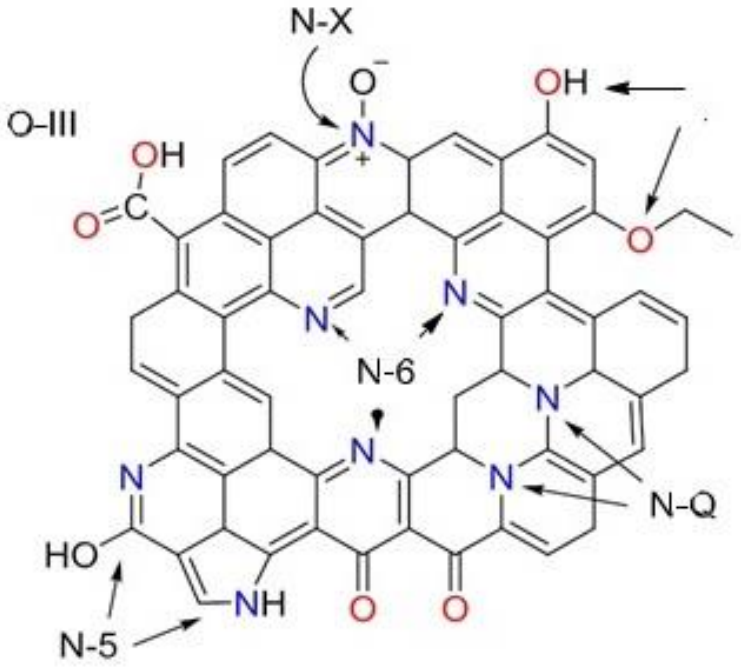

Figure 3-8 Schematic illustration of nitrogen and oxygen functionalities on obtained carbon materials. Adopted and modified from Babak et al. DOI:10.1039/C6TA06251B

3.10.3. Electrochemical performance

The electrochemical characteristics of N-doped carbons have been evaluated for energy storage applications via cyclic voltammetry (CV) and galvanostatic charge-discharge (CD) measurements. The electrochemical behavior of a commercial carbon black sample was also tested as a control experiment. The capacitance value was found to be 14 F/g at 1 A/g for carbon black from the discharge curve. The CV curve of materials is presented in Figures 3-9 (a). At slow scan rates (1 to 20 mV s^{-1}), all the prepared carbon materials displayed rectangular-like cyclic voltammograms, indicating a nearly perfect capacitive performance. The CV profiles, in general, demonstrated a pseudocapacitive behavior at slow sweep rates within -0.7 to -0.4 V regime as shown in Figure 3-9 (c), an evidence that the origin of the as-prepared N-doped carbons capacitive

response is a combination of an electric double-layer capacitance (EDLC) and pseudocapacitance. The appearance of a pseudocapacitance peak in the CV profiles could be attributed to surface functionalities, the presence of nitrogen functional groups and the enhanced surface wettability. [58b],[79], The relation between the annealing temperature and the gravimetric specific capacitance (C_s) is depicted in Figure 3-9 (b). The specific capacitance of NC-700, NC-850 and NC-1000 were measured as 195, 372 and 119 at 10 mV s^{-1} scan rate, respectively. The measured specific capacitance depicts up to +/- 5 % error. This error can also be introduced by the electrode preparation method, amount of active material on the electrode surface. The C_s of the as-prepared N-doped carbons increased by approximately 90 % when the annealing temperature increased from 700 to 850 °C. This increase in the C_s magnitude could be attributed to the significant enhancement in the surface area for the NC-850 sample, almost double that of NC-700 sample, and the obvious increase in pores size which could facilitate the mass transport through the porous framework and so enlarge the ion-accessible surface area and the number of electroactive sites.[26,80,81] C_s decreased significantly when the annealing temperature increased from 850 to 1000 °C, which may be due to a significant decreased in surface area, pore volume, N/C ratio and amorphous carbon content at 1000 °C . In summary, we found that the pseudocapacitive behavior is more pronounced in the NC-850 sample which has a high surface area, micro/meso pore volume, appropriate N/C ratio, and proper amorphous/graphite carbon ratio (I_D/I_G). The volumetric capacitance of NC-850 was found to be 193, 173, and 163 F/cm^3 at 1, 5, 20 mV s^{-1} scan rates, respectively. As compared to the pristine C-850 (314 F g^{-1} at 10 mV s^{-1}), the specific capacitances of NC-850 were enhanced by 17 and 18 % at 1 and 10 mV s^{-1} scan rates, respectively. The observed high C_s value in the NC-850 with respected to pristine C-850 could be attributed to the induced pseudocapacitance, enhanced surface wettability and improved electronic conductivity, resulted in

a better charge distribution and storage within the exposed electrode surface.[82],[83] Another factor that may contribute to the observed enhancement in the C_s is the higher surface area and larger pores size in the NC-850 sample respect to the C-850 sample. The C_s enhancement further supports the claim that N-doping enhances the capacitive response by combining the pseudocapacitance to the EDLC.[84],[85], [86] It is worthwhile to note that C_s value of C-850 was found to be higher than NC-700 or NC-1000, due to the higher surface area and pore volume of C-850. The following typical reaction may take place during the faradic reactions in nitrogen-containing functional groups, [87]

$$-CH - NH_2 + 2OH^- \leftrightarrow -C = NH + H_2O + 2e^- \dots (3.3)$$

$$-C - NH_2 + 2OH^- + 2H^+ \leftrightarrow -C - NHOH + H_2O + 2e^- \dots (3.4)$$

Previous work on the effect of nitrogen functionalities on pseudocapacitance previously [87] has shown that pyridinic and pyrrolic nitrogen-containing functional groups can pronounce the faradaic reaction. This is consistent with our data as NC-850 has 34.8 and 50.8 at. % pyridinic and pyrrolic functional groups, respectively in its structure.

The CV curves deviated from the rectangular shape at high scan rates (> 50 mV s^{-1}) in Figure 3-9(c). This deviation may be due to the poor penetration/ distribution of the applied potential through the material pores, the inherent resistance of the electrode material, KOH electrolyte diffusion resistance, and the contact resistance between the Ni foam current collector and the active electrode material. Another factor that may contribute to the observed deviation in the CV is that the top and the bottom of pores in the electrode materials are subjected to different Ohmic resistances from the KOH aqueous electrolyte.[82]

The effect of N-doping in enhancing the capacitive performance of the prepared samples is further supported by the power density and energy density data, where the N-doped sample displayed higher power and energy densities than the pristine sample. The NC-850 showed an

energy density of 15.3 Wh kg^{-1} and power density of 55.1 W kg^{-1} at a scan rate of 1 mV s^{-1}, as compared to 13.1 Wh kg^{-1} and 46.7 W kg^{-1}, respectively, for C-850.

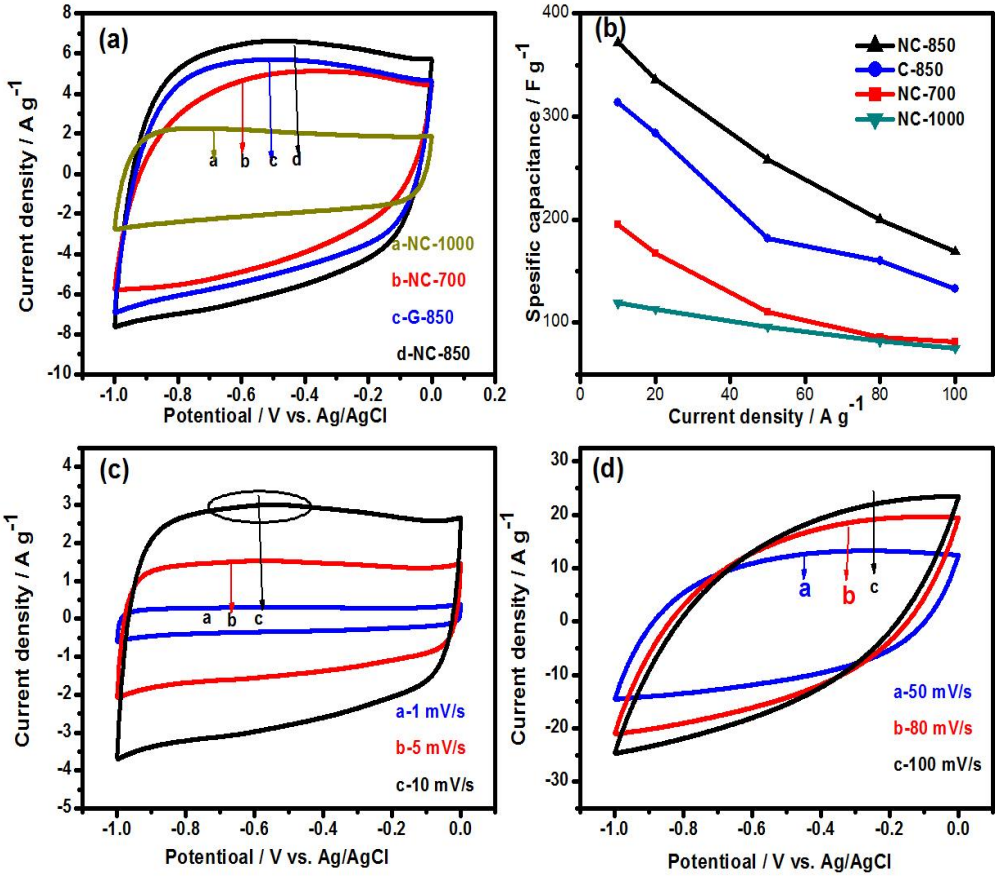

Figure 3-9: (a) CV curves of NC-700, NC-850, NC-1000 and C-850 at 20 mV s-1 scan rate (b) specific capacitance of NC-700, NC-850, NC-1000 and C-850 different scan rates (c) CV curves of NC-850 at different scan rate from 1 to 10 mV s-1 (d) CV curves of NC-850

The charge-discharge behavior of the as-prepared N-doped carbons, NC-700, NC-850, NC-1000 and C-850 samples at 1 A g^{-1} in the potential window of -1 to 0 V is shown in Figure 3-10(a). Also, the charge-discharge curves for NC-850 at different current densities in the potential window of -1 to 0 V are shown in Figure 3-10(b, c). Although the IR drop was obviously seen at relatively higher current densities, the anodic charging and cathodic discharging segments in NC-850 still formed symmetric triangles suggesting a fast dynamics charge-discharge process and good capacitive characteristics. The longest discharging time recorded for NC-850 sample is an indication of a superior capacitive performance, Figure 3-10 (a). The specific capacitance values were found to be 274, 348, 110 and 296 F/g for NC-700, NC-850, NC-1000 and C-850 at 1 A g^{-1} current density, respectively. The high surface area coupled with the relatively high nitrogen/carbon ratio and proper amorphous/graphitic carbon composition could account for the observed enhancement in the discharging time for the NC-850 sample. At the different current densities, the specific capacitance values of NC-850 sample were found to be 324, 305, 282 and 230 at 2, 5, 10 and 20 A g^{-1}, respectively, Figure 3-10 (b, c, d).

Table 3-3 Comparison of the gravimetric capacitances of various carbon materials derived from biomass

Material	Activation method	SSA ($m^2\ g^{-1}$)	Capacitance ($F\ g^{-1}$)	Electrolyte	Measure condition	Ref.
CESM	KOH	221	297	1 M KOH	0.2 A/g	88
bNi(OH)$_2$	Graphene grow	-	1276	1 M KOH	5 mV s^{-1}	89

Corn grains	KOH	2936~3420	206~257	6 M KOH	1mAcm^{-2}	90
Fungi	hydrothermal	80	196	6 M KOH	0.17A g^{-1}	50
Fish scale	KOH	2273	168	7 M KOH	0.05 Ag^{-1}	91
Seaweeds	thermal	15~1307	119~264	1 M H_2SO_4	0.2 A g^{-1}	92
Walnut shell	KOH	2044~2390	168~203	3 M H_2SO_4	1 mA	93
Tea-leaves	KOH	2245~2841	275~330	2 M KOH	1 A g^{-1}	94
Waste paper	KOH	416	180	6 M KOH	2 mV s^{-1}	95
Banana peel	hydrothermal	1650	206	6 M KOH	1 A g^{-1}	96
Sunflower seed shell	KOH	619~2585	213~311	30% KOH	0.25 Ag^{-1}	97
Wheat straw	KOH	2316	251	$MeEt_3NBF_4$/AN	2 mV s^{-1}	98
Silk protein	KOH	2557	264 168	1 M H_2SO_4 BMIM BF_4/AN	0.1 A g^{-1} 0.8 A g^{-1}	99

Pollen	hydrothermal and KOH	3037	185 207	$TEABF_4$/AN EMIM BF_4	1 A g^{-1}	100
Rice husk	CO_2	1500	76	$TEABF_4$/PC	0.05 Ag^{-1}	101
Animal bone	KOH	2157	185	7 M KOH	0.05 Ag^{-1}	102
Cherry stone	KOH	1171	232 120	2 M H_2SO_4 $TEABF_4$/AN	1mAcm^{-2}	103
Fir wood	KOH Steam	1064 1016	180 110	0.5 M H_2SO_4	10 mVs^{-1}	104
Coconut shell	$ZnCl_2$	1874	268 196	6 M KOH $TEABF_4$/PC	1 A g^{-1}	105
Lignin(1)	KOH	3775	286.7	6 M KOH	0.2 A g^{-1}	58c
Lignin(1)	KOH	2265	336	6 M KOH	1 A g^{-1}	58a
Lignin	Composite	802	880	6 M KOH	10 mV s^{-1}	58d
This work (Lignin)	KOH	1104	348	1 M KOH	1 Ag^{-1}	

According to literature and to the best of our knowledge, the NC-850 sample (348 F/g at 1 A/g and 440 F/g at 1 mV s^{-1}) demonstrates the second highest specific capacitance value among the different lignin-derived carbon materials and also show higher or comparable capacitance value to other type of materials shown in Table 3.3.

To examine the interfacial characteristics and the electrochemical response of the as-prepared electrodes, electrochemical impedance spectroscopy (EIS) data were recorded in the frequency range from 10 MHz to 500 kHz with a 5 mV AC amplitude. Three different types of resistance could be distinguished in the Nyquist plot of the studied materials based on the frequency (Figure 3-10 (e)). At the high-frequency region, all the studied materials displayed a semicircular part, its diameter corresponds to the charge transfer resistance (R_{ct}) which control the interfacial electron transfer kinetics at the electrode surface. Although all the studied material displayed similar equivalent series resistant (ESR) of 5.8 □ obtained from the intercept of the Nyquist plot with Z'-real axis at the high-frequency region, the C-850 (Figure 3-10 (e)) displayed a semicircle with a larger diameter due to a higher R_{ct} than NC-850. The R_{ct} of the C-850 and NC-850, calculated from the diameter of the semicircular part in Nyquist plot, were 1.3 and 0.93, respectively. The observed decrease in the charge transfer resistance could be attributed to the N-doping effect. At low-frequency region, the N-doped materials displayed a more vertical line than the C-850 sample indicating a better capacitive performance, faster ion diffusion and low resistance (Warburg resistance) of the ions diffusion to the electrode surface. The impedance data indicated the importance of the N-doping process in enhancing the conductivity and capacitance characteristics of the studied carbon materials.

An important characteristic of any electrochemical supercapacitor is its cycle life. The stability of the as-prepared N-doped carbon electrode (NC-850) was investigated by collecting

charge-discharge over 30,000 cycles at a current density of 20 A g^{-1} within the potential window of -1 to 0 volts. As shown in Figure 3-13 (f), the NC-850 supercapacitor electrode displayed an outstanding cyclic stability under relatively harsh conditions. The ability of the N-C-850 electrode to maintain ~100% capacitive performance up to 10,000 cycles reflects an excellent long-term stability of the electrode material and proved the efficient attachment/incorporation of the nitrogen atoms into the porous carbon framework. Although, the capacitance performance of NC-850 sample was slightly dropped to 95% of its initial value between the 10,000 and 20,000 cycles, then (capacitive performance) enhanced again to ~100% between 20,000 to 30,000 cycles. The observed enhancement in the specific capacitance value at higher cycle numbers may be due to the opening of the pore clogging where more electrolyte ions can enter porous of materials.[106]

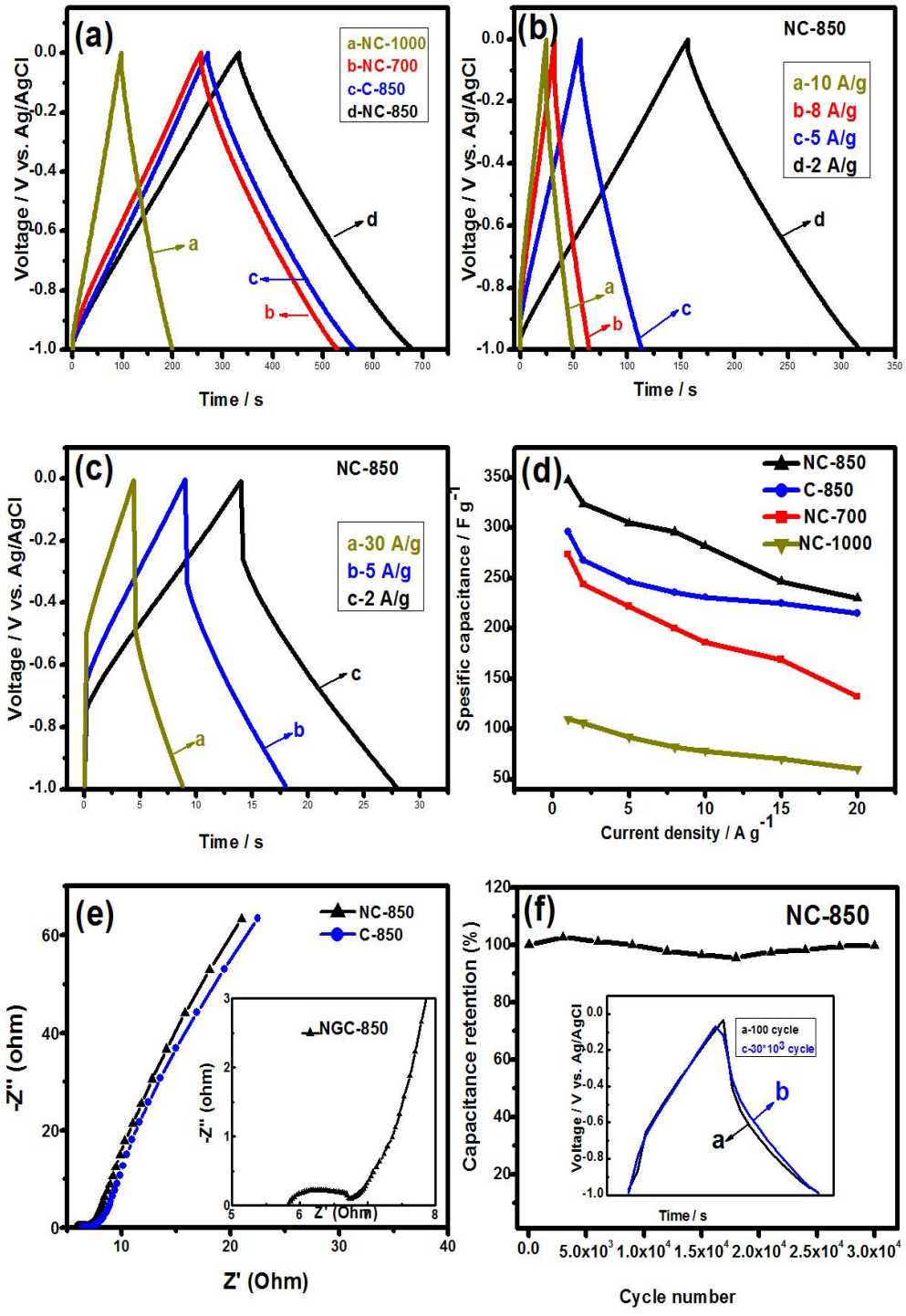

Figure 3-10: (a) Charge-discharge curves of NC-700, NC-850, NC-1000 and C-850 at 1 A g-1 (b) Charge-discharge curves of NC-850 at from 2 to 10 A g-1 (c) Charge-discharge curves of NC-850 at from 15 to 30 A g-1. (d) Specific capacitance of NC-700, NC-850, NC-

3.11. Conclusions

This work reported a new method for the production of N-doped carbons as for supercapacitor applications from lignin. The obtained N-doped materials exhibit high surface area with abundant micro/meso porosity and sheet-like morphology. The best material NC-850 exhibited the high specific capacitance (348 F/g at 1 A/g, and 440 F/g at 1 mV s^{-1}) in the electrolyte solution, due to co-existence of a double layer capacitance and pseudocapacitance phenomena. The NC-850 delivers a maximum energy density of 15.3 Wh kg^{-1} and power density of 55.1 W $kg^{-1,}$ at 1 mV s^{-1}. In addition, the NC-850 exhibited good capacitance retention over 30,000 cycles.

3.12. References

1. Conway, B. E., *Electrochemical supercapacitors: scientific fundamentals and technological applications*. Springer Science & Business Media: 2013.
2. Reddy, A. L. M.; Gowda, S. R.; Shaijumon, M. M.; Ajayan, P. M., Hybrid nanostructures for energy storage applications. *Adv Mater* **2012,** *24* (37), 5045-5064.
3. Zhu, Y.; Murali, S.; Stoller, M. D.; Ganesh, K.; Cai, W.; Ferreira, P. J.; Pirkle, A.; Wallace, R. M.; Cychosz, K. A.; Thommes, M., Carbon-based supercapacitors produced by activation of graphene. *Science* **2011,** *332* (6037), 1537-1541.
4. Sun, L.; Tian, C. G.; Li, M. T.; Meng, X. Y.; Wang, L.; Wang, R. H.; Yin, J.; Fu, H. G., From coconut shell to porous graphene-like nanosheets for high-power supercapacitors. *J Mater Chem A* **2013,** *1* (21), 6462-6470.
5. Zhai, Y. P.; Dou, Y. Q.; Zhao, D. Y.; Fulvio, P. F.; Mayes, R. T.; Dai, S., Carbon Materials for Chemical Capacitive Energy Storage. *Adv Mater* **2011,** *23* (42), 4828-4850.
6. Simon, P.; Gogotsi, Y., Materials for electrochemical capacitors. *Nature materials* **2008,** *7* (11), 845-854.
7. Chen, S.; Bi, J.; Zhao, Y.; Yang, L.; Zhang, C.; Ma, Y.; Wu, Q.; Wang, X.; Hu, Z., Nitrogen-Doped Carbon Nanocages as Efficient Metal-Free Electrocatalysts for Oxygen Reduction Reaction. *Adv Mater* **2012,** *24* (41), 5593-5597.
8. Kim, H.; Fortunato, M. E.; Xu, H.; Bang, J. H.; Suslick, K. S., Carbon Microspheres as Supercapacitors. *The Journal of Physical Chemistry C* **2011,** *115* (42), 20481-20486.
9. Lei, Z.; Lu, L.; Zhao, X., The electrocapacitive properties of graphene oxide reduced by urea. *Energ Environ Sci* **2012,** *5* (4), 6391-6399.
10. Lai, L. F.; Yang, H. P.; Wang, L.; Teh, B. K.; Zhong, J. Q.; Chou, H.; Chen, L. W.; Chen, W.; Shen, Z. X.; Ruoff, R. S.; Lin, J. Y., Preparation of Supercapacitor Electrodes through Selection of Graphene Surface Functionalities. *Acs Nano* **2012,** *6* (7), 5941-5951.
11. Bose, S.; Kuila, T.; Mishra, A. K.; Rajasekar, R.; Kim, N. H.; Lee, J. H., Carbon-based nanostructured materials and their composites as supercapacitor electrodes. *J Mater Chem* **2012,** *22* (3), 767-784.

12. Zhang, L. L.; Zhao, X. S., Carbon-based materials as supercapacitor electrodes. *Chem Soc Rev* **2009,** *38* (9), 2520-2531.
13. Wu, N.-L., Nanocrystalline oxide supercapacitors. *Mater Chem Phys* **2002,** *75* (1–3), 6-11.
14. Ryu, K. S.; Kim, K. M.; Park, N.-G.; Park, Y. J.; Chang, S. H., Symmetric redox supercapacitor with conducting polyaniline electrodes. *J Power Sources* **2002,** *103* (2), 305-309.
15. Alhabeb, M.; Beidaghi, M.; Van Aken, K. L.; Dyatkin, B.; Gogotsi, Y., High-density freestanding graphene/carbide-derived carbon film electrodes for electrochemical capacitors. *Carbon* **2017,** *118*, 642-649.
16. Xu, G.; Zheng, C.; Zhang, Q.; Huang, J.; Zhao, M.; Nie, J.; Wang, X.; Wei, F., Binder-free activated carbon/carbon nanotube paper electrodes for use in supercapacitors. *Nano Res* **2011,** *4* (9), 870-881.
17. Torregrossa, D.; Paolone, M., Modelling of current and temperature effects on supercapacitors ageing. Part I: Review of driving phenomenology. *J Energy Storage* **2016,** *5*, 85-94.
18. Liu, L. L.; Niu, Z. Q.; Chen, J., Unconventional supercapacitors from nanocarbon-based electrode materials to device configurations. *Chem Soc Rev* **2016,** *45* (15), 4340-4363.
19. Xie, Q. X.; Bao, R. R.; Zheng, A. R.; Zhang, Y. F.; Wu, S. H.; Xie, C.; Zhao, P., Sustainable Low-Cost Green Electrodes with High Volumetric Capacitance for Aqueous Symmetric Supercapacitors with High Energy Density. *Acs Sustain Chem Eng* **2016,** *4* (3), 1422-1430.
20. Long, C. L.; Jiang, L. L.; Wu, X. L.; Jiang, Y. T.; Yang, D. R.; Wang, C. K.; Wei, T.; Fan, Z. J., Facile synthesis of functionalized porous carbon with three-dimensional interconnected pore structure for high volumetric performance supercapacitors. *Carbon* **2015,** *93*, 412-420.
21. Mao, C. P.; Liu, S. G.; Pang, L.; Sun, Q.; Liu, Y.; Xu, M. W.; Lu, Z. S., Ultrathin MnO2 nanosheets grown on fungal conidium-derived hollow carbon spheres as supercapacitor electrodes. *Rsc Adv* **2016,** *6* (7), 5184-5191.
22. Hu, X.; Xiong, W.; Wang, W.; Qin, S. L.; Cheng, H. Y.; Zeng, Y.; Wang, B.; Zhu, Z. H., Hierarchical Manganese Dioxide/Poly(3,4-ethylenedioxythiophene) Core-Shell Nanoflakes on Ramie-Derived Carbon Fiber for High-Performance Flexible All-Solid-State Supercapacitor. *Acs Sustain Chem Eng* **2016,** *4* (3), 1201-1211.
23. Li, Y. J.; Wang, G. L.; Wei, T.; Fan, Z. J.; Yan, P., Nitrogen and sulfur co-doped porous carbon nanosheets derived from willow catkin for supercapacitors. *Nano Energy* **2016,** *19*, 165-175.
24. Subramanian, N.; Viswanathan, B., Nitrogen- and oxygen-containing activated carbons from sucrose for electrochemical supercapacitor applications. *Rsc Adv* **2015,** *5* (77), 63000-63011.
25. Zhou, H.; Chen, H.; Luo, S.; Lu, G.; Wei, W.; Kuang, Y., The effect of the polyaniline morphology on the performance of polyaniline supercapacitors. *J Solid State Electr* **2005,** *9* (8), 574-580.
26. Ruan, C.; Ai, K.; Lu, L., Biomass-derived carbon materials for high-performance supercapacitor electrodes. *Rsc Adv* **2014,** *4* (58), 30887-30895.
27. Arbizzani, C.; Mastragostino, M.; Soavi, F., New trends in electrochemical supercapacitors. *J Power Sources* **2001,** *100* (1-2), 164-170.
28. Zhang, D. Y.; Hao, Y.; Zheng, L. W.; Ma, Y.; Feng, H. X.; Luo, H. M., Nitrogen and sulfur co-doped ordered mesoporous carbon with enhanced electrochemical capacitance performance. *J Mater Chem A* **2013,** *1* (26), 7584-7591.
29. Dutta, S.; Bhaumik, A.; Wu, K. C.-W., Hierarchically porous carbon derived from polymers and biomass: effect of interconnected pores on energy applications. *Energ Environ Sci* **2014,** *7* (11), 3574-3592.
30. Yun, Y. S.; Im, C.; Park, H. H.; Hwang, I.; Tak, Y.; Jin, H. J., Hierarchically porous carbon nanofibers containing numerous heteroatoms for supercapacitors. *J Power Sources* **2013,** *234*, 285-291.
31. Feng, H. B.; Zheng, M. T.; Dong, H. W.; Xiao, Y.; Hu, H.; Sun, Z. X.; Long, C.; Cai, Y. J.; Zhao, X.; Zhang, H. R.; Lei, B. F.; Liu, Y. L., Three-dimensional honeycomb-like hierarchically structured carbon for high-performance supercapacitors derived from high-ash-content sewage sludge. *J Mater Chem A* **2015,** *3* (29), 15225-15234.

32. Jiang, H.; Lee, P. S.; Li, C. Z., 3D carbon based nanostructures for advanced supercapacitors. *Energ Environ Sci* **2013,** *6* (1), 41-53.
33. Wen, X.; Zhang, D.; Yan, T.; Zhang, J.; Shi, L., Three-dimensional graphene-based hierarchically porous carbon composites prepared by a dual-template strategy for capacitive deionization. *J Mater Chem A* **2013,** *1* (39), 12334-12344.
34. Xie, K.; Qin, X.; Wang, X.; Wang, Y.; Tao, H.; Wu, Q.; Yang, L.; Hu, Z., Carbon nanocages as supercapacitor electrode materials. *Adv Mater* **2012,** *24* (3), 347-352.
35. Ania, C. O.; Khomenko, V.; Raymundo-Piñero, E.; Parra, J. B.; Beguin, F., The large electrochemical capacitance of microporous doped carbon obtained by using a zeolite template. *Adv Funct Mater* **2007,** *17*.
36. Niu, Z.; Zhang, L.; Liu, L.; Zhu, B.; Dong, H.; Chen, X., All-Solid-State Flexible Ultrathin Micro-Supercapacitors Based on Graphene. *Adv Mater* **2013,** *25* (29), 4035-4042.
37. Zhao, Y.; Hu, C.; Hu, Y.; Cheng, H.; Shi, G.; Qu, L., A Versatile, Ultralight, Nitrogen-Doped Graphene Framework. *Angewandte Chemie* **2012,** *124* (45), 11533-11537.
38. Wei, L.; Sevilla, M.; Fuertes, A. B.; Mokaya, R.; Yushin, G., Hydrothermal Carbonization of Abundant Renewable Natural Organic Chemicals for High-Performance Supercapacitor Electrodes. *Adv Energy Mater* **2011,** *1* (3), 356-361.
39. Béguin, F.; Szostak, K.; Lota, G.; Frackowiak, E., A Self-Supporting Electrode for Supercapacitors Prepared by One-Step Pyrolysis of Carbon Nanotube/Polyacrylonitrile Blends. *Adv Mater* **2005,** *17* (19), 2380-2384.
40. Shrestha, S.; Mustain, W. E., Properties of Nitrogen-Functionalized Ordered Mesoporous Carbon Prepared Using Polypyrrole Precursor. *Journal of The Electrochemical Society* **2010,** *157* (11), B1665-B1672.
41. Li, L.; Liu, E.; Li, J.; Yang, Y.; Shen, H.; Huang, Z.; Xiang, X.; Li, W., A doped activated carbon prepared from polyaniline for high performance supercapacitors. *J Power Sources* **2010,** *195* (5), 1516-1521.
42. Zhong, M.; Kim, E. K.; McGann, J. P.; Chun, S.-E.; Whitacre, J. F.; Jaroniec, M.; Matyjaszewski, K.; Kowalewski, T., Electrochemically Active Nitrogen-Enriched Nanocarbons with Well-Defined Morphology Synthesized by Pyrolysis of Self-Assembled Block Copolymer. *Journal of the American Chemical Society* **2012,** *134* (36), 14846-14857.
43. Hulicova, D.; Kodama, M.; Hatori, H., Electrochemical Performance of Nitrogen-Enriched Carbons in Aqueous and Non-Aqueous Supercapacitors. *Chemistry of Materials* **2006,** *18* (9), 2318-2326.
44. Hulicova-Jurcakova, D.; Kodama, M.; Shiraishi, S.; Hatori, H.; Zhu, Z. H.; Lu, G. Q., Nitrogen-Enriched Nonporous Carbon Electrodes with Extraordinary Supercapacitance. *Adv Funct Mater* **2009,** *19* (11), 1800-1809.
45. Hulicova-Jurcakova, D.; Seredych, M.; Lu, G. Q.; Bandosz, T. J., Combined Effect of Nitrogen-and Oxygen-Containing Functional Groups of Microporous Activated Carbon on its Electrochemical Performance in Supercapacitors. *Adv Funct Mater* **2009,** *19* (3), 438-447.
46. Jeong, H. M.; Lee, J. W.; Shin, W. H.; Choi, Y. J.; Shin, H. J.; Kang, J. K.; Choi, J. W., Nitrogen-Doped Graphene for High-Performance Ultracapacitors and the Importance of Nitrogen-Doped Sites at Basal Planes. *Nano Letters* **2011,** *11* (6), 2472-2477.
47. Raymundo-Piñero, E.; Leroux, F.; Béguin, F., A high-performance carbon for supercapacitors obtained by carbonization of a seaweed biopolymer. *Adv Mater* **2006,** *18* (14), 1877-1882.
48. Li, Z.; Zhang, L.; Amirkhiz, B. S.; Tan, X.; Xu, Z.; Wang, H.; Olsen, B. C.; Holt, C.; Mitlin, D., Carbonized Chicken Eggshell Membranes with 3D Architectures as High-Performance Electrode Materials for Supercapacitors. *Adv Energy Mater* **2012,** *2* (4), 431-437.
49. Zhu, H.; Wang, X.; Liu, X.; Yang, X., Integrated Synthesis of Poly (o-phenylenediamine)-Derived Carbon Materials for High Performance Supercapacitors. *Adv Mater* **2012,** *24* (48), 6524-6529.

50. Zhu, H.; Wang, X.; Yang, F.; Yang, X., Promising Carbons for Supercapacitors Derived from Fungi. *Adv Mater* **2011,** *23* (24), 2745-2748.
51. Gosselink, R. J. A.; Abächerli, A.; Semke, H.; Malherbe, R.; Käuper, P.; Nadif, A.; van Dam, J. E. G., Analytical protocols for characterisation of sulphur-free lignin. *Industrial Crops and Products* **2004,** *19* (3), 271-281.
52. Li, C.; Zhao, X.; Wang, A.; Huber, G. W.; Zhang, T., Catalytic Transformation of Lignin for the Production of Chemicals and Fuels. *Chemical Reviews* **2015**.
53. (a) Li, H.; Yuan, D.; Tang, C. H.; Wang, S. X.; Sun, J. T.; Li, Z. B.; Tang, T.; Wang, F. K.; Gong, H.; He, C. B., Lignin-derived interconnected hierarchical porous carbon monolith with large areal/volumetric capacitances for supercapacitor. *Carbon* **2016,** *100*, 151-157; (b) Demir, M.; Kahveci, Z.; Aksoy, B.; Palapati, N. K.; Subramanian, A.; Cullinan, H. T.; El-Kaderi, H. M.; Harris, C. T.; Gupta, R. B., Graphitic bio-carbon from metal-catalyzed hydrothermal carbonization of lignin. *ACS Industrial & Engineering Chemistry Research* **2015**.
54. Wu, Y.; Zhang, S.; Guo, X.; Huang, H., Adsorption of chromium (III) on lignin. *Bioresource technology* **2008,** *99* (16), 7709-7715.
55. Basu, S.; Gaur, R.; Gomes, J.; Sreekrishnan, T.; Bisaria, V. S., Effect of seed culture on solid-state bioconversion of wheat straw by Phanerochaete chrysosporium for animal feed production. *Journal of bioscience and bioengineering* **2002,** *93* (1), 25-30.
56. Saha, D.; Li, Y.; Bi, Z.; Chen, J.; Keum, J. K.; Hensley, D. K.; Grappe, H. A.; Meyer III, H. M.; Dai, S.; Paranthaman, M. P., Studies on supercapacitor electrode material from activated lignin-derived mesoporous carbon. *Langmuir* **2014,** *30* (3), 900-910.
57. Zhang, W.; Lin, H.; Lin, Z.; Yin, J.; Lu, H.; Liu, D.; Zhao, M., 3 D Hierarchical Porous Carbon for Supercapacitors Prepared from Lignin through a Facile Template-Free Method. *Chemsuschem* **2015,** *8* (12), 2114-2122.
58. (a) Wang, K. L.; Cao, Y. H.; Wang, X. M.; Castro, M. A.; Luo, B.; Gu, Z. R.; Liu, J.; Hoefelmeyer, J. D.; Fan, Q. H., Rod-shape porous carbon derived from aniline modified lignin for symmetric supercapacitors. *J Power Sources* **2016,** *307*, 462-467; (b) Zhao, H. B.; Wang, W. D.; Lu, Q. F.; Lin, T. T.; Lin, Q. L.; Yang, H. J., Preparation and application of porous nitrogen-doped graphene obtained by co-pyrolysis of lignosulfonate and graphene oxide. *Bioresource Technology* **2015,** *176*, 106-111; (c) Zhang, W. L.; Zhao, M. Z.; Liu, R. Y.; Wang, X. F.; Lin, H. B., Hierarchical porous carbon derived from lignin for high performance supercapacitor. *Colloid Surface A* **2015,** *484*, 518-527; (d) Hu, S. X.; Zhang, S. L.; Pan, N.; Hsieh, Y. L., High energy density supercapacitors from lignin derived submicron activated carbon fibers in aqueous electrolytes. *J Power Sources* **2014,** *270*, 106-112; (e) Chen, F.; Zhou, W. J.; Yao, H. F.; Fan, P.; Yang, J. T.; Fei, Z. D.; Zhong, M. Q., Self-assembly of NiO nanoparticles in lignin-derived mesoporous carbons for supercapacitor applications. *Green Chem* **2013,** *15* (11), 3057-3063.
59. Jeon, J.-W.; Zhang, L.; Lutkenhaus, J. L.; Laskar, D. D.; Lemmon, J. P.; Choi, D.; Nandasiri, M. I.; Hashmi, A.; Xu, J.; Motkuri, R. K.; Fernandez, C. A.; Liu, J.; Tucker, M. P.; McGrail, P. B.; Yang, B.; Nune, S. K., Controlling Porosity in Lignin-Derived Nanoporous Carbon for Supercapacitor Applications. *Chemsuschem* **2015,** *8* (3), 428-432.
60. Lai, C. L.; Zhou, Z. P.; Zhang, L. F.; Wang, X. X.; Zhou, Q. X.; Zhao, Y.; Wang, Y. C.; Wu, X. F.; Zhu, Z. T.; Fong, H., Free-standing and mechanically flexible mats consisting of electrospun carbon nanofibers made from a natural product of alkali lignin as binder-free electrodes for high-performance supercapacitors. *J Power Sources* **2014,** *247*, 134-141.
61. Jeon, J. W.; Zhang, L. B.; Lutkenhaus, J. L.; Laskar, D. D.; Lemmon, J. P.; Choi, D.; Nandasiri, M. I.; Hashmi, A.; Xu, J.; Motkuri, R. K.; Fernandez, C. A.; Liu, J.; Tucker, M. P.; McGrail, P. B.; Yang, B.; Nune, S. K., Controlling Porosity in Lignin-Derived Nanoporous Carbon for Supercapacitor Applications. *Chemsuschem* **2015,** *8* (3), 428-432.

62. Ramsurn, H.; Kumar, S.; Gupta, R. B., Enhancement of biochar gasification in alkali hydrothermal medium by passivation of inorganic components using Ca (OH) 2. *Energy & Fuels* **2011,** *25* (5), 2389-2398.
63. El-Kady, M. F.; Strong, V.; Dubin, S.; Kaner, R. B., Laser scribing of high-performance and flexible graphene-based electrochemical capacitors. *Science* **2012,** *335* (6074), 1326-1330.
64. Xie, Q.; Bao, R.; Zheng, A.; Zhang, Y.; Wu, S.; Xie, C.; Zhao, P., Sustainable Low-Cost Green Electrodes with High Volumetric Capacitance for Aqueous Symmetric Supercapacitors with High Energy Density. *Acs Sustain Chem Eng* **2016**.
65. Suhas; Carrott, P. J. M.; Ribeiro Carrott, M. M. L., Lignin – from natural adsorbent to activated carbon: A review. *Bioresource Technology* **2007,** *98* (12), 2301-2312.
66. Ma, Y.; Du, Z.; Liu, J.; Xia, F.; Xu, J., Selective oxidative C–C bond cleavage of a lignin model compound in the presence of acetic acid with a vanadium catalyst. *Green Chem* **2015,** *17* (11), 4968-4973.
67. Barranco, V.; Lillo-Rodenas, M. A.; Linares-Solano, A.; Oya, A.; Pico, F.; Ibañez, J.; Agullo-Rueda, F.; Amarilla, J. M.; Rojo, J. M., Amorphous Carbon Nanofibers and Their Activated Carbon Nanofibers as Supercapacitor Electrodes. *The Journal of Physical Chemistry C* **2010,** *114* (22), 10302-10307.
68. Sevilla, M.; Mokaya, R., Energy storage applications of activated carbons: supercapacitors and hydrogen storage. *Energ Environ Sci* **2014,** *7* (4), 1250-1280.
69. Wu, F.-C.; Tseng, R.-L., Preparation of highly porous carbon from fir wood by KOH etching and CO 2 gasification for adsorption of dyes and phenols from water. *J Colloid Interf Sci* **2006,** *294* (1), 21-30.
70. Selvamani, V.; Ravikumar, R.; Suryanarayanan, V.; Velayutham, D.; Gopukumar, S., Fish scale derived nitrogen doped hierarchical porous carbon—a high rate performing anode for lithium ion cell. *Electrochimica Acta* **2015,** *182*, 1-10.
71. Luo, H. X.; Liu, Z. Y.; Chao, L. M.; Wu, X. C.; Lei, X. D.; Chang, Z.; Sun, X. M., Synthesis of hierarchical porous N-doped sandwich-type carbon composites as high-performance supercapacitor electrodes. *J Mater Chem A* **2015,** *3* (7), 3667-3675.
72. Gao, F.; Shao, G. H.; Qu, J. Y.; Lv, S. Y.; Li, Y. Q.; Wu, M. B., Tailoring of porous and nitrogen-rich carbons derived from hydrochar for high-performance supercapacitor electrodes. *Electrochimica Acta* **2015,** *155*, 201-208.
73. Zhao, X.; Zhu, J. B.; Liang, L.; Li, C. Y.; Liu, C. P.; Liao, J. H.; Xing, W., Biomass-derived N-doped carbon and its application in electrocatalysis. *Appl Catal B-Environ* **2014,** *154*, 177-182.
74. Zhang, L.; Liu, Z.; Cui, G.; Chen, L., Biomass-derived materials for electrochemical energy storages. *Progress in Polymer Science* **2015,** *43*, 136-164.
75. Shirazi, S. F. S.; Gharehkhani, S.; Yarmand, H.; Badarudin, A.; Metselaar, H. S. C.; Kazi, S. N., Nitrogen doped activated carbon/graphene with high nitrogen level: green synthesis and thermo-electrical properties of its nanofluid. *Mater Lett* **2015,** *152*, 192-195.
76. Gharehkhani, S.; Shirazi, S. F. S.; Jahromi, S. P.; Sookhakian, M.; Baradaran, S.; Yarmand, H.; Oshkour, A. A.; Kazi, S. N.; Basirun, W. J., Spongy nitrogen-doped activated carbonaceous hybrid derived from biomass material/graphene oxide for supercapacitor electrodes. *Rsc Adv* **2015,** *5* (51), 40505-40513.
77. Ai, Y. L.; Xie, X. H.; He, W.; Liang, B. L.; Fan, Y. Q., Microstructure and properties of Al2O3(n)/ZrO2 dental ceramics prepared by two-step microwave sintering. *Mater Design* **2015,** *65*, 1021-1027.
78. Lee, M.; Kim, G. P.; Song, H. D.; Park, S.; Yi, J., Preparation of energy storage material derived from a used cigarette filter for a supercapacitor electrode. *Nanotechnology* **2014,** *25* (34).
79. Zhao, Y. H.; Liu, M. X.; Deng, X. X.; Miao, L.; Tripathi, P. K.; Ma, X. M.; Zhu, D. Z.; Xu, Z. J.; Hao, Z. X.; Gan, L. H., Nitrogen-functionalized microporous carbon nanoparticles for high performance supercapacitor electrode. *Electrochimica Acta* **2015,** *153*, 448-455.
80. Wang, L.; Gao, Z.; Chang, J.; Liu, X.; Wu, D.; Xu, F.; Guo, Y.; Jiang, K., Nitrogen-Doped Porous Carbons As Electrode Materials for High-Performance Supercapacitor and Dye-Sensitized Solar Cell. *Acs Appl Mater Inter* **2015,** *7* (36), 20234-20244.

81. John, A. R.; Arumugam, P., Open ended nitrogen-doped carbon nanotubes for the electrochemical storage of energy in a supercapacitor electrode. *J Power Sources* **2015,** *277*, 387-392.
82. Ren, Y. M.; Zhang, J. M.; Xu, Q.; Chen, Z. M.; Yang, D. Y.; Wang, B.; Jiang, Z., Biomass-derived three-dimensional porous N-doped carbonaceous aerogel for efficient supercapacitor electrodes. *Rsc Adv* **2014,** *4* (45), 23412-23419.
83. Liu, R. L.; Ji, W. J.; He, T.; Zhang, Z. Q.; Zhang, J.; Dang, F. Q., Fabrication of nitrogen-doped hierarchically porous carbons through a hybrid dual-template route or CO2 capture and haemoperfusion. *Carbon* **2014,** *76*, 84-95.
84. Ruan, C. P.; Ai, K. L.; Lu, L. H., Biomass-derived carbon materials for high-performance supercapacitor electrodes. *Rsc Adv* **2014,** *4* (58), 30887-30895.
85. Ma, G. F.; Yang, Q.; Sun, K. J.; Peng, H.; Ran, F. T.; Zhao, X. L.; Lei, Z. Q., Nitrogen-doped porous carbon derived from biomass waste for high-performance supercapacitor. *Bioresource Technology* **2015,** *197*, 137-142.
86. He, S. J.; Hou, H. Q.; Chen, W., 3D porous and ultralight carbon hybrid nanostructure fabricated from carbon foam covered by monolayer of nitrogen-doped carbon nanotubes for high performance supercapacitors. *J Power Sources* **2015,** *280*, 678-686.
87. Wei, X.; Jiang, X.; Wei, J.; Gao, S., Functional Groups and Pore Size Distribution do Matter to Hierarchically Porous Carbons as High-Rate-Performance Supercapacitors. *Chemistry of Materials* **2015**.
88. Li, Z.; Zhang, L.; Amirkhiz, B. S.; Tan, X. H.; Xu, Z. W.; Wang, H. L.; Olsen, B. C.; Holt, C. M. B.; Mitlin, D., Carbonized Chicken Eggshell Membranes with 3D Architectures as High-Performance Electrode Materials for Supercapacitors. *Adv Energy Mater* **2012,** *2* (4), 431-437.
89. Wang, H. L.; Dai, H. J., Strongly coupled inorganic-nano-carbon hybrid materials for energy storage. *Chem Soc Rev* **2013,** *42* (7), 3088-3113.
90. Balathanigaimani, M.; Shim, W.-G.; Lee, M.-J.; Kim, C.; Lee, J.-W.; Moon, H., Highly porous electrodes from novel corn grains-based activated carbons for electrical double layer capacitors. *Electrochem Commun* **2008,** *10* (6), 868-871.
91. Chen, W.; Zhang, H.; Huang, Y.; Wang, W., A fish scale based hierarchical lamellar porous carbon material obtained using a natural template for high performance electrochemical capacitors. *J Mater Chem* **2010,** *20* (23), 4773-4775.
92. Raymundo-Piñero, E.; Cadek, M.; Béguin, F., Tuning carbon materials for supercapacitors by direct pyrolysis of seaweeds. *Adv Funct Mater* **2009,** *19* (7), 1032-1039.
93. Choi, W.-S.; Shim, W.-G.; Ryu, D.-W.; Hwang, M.-J.; Moon, H., Effect of ball milling on electrochemical characteristics of walnut shell-based carbon electrodes for EDLCs. *Microporous and Mesoporous Materials* **2012,** *155*, 274-280.
94. Peng, C.; Yan, X.-b.; Wang, R.-t.; Lang, J.-w.; Ou, Y.-j.; Xue, Q.-j., Promising activated carbons derived from waste tea-leaves and their application in high performance supercapacitors electrodes. *Electrochimica Acta* **2013,** *87*, 401-408.
95. Kalpana, D.; Cho, S.; Lee, S.; Lee, Y.; Misra, R.; Renganathan, N., Recycled waste paper—A new source of raw material for electric double-layer capacitors. *J Power Sources* **2009,** *190* (2), 587-591.
96. Lv, Y.; Gan, L.; Liu, M.; Xiong, W.; Xu, Z.; Zhu, D.; Wright, D. S., A self-template synthesis of hierarchical porous carbon foams based on banana peel for supercapacitor electrodes. *J Power Sources* **2012,** *209*, 152-157.
97. Li, X.; Xing, W.; Zhuo, S.; Zhou, J.; Li, F.; Qiao, S.-Z.; Lu, G.-Q., Preparation of capacitor's electrode from sunflower seed shell. *Bioresource technology* **2011,** *102* (2), 1118-1123.
98. Li, X.; Han, C.; Chen, X.; Shi, C., Preparation and performance of straw based activated carbon for supercapacitor in non-aqueous electrolytes. *Microporous and Mesoporous Materials* **2010,** *131* (1), 303-309.

99. Yun, Y. S.; Cho, S. Y.; Shim, J.; Kim, B. H.; Chang, S. J.; Baek, S. J.; Huh, Y. S.; Tak, Y.; Park, Y. W.; Park, S., Microporous carbon nanoplates from regenerated silk proteins for supercapacitors. *Adv Mater* **2013,** *25* (14), 1993-1998.
100. Zhang, L.; Zhang, F.; Yang, X.; Leng, K.; Huang, Y.; Chen, Y., High-Performance Supercapacitor Electrode Materials Prepared from Various Pollens. *Small* **2013,** *9* (8), 1342-1347.
101. Kuratani, K.; Okuno, K.; Iwaki, T.; Kato, M.; Takeichi, N.; Miyuki, T.; Awazu, T.; Majima, M.; Sakai, T., Converting rice husk activated carbon into active material for capacitor using three-dimensional porous current collector. *J Power Sources* **2011,** *196* (24), 10788-10790.
102. Huang, W.; Zhang, H.; Huang, Y.; Wang, W.; Wei, S., Hierarchical porous carbon obtained from animal bone and evaluation in electric double-layer capacitors. *Carbon* **2011,** *49* (3), 838-843.
103. Olivares-Marín, M.; Fernández, J.; Lázaro, M. J.; Fernández-González, C.; Macías-García, A.; Gómez-Serrano, V.; Stoeckli, F.; Centeno, T. A., Cherry stones as precursor of activated carbons for supercapacitors. *Mater Chem Phys* **2009,** *114* (1), 323-327.
104. Wu, F.-C.; Tseng, R.-L.; Hu, C.-C.; Wang, C.-C., Effects of pore structure and electrolyte on the capacitive characteristics of steam-and KOH-activated carbons for supercapacitors. *J Power Sources* **2005,** *144* (1), 302-309.
105. Sun, L.; Tian, C.; Li, M.; Meng, X.; Wang, L.; Wang, R.; Yin, J.; Fu, H., From coconut shell to porous graphene-like nanosheets for high-power supercapacitors. *J Mater Chem A* **2013,** *1* (21), 6462-6470.
106. Lee, M.; Kim, G.-P.; Song, H. D.; Park, S.; Yi, J., Preparation of energy storage material derived from a used cigarette filter for a supercapacitor electrode. *Nanotechnology* **2014,** *25* (34), 345601.

4. Chapter 4. Supercapacitive and Oxygen Reduction Characteristics of the Sulfur Self-Doped Micro/Mesoporous Carbon Derived From Lignin

4.1. Fuel cells

Fuel cells are electrochemical devices that convert the chemical energy of fuels into electric energy. Typically, a fuel cell consists of two electrodes (anode and cathode), a separator for proton exchange and two electron collector for electricity flow. When protons and electrons move to the cathode side, oxygen molecules are reduced to form water in hydrogen fuel cell. In the full process, only electricity and water are come out as products which make it an environmentally benign process. Each cell produces around 0.6-0.7 V. To provide a high voltage, individual cells are combined to form a large size fuel cell. The schematic illustration of working principle of the fuel cell is shown in Figure 4-1. There is two design mechanism for reduction of oxygen, which is the main rate limiting reaction. The direct four electron process of O_2 reduction is preferred and desired for optimum energy saving and to avoid hydrogen peroxide formation. The direct two electron process which is the competitive reaction and leads to low cell voltage, overall efficiency losses, and formation of byproduct hydrogen peroxide in fuel cells1,2.

E_0 = + 0.695 vs. NHE (2 electron pathway)

$$O_{2(g)} + [H^+ + e^-] \rightarrow *OOH_{(aq)} \quad (4.1)$$

$$*OOH_{(aq)}[H^+ + e^-] \rightarrow H_2O_2 \quad (4.2(a))$$

$$E_0 = +1.229\ vs.NHE\ (4\ electron\ path\ way)$$

$$O_{2(g)} + [H^+ + e^-] \rightarrow *OOH_{(aq)} \quad 4.3$$

$$* OOH_{(aq)} + [H^+ + e^-] \rightarrow * O_{(aq)} + H_2O_{(aq)} \text{ (4.2(b))}$$

$$* O_{(aq)} + [H^+ + e^-] \rightarrow * OH_{(aq)} + H_2O_{(aq)} \text{ (4.4)}$$

$$* OH_{(aq)} + [H^+ + e^-] \rightarrow * H_2O_{(aq)} \text{ (4.5)}$$

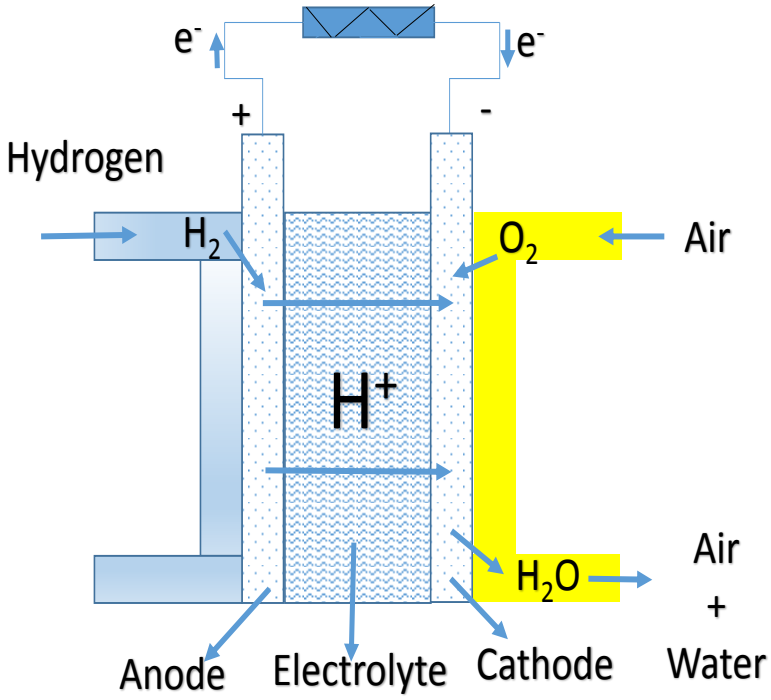

Figure 4-1: The schematic illustration of working principle of fuel cell

4.2. The oxygen reduction reaction (ORR) catalyst

In the last decade, oxygen reduction reaction (ORR) studies have drawn more attention due to their application in fuel cells, water purification, and metal-air batteries.[3,4]. Efficient electrocatalysts materials are important for practical applications of fuel cell because of the high over potential caused by low activity of oxygen reduction reaction [3a]

Recently, the Pt-based catalyst had been known as the best catalyst for ORR due to the excellent oxygen reduction efficiency; however, there are many concerns using Pt-based catalyst including high cost, poor durability, and limited transport of electrolyte on the surface.[5]. Especially, efficiency loss of Pt-based catalyst (in process high potential lead to Pt degradation) and higher cost ($32 per gram (2015)) limit commercializing of fuel cells.[6] Therefore, more efficient, durable, and low-cost fuel cell catalysts are urgently needed for commercializing fuel cells. Ongoing research has developed alternative non-metal materials for ORR application instead of platinum-based catalysts[7]. For instance, Pt-based alloy materials, variable metal oxides, etc. However, these catalysts are still not practically useful because of harsh synthesis conditions, expensive and not durable. In terms of non-metal catalysts, carbon-derived catalysts have been considered as inexpensive, abundant, chemically stable, highly durable and eco-friendly catalysts, however, practical application of these catalysts are still limited toward the ORR due to the poor electrochemical activity, less active site for O_2 reduction and low electrical/ionic conductivity. The chemical doping such as N or B, P, S into carbon framework has been received as an effective method to modify the catalytic properties of carbon materials. [6] Structural defects introduced by heteroatom dopants result in more edge-active sites in the carbon structure which enhances the electrochemical activity toward the ORR. Especially, sulfur-doped carbon could potentially replace Pt-based catalyst in a fuel cell. Although the nature of the active sites of sulfur remains elusive, sulfur has been generally identified as an essential element for catalytic sites in carbon structure because of six valence electrons in sulfur available to form strong covalent bonds with carbon atoms[8], [9]. When O_2 molecules adsorbed on the surface, breaking of O-O bond is one of the most challenge steps for oxygen reduction reaction. Existing of C-S bond opens new active in the edge or defect sites which help to break O-O bonding on the surface. Contrary to N, B, P molecules, it

is believed that spin density is a more leading factor for regulating ORR activity than charge distribution in the S-doped carbons due to the less electroneutrality in C-S bond (electronegativities of 2.58 and 2.55, for C and S, respectively) [10]. Moreover, sulfur atom has a larger atomic radius (100 pm(picometre)) than nitrogen (65 pm) and carbon (70 pm). This large differences in atomic radius help the disruption of the carbon connection pattern. In another word, sulfur-doping will induce more defect sites and strain in the carbon framework, which may couple chemisorption of oxygen and facilitate charge localization. In addition, the lone pairs of sulfur atoms may easily interact with the surrounding electrolyte molecules due to the large polarizable d-orbitals in a sulfur atom (sulfur groups are known as soft nucleophiles). [9], [6] This effect is estimated to be much more pronounced in sulfur than that for nitrogen.

4.3. Lignin-derived ORR catalyst

Many groups have already reported the electrochemically active catalysts in the different forms of sulfur-doped carbon, however, it still needs to develop state-of-the-art, inexpensive, sustainable sulfur-doped catalyst for practical ORR application. In this dissertation, a novel and the simple synthetic pathway have been developed for sulfur-doped carbon derived from lignin. The electrochemical activity and durability of sulfur-doped carbon from lignin precursor are investigated. Following properties are desired in the sulfur-doped carbon from lignin: (i) high specific surface area with micro/mesoporosity which enhances oxygen interaction sides, (ii) high electrical/proton conductivity, (iii) high electrochemical sites with variable sulfur functional groups (sulfide(C-S-C)/oxidized sulfur(C-SO_x-C)) in the resulting material responsible for O_2 reduction, and (iv) high electrochemical stability under fuel cell operating conditions.

4.4. Supercapacitor application of S-doped carbon

Electrochemical capacitors (ESs), also called electro-double layer capacitors, are electrochemical devices in which an ion adsorption/desorption process is used to store the charge.[11,12] ESs have attracted a lot of attention over the past decades as energy storage devices due to their fast charge/ discharge rates and high power density.[13] These have a wide range of applications in hybrid electric vehicles, electronic devices, memory backup, etc. However, pure electrical double layer capacitors (EDLCs) based on a non-faradic process to store the charge are suffering from poor specific capacitance values, which limits their applications and wide spread use.[14,15] Many EDLCs are made of carbon materials such as activated carbon, carbon nanotubes, graphitic carbon, graphene, etc. An appealing route to enhance the capacitance of EDLC-based materials involves the addition of N, O, S or P heteroatom and/or MaXb (where M is a transition metal ion and X are O, S or OH-).[16,17,18,10] The add-atom is designed to enhance the capacitance of a material via the pseudocapacitive effect, which depends on storing the charge through a reversible faradic redox reaction.[19] In particular, sulfur atoms have been considered an interesting heteroatom dopant of carbon materials for energy applications.[20,21] First, the difference in electronegativity between carbon (2.55) and sulfur (2.58) facilitates the charge transfer in the C-S bonds which enhances the electrochemical performance and conductivity of unmodified carbon. [10,9] Second, sulfur molecules modify the electronic structure (e.g. electron density balance) of the carbon atoms and thus generates electroactive centers on the material surface or defects to enhance the electrocatalytic and capacitive performance of the carbon materials.[9, 22,]

4.5. Key goals

A large number of carbon-based materials for energy storage and fuel cell applications have been produced from fossil fuels. However, there are many concerns associated with using

petroleum-derived materials such as environmental pollution and unsustainable sources. Hence, It is urgent to develop environmentally friendly, sustainable and inexpensive carbon materials.[18] There are several studies reported on the application and utilization of nitrogen- and sulfur-doped biomass-derived carbon materials in supercapacitors and fuel cells,[8, 23,24,25,26] include only a few derived from lignin biomass.[27,28] Moreover, to the best of our knowledge, there is no report of self-sulfur doped carbon from lignin activated by in-situ experiment. In addition, to Lignin, a complex biopolymer, is a byproduct of pulp and paper industry.[29] Approximately 50 million tons of lignin are generated per year, out of which only 5% is converted into valuable products. [30,31,32,33] Therefore, there is a need to develop value-added products from lignin. This work examines lignin-derived sulfur self-doped carbon electrodes for use in supercapacitors and fuel cells. A simple, eco-friendly and scalable synthetic pathway has been chosen. Impacts of hydrothermal carbonization and thermal annealing on the capacitance of the final material have also been studied.

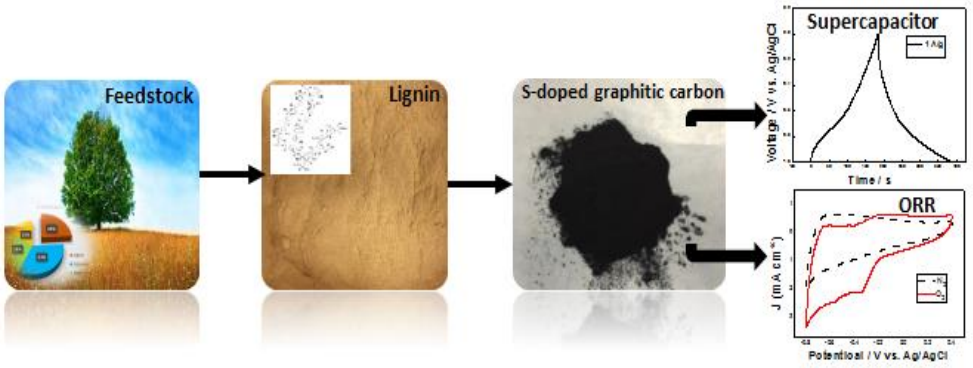

Figure 4-2 Abstract of chapter self S-doped material

4.6. Experimental

4.6.1. Chemicals

Commercially available calcium lignosulfonate lignin (Norlig A) was received from Lignotech company.[34] Organosolv lignin (sulfur-free lignin) was obtained from Lignol Innivations, Inc.[35] Potassium hydroxide (KOH) and polytetrafluoroethylene (PTFE, 60 wt. % dispersion in H_2O) were obtained from Sigma-Aldrich. Carbon black was received from Alfa Aesar. Ni foam was purchased from MTI Corporation. Commercial 10 wt % Pt/carbon was bought from Sigma-Aldrich. Chemicals were used as received unless it is mentioned in the text. Deionized water (18.2 MΩ.cm) was used as a solvent in the hydrothermal treatments.

4.6.2. Bio-char synthesis from lignin

Bio-char was synthesized via the hydrothermal carbonization (HTC) process which is easy and low-cost process.[36] For a typical synthesis, lignin (10 g) was mixed with 80 mL deionized water. The solution was placed into a 300 mL ultrasonic high-pressure reactor (Col-Int). The reactor was

equipped with sonication to enhance the mass transfer from the solid phase into the solvent phase and to increase the removal of oxygen from lignin during the hydrothermal treatment.[37] The reaction was carried out at 300 ℃ and 98 bar for 30 minutes.[38] Water in this reaction was under sub-critical conditions which had both liquid and vapor phases in equilibrium. After the HTC, the reactor was allowed to cool down to ambient temperature. The obtained brown aqueous suspension was filtered to isolate the produced bio-char from the solvent.

4.6.3. Preparation of sulfur self-doped carbon from bio-char

S-doped carbons were directly synthesized by the post-annealing process at elevated temperatures. In a typical procedure, 1 g bio-char was heated to the desired temperature (700 to 1000 ^{o}C) for 1 h under N_2 flow at a heating rate of 5 °C/min in the tubular furnace (Carbolite MTF-250). The obtained material was washed with 3 M HCl following by dilute water in order to remove calcium and other minerals. The produced S-doped carbons were labeled as SC-*x*, where *S* denotes the sulfur doping, C refers to carbon and *x* refers to the carbonization temperature in ^{o}C. Graphitic carbon C-850 (pristine) were obtained for comparison by applying the same procedures on bio-char derived from the sulfur-free lignin (Organosolv).

4.6.4. Physical characterization

Thermogravimetric (TGA) analysis was recorded by a Perkin Elmer thermo-gravimetric analyzer with a constant heating rate of 5 °C/min under N_2 flow and temperature ranging in 30 °C to 1000 °C. FTIR spectra of materials were collected by Nexus 670 FTIR spectrometer which uses a Smart ATR Nicolet. Operating conditions were fixed to average 16 scans at 1 cm^{-1} intervals and a resolution of 4 cm^{-1} scanned from 4000 to 400 cm^{-1}. Raman spectra of materials were collected on Horiba LABRam HR spectroscopy with excitation of 532 nm light source in order to detect graphitic carbon formation. The morphology of the synthesized materials was examined by

scanning electron microscope (SEM) (Hitachi SU-70 FE-SEM). The operation condition was 5 kV acceleration voltage under a vacuum atmosphere. The Brunauer-Emmett-Teller (BET) specific surface area and porosity properties were determined by applying N_2 adsorption/desorption isotherm with a NOVA surface analyzer. The X-ray photoelectron spectroscopic (XPS) analysis was performed on X-ray photoelectron spectrometer (ESCALAP250) with a monochromatic Al K alpha source (1486.6 eV, 20 kV, 250 W). The sp^2 carbon peak was adjusted to 284.6 eV to calibrate the XPS energy scale. Thermo Advantage software was applied for processing the XPS data.

4.6.5. Electrochemical Measurements

All electrochemical measurements in this study were performed on a CHI 660E electrochemical workstation (CH Instruments, Inc.) in a conventional three-electrode electrochemical cell in 1 M KOH aqueous electrolyte under ambient conditions. Silver/Silver chloride (Ag/AgCl) and platinum wire were used as a reference and counter electrodes, respectively. The working electrode was obtained by mixing the active material, carbon black, and PTFE binder with a weight ratio of 80:10:10. The resulting slurry was spread on a nickel foam current collector (1.5 cm x 3 cm) then dried at 80 °C overnight and pressed under a high pressure of 20 MPa. Geometric surface area of 0.32 cm^2 for the working electrode was achieved by using UHMW tape (CS-Hyde). Cyclic voltammetry (CV) measurements were conducted at different constant scan rates (1-100 mV s^{-1}) within the potential window -0.6 to 0.2 volts. Galvanostatic charge/discharge measurements were carried out to evaluate the capacitance and cyclability of the as-prepared electrodes at a range of constant current densities (5 to 20,000 mA/g) between -1.0 to 0.0 volts. Electrochemical impedance spectroscopy (EIS) analysis for the supercapacitor electrodes was conducted by applying an AC amplitude of 5 mV within the 10 MHz to 0.5 MHz frequency range. The

gravimetric specific capacitance (C_s, F g^{-1}) of electrodes was calculated from the galvanostatic discharge curves according to the equation (1):

$$C_s = \frac{I\Delta t}{m\Delta V} \quad (4.6)$$

where I is the discharge current (A), ΔV is discharging voltage, m is the mass of the active electrode material (g) and Δt is the discharge time. The volumetric capacitance (C_v, F/$cm^{3)}$ was calculated by the following equation:

$$C_v = \rho C_s \quad (4.7)$$

where C_s is specific capacitance, ρ is particle density calculated by equation 3[39,40]:

$$\rho = \frac{1}{V_t + (1/\rho_t)} \quad (4.8)$$

V_t is total pore volume cm^3/g and ρ_t is true density of carbon (2 g/cm^3).

The energy density (E, Wh kg^{-1}) and the power density (P, W kg^{-1}) were calculated as follows:

$$E = \frac{1}{8} C \left(\frac{F}{g}\right) \Delta V^2 (mvolt^2) \frac{1000\ g}{1\ kg} \frac{1\ h}{3600\ s} \quad (4.9)$$

$$P = \frac{E\left(\frac{Wh}{kg}\right) v\left(\frac{mvolt}{s}\right) \frac{3600\ s}{1\ h} \frac{1\ volt}{1000\ mvolt}}{\Delta V\ (volt)} \quad (4.10)$$

For the ORR measurements, the working electrode was prepared from an ink solution composed of 5 mg active material, 100 □L Nafion binder, and 300 □L ethanol. The mixture was sonicated for 30 min and 8 □L of the resulting ink were dropped onto a freshly cleaned rotational disc glassy carbon electrode (RDE, 3 mm diameter, CH Instruments Inc.). The prepared RDE was warmed to 70 ^{o}C to improve adhesion of the active material on the glassy carbon electrode surface.

0.1 M (80 mL) KOH solution was used as an electrolyte in a three-electrode cell with RDE. The obtained current was normalized by the geometric area of the active surface (mA/m^2). For kinetic measurement, the Koutecky-Levich equation (6) was applied at the potential from 0.4 and -0.8 V and for rotational speed range from 500 and 2500 rpm as follows.[41]

$$\frac{1}{J} = \frac{1}{J_k} + \frac{1}{B\omega^{0.5}} \qquad (4.11)$$

where, J is the current density, J_k is kinetic current density, ω was rotational speed, and B is the slope of K-L curve. The theoretical value of n can be calculated from following equation (7)

$$B = 0.2nF\left(D_{O_2}\right)^{2/3} C_{O_2} v^{-1/6} \quad (4.12)$$

where n is the number of electrons transferred per O_2 molecule during the oxygen reduction reaction, B is the slope of K-L curve, F is the faraday constant (96,485 C mol^{-1}), D_{O_2}(1.9×10−5 cm^2 s^{-1}) is the diffusion coefficient of O_2 in KOH electrolyte, C_{O_2}(1.2*10^{-6}) is concentration of O_2 in the electrolyte and ν (0.01 cm^2 s^{-1}) is the kinematic viscosity of the electrolyte). The obtained graphs were normalized to the area of the active surface area (mA/m^2). Scheme of a three electrode cell for ORR characterization depicted in Figure 4-4.

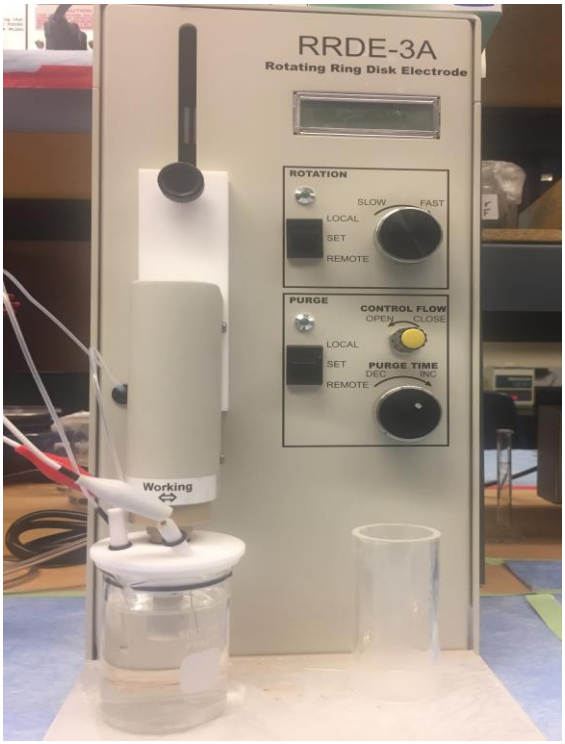

Figure 4-3: Photography of rotational disc electrode instrument

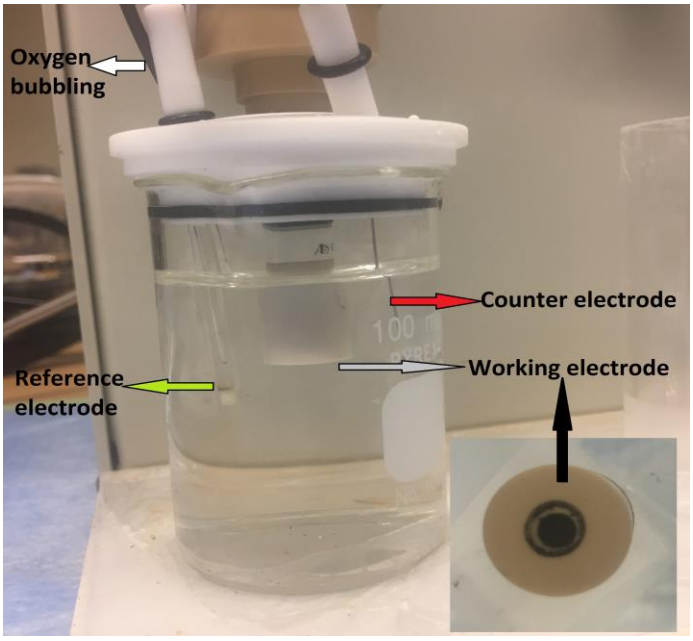

Figure 4-4 Scheme of a three electrode cell for ORR characterization

4.7.Results and discussion

4.7.1. Physical and chemical properties

The pathway for the synthesis of sulfur self-doped carbons is illustrated in Figure 4-5. The production of S-doped carbons has been designed to be simple, inexpensive, environmentally friendly, and easy to scale-up process. The as-prepared S-doped carbons were labeled as SC-*x*, where S denotes the sulfur self-doping, C refers to carbon and *x* refers to the carbonization temperature in ^{o}C. Carbon C-850 (pristine) was also synthesized by following the same procedures from sulfur-free (organosolv) lignin.

In this study, we used two types of lignin. First, Norlig A (calcium lignosulfonate) lignin which is separated from woody plants in H_2SO_4 solution to form black liquor and then, lignin was

precipitated by the addition of lime (CaO). [29] The elemental composition of Norlig A is 36.8 wt.% C, 37.3 wt.% O, 6.7 wt.% S, and 2.5 wt.% Ca as shown in Table 1. The sulfur and calcium contents originate from the manufacturing process. The presence of calcium and sulfur atoms enhances the electrochemical and surface activation properties of the as-prepared carbon materials, as discussed in following sections. The second type, signal (organosolv) is a lignin lacking sulfur and calcium atoms in its structure due to the use of organic solvents in the separation process.[29,35] Organosolv lignin contains 65.4 wt.% C and 35.6 wt.% O. Absence of sulfur and calcium atoms in the organosolv lignin limits the electrochemical and surface activation properties in the resulting carbon material (C-850). It is important to bear in mind that both the surface activating agent (calcium catalyst) and sulfur molecules (origin of lignin process) were used by in-situ synthesis process.

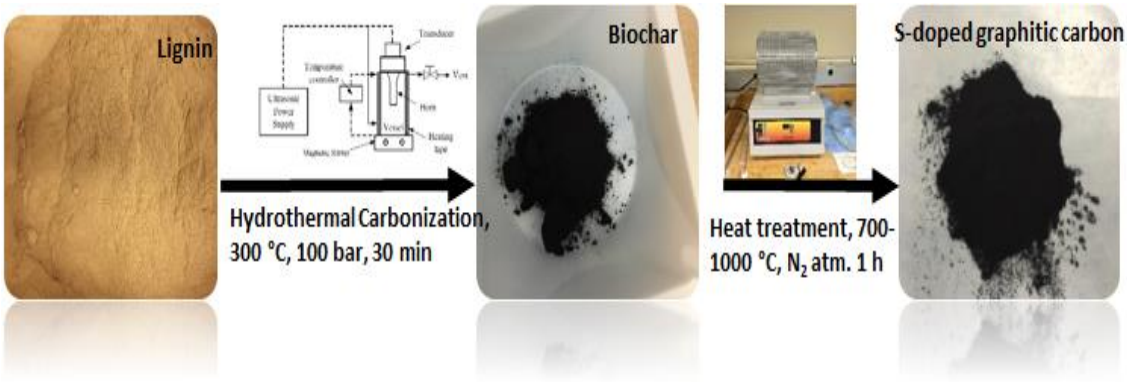

Figure 4-5 Synthesis pathway of S-doped carbon

TGA was used to investigate the thermal decomposition of lignin, bio-char and the as-prepared sulfur self-doped carbon materials as shown in (Figure 4-6(a)). Lignin, bio-char and SC-850 desorb water up to 150 °C. Lignin started to decompose at 200 °C and continued the decomposition up to 725 °C. The residual ash content of lignin is calculated to be 16 wt.% at 1000 °C. Approximately 41 wt.% of bio-char remains at 850 °C as shown in Figure 6(a). The TGA of the as-prepared SC-850 reflects its high thermal stability.

Lignin, biochar and S-doped carbons were analyzed by FTIR in order to determine the transformation of the functional groups during the preparation (Figure 4-6(b)). Several functional groups, characteristic of the lignin structure, are found. For instance, the IR peaks located at 1032, 1420, 1450, 1507, and 1593 cm^{-1} correspond to the C-H bonds and aromatic ring groups of lignin. The peak located at 2939 cm^{-1} is due to the vibration of the C-H bond of aliphatic carbon in the lignin structure. [30, 33] The –OH functional group of lignin displayed a peak around 3300 cm^{-1}. The characteristic IR peaks of the lignin such as –OH group disappeared in the IR spectra of the corresponding bio-char and as-synthesized carbon due to the breaking of the hydroxyl groups during the HTC and heat treatment steps[42].

Raman spectroscopy is a crucial technique to investigate the degree of graphitization for carbon materials. Figure 4-6 (c) displays two characteristic peaks in Raman spectra of the samples. The G band located at 1580 cm^{-1} corresponds to the graphitic carbon (sp^2) structure while the D band at 1360 cm^{-1} is associated with the disordered structure of the carbon-based materials.[43] The appearance of G and D bands in Raman spectra of the as-prepared sulfur self-doped carbons indicates that the structure consists of a combination of graphitic and disordered (amorphous) carbons. The intensity ratio of the D band (I_D) to G band (I_G) is an indicator of the formation of graphitization and disordered structure.[44,45] The lower I_D/I_G ratio corresponds to the higher degree

of graphitization in the resulting materials. The I_D/I_G ratios were found to be 0.83, 0.89, 0.97 and 1.01 for the SC-700, SC-850, SC-1000 and C-850, respectively confirm a high degree of graphitization. The slight enhancement in the I_D/I_G ratio may be attributed to destruction of well ordered-graphitic structures at the higher annealing temperatures.[46] It is assumed that the specific capacitance of a carbon-based material increases with the amorphous carbon content due to the large surface area of the disordered structure. However, the electrical conductivity of amorphous carbon is low. On the other side, graphitic carbon possesses an outstanding electrical conductivity because of its well-ordered crystalline structure, however, its surface area and pore size distribution are limited.[44] Thus, the graphitic/amorphous composition of carbon materials has been examined to obtain the optimum sample in point of electrochemical activity. In the present study, the SG850 (I_D/I_G of 0.89) displayed the highest electrochemical activity.

The N_2 adsorption/desorption isotherms and pore size distributions of the sulfur self-doped carbons are presented in Figure 4-6 (d,e). The BET surface area of the SC-700, SC-850, SC-1000, and C-850 were found to be 78, 660, 260, and < 20 m^2/g, respectively, as listed in Table 2. The total pore volume of SC-700, SC-850 and SC-1000 was found to be 0.05, 0.25 and 0.12 cc/g, respectively. It is worthwhile to mention that the surface area and pore sizes distribution of the as-prepared carbon samples were significantly influenced by the annealing temperature. Annealing temperature at 850 ^oC was found at an optimum temperature with regard to the high the BET surface area of the sample. At the low annealing temperature (700 °C), surface activation was not completed due to the insufficient thermal energy. The lower the BET surface area of SC-1000 caused by collapsing of the micro/meso pore at the higher annealing temperature and evaporation of the heteroatoms. [47,48] We further compared the BET surface area of SC-850 with respect to C-850 (calcium free lignin). The surface area of C-850 (< 20 m^2/g) is significantly lower than SC-

850. It is important to point out the synthetic strategy of both C-850 and SC-850 did not include any surface activation agent. As it mentioned in the previous section, the carbon material derived from the organosolv lignin does not present any calcium content while the carbon materials derived from the calcium lignosulfonate lignin displayed up to 2.5 wt.% calcium content. The high BET surface area of SC-850 imply that the calcium molecules may act as a surface activating agent during the annealing treatment. This observation is in accord with our previous finding that many metal catalyst (e.g., Mn, Fe) activates carbon surface.[49] The pore size distributions of samples displayed micro/meso porous structure shown in Figure 4-6(e). The pore size of SC-850 was found to be 1.5 nm (micropore) and 15 nm (mesopore).

The SEM micrographs of the synthesized sulfur self-doped carbon materials are presented in Figure 4-7. All the sulfur self-doped carbon samples displayed a similar morphology composed of spherically shaped particles that stick to each other in a random fashion with a size ranging from 0.5 to 3 μm. The main dissimilarity in the samples morphology was the size of the spherical shapes. The morphology of C-850 is different from SC-850 where microstructure of the C-850 is non-porous and consists of fused carbon spheres that form a compact structure

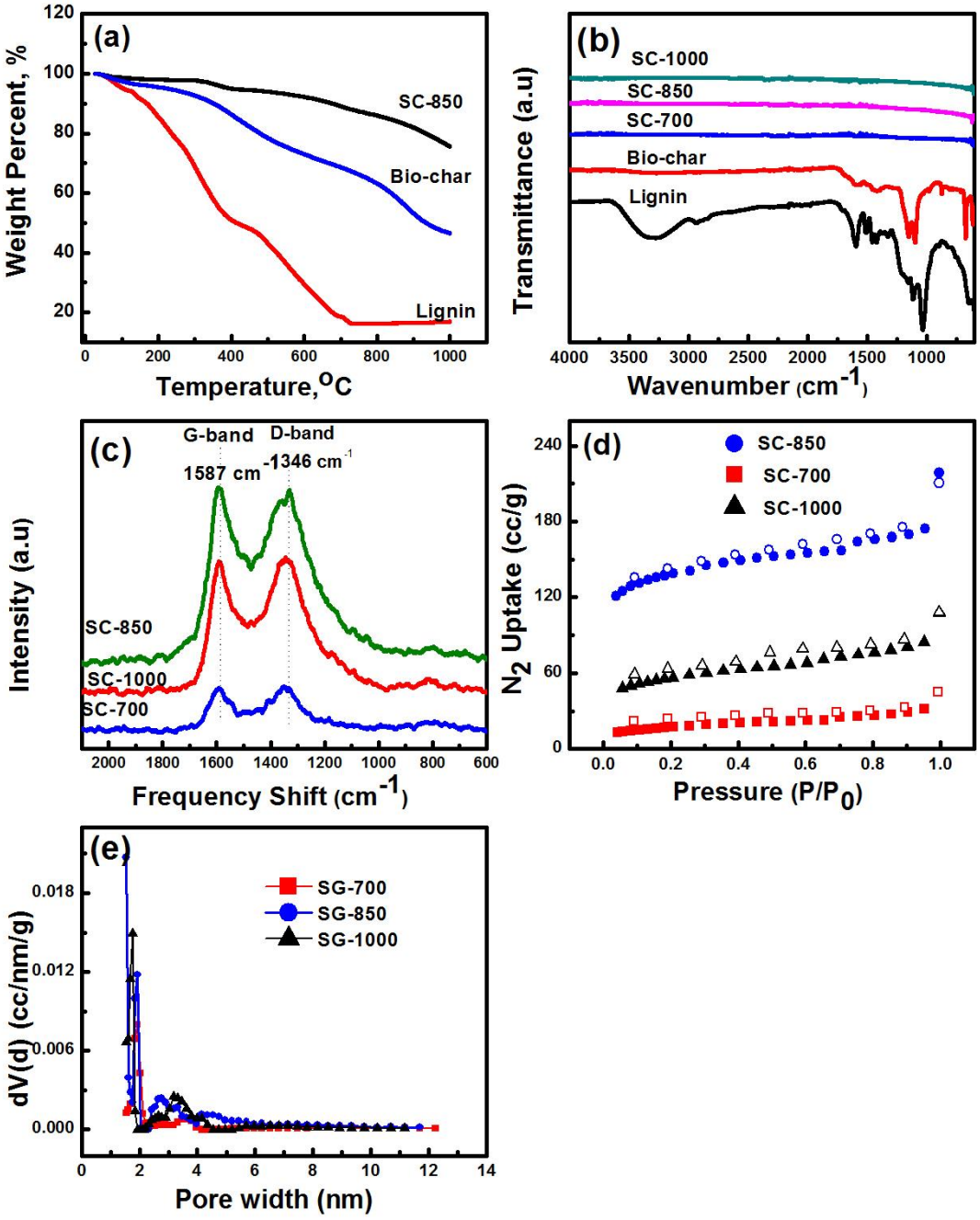

Figure 4-6: (a) TGA curves of lignin, adenine and biochar, (b)) FTIR spectra of lignin, bio-char and S-doped carbons, (c) Raman spectra S-doped carbons, (d) Nitrogen uptake at 77 K, (e) pore size distributions calculated from carbon model using

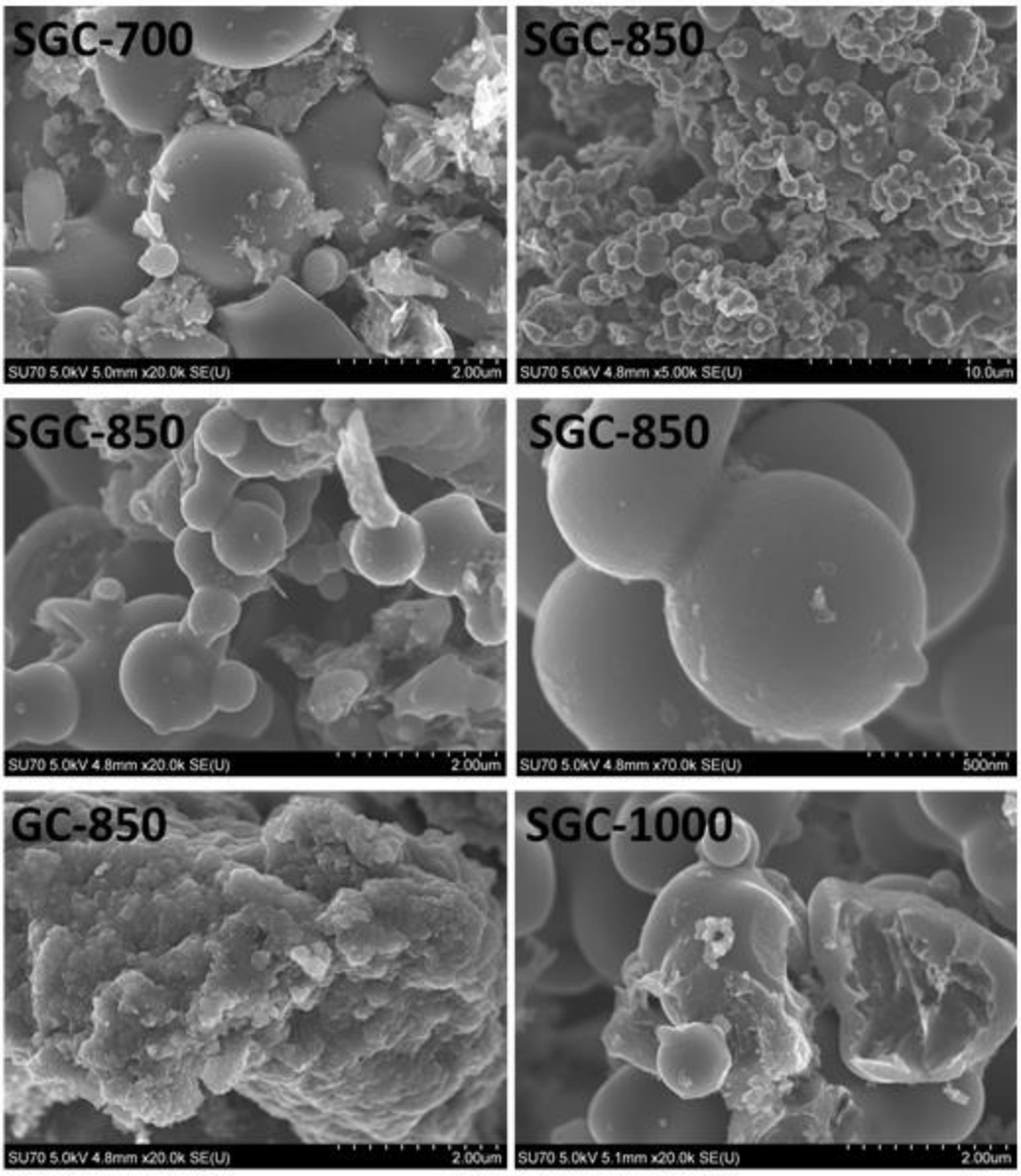

Figure 4-7: SEM image of (a) SC-700, (b), (c), (d) SC-850 at variable magnification (e) SGC100 and (f) C-850

4.7.2. XPS results

The surface chemical composition of sulfur self-doped carbons materials was investigated by X-ray photoelectron spectroscopy (XPS). The surface elemental composition and the corresponding functional groups are listed in Table 1. The survey scans of the sulfur self-doped carbon materials are shown in Figure 4.8. Carbon, oxygen, and sulfur peaks are located at 288.4, 532 and 164.7 eV, respectively. The carbon content has been significantly increased during the HTC and annealing processes to be ~1.6 times that in pure lignin as shown in Table 1. The observed enhancement in the carbon content of S-doped carbons reflects the efficiency of the carbonization process and could be attributed to the low volatility of the carbon molecules/compounds compared to those of the dopant such as oxygen and sulfur. In particular, the oxygen content has been significantly decreased through the HTC and thermal annealing steps being 5 to 6 times less than that before the treatment, due to the deoxygenation of many functional groups (e.g., hydroxyl and carboxyl groups) which is consistent with FTIR results.[50] The S/C ratio slightly decreased with the increase of the annealing temperature due to the volatility of sulfur compounds. The bulk elemental composition of lignin was compared with surface composition XPS data (e.g. 5-10 nm) as shown in Table 1. The variation between the XPS and bulk elemental analysis data arises from the fact that XPS detects the surface of the materials (e.g. 5-10 nm), while C/H/S elemental analysis examines the bulk composition.[51] [52] The C *1s*, O 1s and S *2p* high-resolution core-level spectra of the as-prepared samples are depicted in Figure 8. For XPS deconvolution of the C *1s*, the main peak located at 284.4 eV in Figure 8b is attributed to the C=C group. The two small overlapped peaks observed at 285.6 eV and 286.5 eV are attributed to C-O, C=O and O-C=O functional groups. [52] Another peak located at 283.9 eV is assigned to C-S groups[53,54], which is consistent with the high-resolution core-level sulfur spectrum. The high-

resolution XPS core-level scan of the O *1s* is presented in Figure 8(c). Three types of oxygen functional groups can be identified from the spectrum. The main peak located at 531.2 eV refers to the C=O bond while the small peaks at 531.5 and 532.9 eV correspond to O-CO/C-OH bonds[55]. Careful examination of the S *2p* high-resolution core-level spectra indicates the presence of three types of sulfur functional groups as shown in Figure 8 (d, e, f). The two core peaks located at 164 and 165.3 eV are assigned to sulfide (-S-C-S) and sulfoxide groups.[43,24] The relatively small peak seen at higher energy 168.6 eV is ascribed to -C-SO_2-C bonds (sulfone bridge)[53,56]. The effect of variable sulfur functional groups is discussed in the electrochemical results (see below).

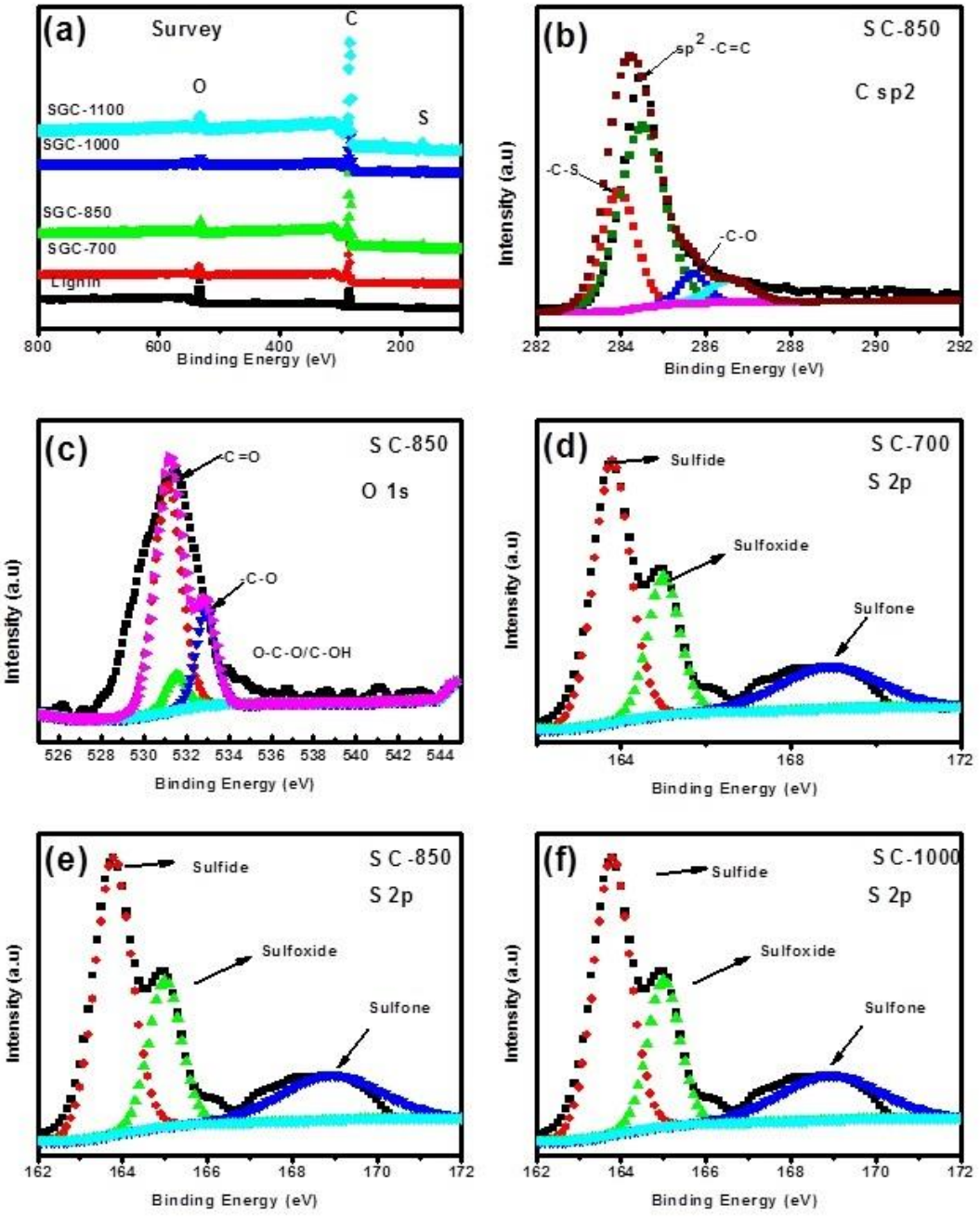

Figure 4-8: XPS analysis (a) survey spectra of lignin, SC-700, SC-850 and SC-1000, (b) High resolution C 1s core level analysis of SC-850, (c) High resolution O 1s core level analysis of SC-850, (d) High resolution S *2p* core level analysis of SC-700, (e) High resolution S *2p* core level analysis of SC-850, (f) High resolution S *2p* core level analysis of SC-1000

4.7.3. Electrochemical results

Galvanostatic charge/discharge measurements were conducted in a three-electrode configuration to evaluate the electrochemical performance of the S-doped carbons as electrode materials in supercapacitors. As shown in Figure 4-9(a), all the S-doped carbons displayed nearly isosceles triangular-shaped galvanostatic charge/discharge. Furthermore, the galvanostatic charge-discharge measurements were performed at different current densities (5 to 20,000 mA/g). The SC-850 maintained the triangular-shaped galvanostatic charge/discharge curves even at high current densities (up to 10,000 mA/g) as shown in Figure 4-9(c). These interesting findings indicate that the S-doped carbons possess a near ideal EDLC behavior with a fast charge propagation. The specific capacitance (Cs, F/g) of the S-doped carbons was calculated according to equation (1). Although SC-700 displayed the highest sulfur content as indicated by the XPS data, its specific capacitance value (124 F/g at 1 A/g) is smaller than that of the SC-850 (202 F/g at 1 A/g) as shown in Table 2. The reason for the pronounced high specific capacitance of the SC-850 sample could be attributed to its high surface area (660 m^2/g) which is 8 times higher than that of SC-700 sample. The high surface area in conjunction with the enhanced micro/mesoporosity contents facilitate mass transport through the pores of the electrode material and provide more active sites for the electrosorption of electrolyte ions and thus could account for the observed high specific capacitance for the SC-850 sample, which is 1.6 times greater than SC-700. Another factor that may contribute to the observed high capacitance of the SC-850 sample is that the higher amorphous carbon content. The SC-850 sample displayed higher I_D/I_G ratio than the SC-700 sample as shown in Table 2. It is already addressed before that it is assumed that amorphous carbon possesses larger specific capacitance value while the graphite exhibits more conductivity. Although the specific capacitance of SC-700 is the lowest, the conductivity of the SGC700 is

higher than other samples. This finding is consistent with EIS data and is examined in depth. The higher capacitance of the SC-850 compared with the SC-1000 (146 F/g at 1 A/g) may be due to the synergistic effect of higher surface area, larger microspore volume and higher S/C ratio. Moreover, the specific capacitance of the SC-850 (225 F/g at 0.5 A/g) is about 5 times that of the un-doped C-850 (organosolv-derived carbon) which is found to be 44 F/g at 0.5 A/g. The higher capacitance for the SC-850 compared with that of the C-850 could be attributed to the higher surface area with accessible porosity and the presence of sulfur atoms which contribute to pseudocapacitance, facilitate/ improve the ion transport and increase the number of the electroactive centers. The proposed faradaic reaction of sulfur-containing functional groups was reported previously with following reactions[57]

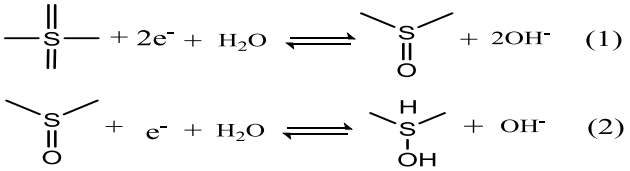

The first and second faradaic reactions contribute to sulfone and sulfoxide functional groups, respectively. In addition, the sulfide functional groups contribute to enhancing the charge transfer on the surface. The sulfide functionalities may affect the further polarization of carbon surface by a combination of electron-rich sulfide groups with carbon structure.[57] These statements are consistent with our data that SC-850 has 65.7 sulfides, 27.5 sulfoxides and 6.6 at. % sulfone functional groups in its structure. At variable current densities, the specific capacitances of the SC-850 sample were found to be 185, 147, and 95 F/g at 2, 5 and 10 A/g, respectively. The outstanding performance even at high current densities is caused by fast ion transfer on the electrode surface. We further measured the volumetric specific capacitance of SC-850 from equation (3). The volumetric capacitance of SC-850 was found to be 300, 269, and 195 F/cm^3 at 0.5, 1 and 10 A/g

current densities, respectively. The obtained specific capacitance value was compared with literature. Although the specific capacitance of SC-850 electrode is lower than many heteroatom-doped/templated carbon derived materials, [58,59,60,61] the specific capacitance value, 225 F/g at 0.5 A/g, is still higher or comparable with reported capacitance values for many biomass-based carbon electrodes.[62,63,64]

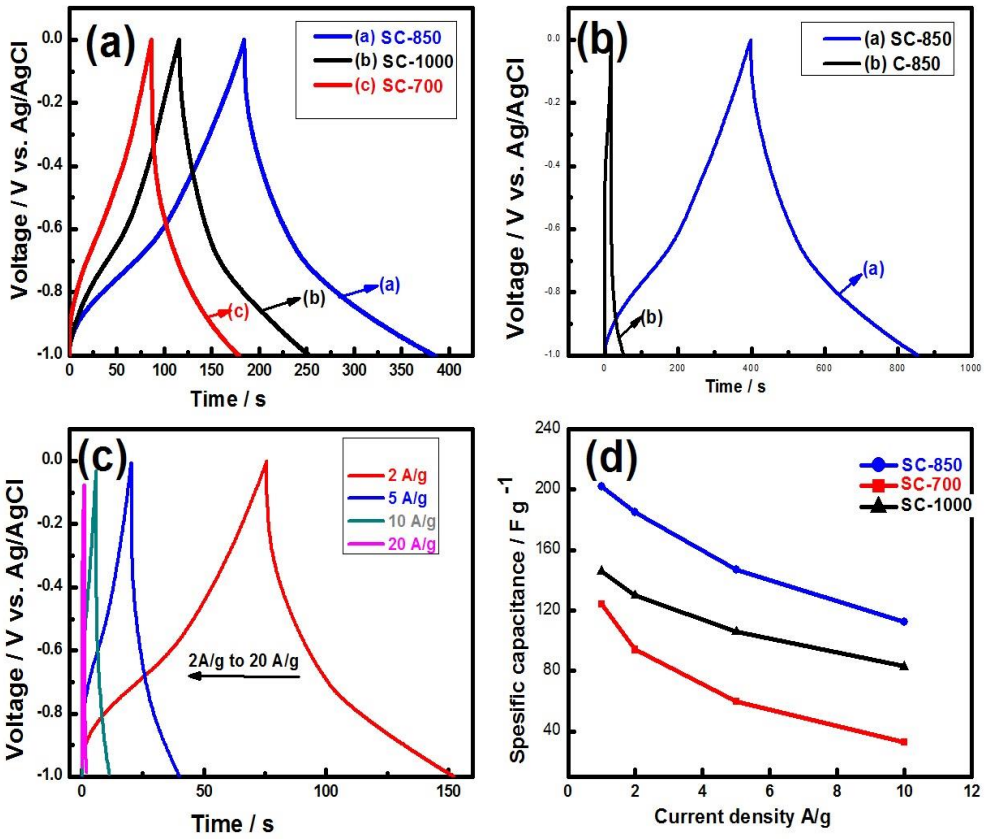

Figure 4-9: (a) Charge-discharge curves of SC-700, SC-850 and SC-1000 at 1 A g-1, (b) Charge-discharge curves of SC-850 and C-850 at 0.5 A. g-1, (c) Charge-discharge curves of SC-850 at 2, 5, 10, 20 A g-1, (d) Specific capacitance of obtained materials (all experiments were conducted in 1 M KOH electrolyte solution).

To examine the presence of pseudocapacitance in the as-prepared S-doped carbon materials, cyclic voltammetry measurements were performed using a three-electrode system. The CV data of the S-doped carbons revealed that SC-850 has the highest CV area and SC-700 has the lowest CV area, which is consistent with the galvanostatic charge/discharge measurements. The SC-850 sample displayed nearly perfect rectangular shaped CV curve at 20 mV s^{-1} scan rate as shown in Figure 4-10 (a) which indicates ideal double layer capacitor behavior. Close examination of the SC-850 sample's CVs at slow scan rates indicated the presence of pseudocapacitive behavior where redox peaks appeared around -0.3 volts as shown in Figure 4-10 (b). This peak could be attributed to the reversible Faradaic redox reaction of the sulfone and sulfoxide surface functionalities. The XPS data showed the presence of some oxygen functionalities which may also be contributed to the observed pseudocapacitance. The increased electrical resistance and poor penetration of the electrolyte into the electrode material pore at fast scan rates could account for the observed slight distortion of the CVs of the SC-850 sample from the rectangular shape as shown in Figure 4-10(c).

Electrochemical impedance spectroscopy (EIS) measurements were conducted via applying an AC amplitude of 5 mV in the frequency range from 10 MHz to 500 kHz to examine the interfacial properties and electron transfer kinetics of the as-prepared S-doped carbon materials and to understand their electrochemical behavior. Nyquist plots of the S-doped carbon materials are shown in Figure 4-10 (d). They are similar, consisting of a semicircular part in the high-frequency region and a linear part in the low-frequency region. In the high-frequency region, the intercept of the semicircular part of the Nyquist plot with the real impedance axis (Z'-real axis) gives the equivalent series resistance (ESR). For an electrochemical capacitor, the ESR governs the rate of the charged–discharge process and it is a combination of the electrolyte ionic resistance,

intrinsic and contact resistances of the nickel foam current collector and the electrode material. The SC-700 and SC-850 electrodes displayed almost the same ESR of ~ 5.7 Ω with the SC-850 electrode being slightly more conductive than the SC-700 electrode as shown in the inset of Figure 4-10 (d). The observed relatively high resistance (6.3 Ω) for the SC-1000 electrode with respect to the other electrodes could be attributed to the poor accessibility of the electrolyte to the electrode material which resulted in slow electron and ion transfer rates. In the high-frequency region, the diameter of the semicircular part of the Nyquist plot gives the charge transfer resistance (R_{ct}) which originates from the electron transfer process (e.g. Faradic reactions) at the electrode surface. The SC-700 sample displayed smaller R_{ct} value (0.5 Ω) than that of the SC-850 sample (0.7 Ω). This slight change in the conductivity may be assigned to the presence of higher graphitic carbon content in the SC-700 as compared to SC-850. These findings are in agreement with the Raman data which showed that SC-700 has the lowest I_D/I_G ratio. In the low-frequency region, the linear part of the Nyquist plot for the SC-850 sample is obviously more vertical than that for the other S-doped materials, which is indicative of a lower ionic diffusion resistance, resulting in enhanced capacitive performance and faster ionic diffusion through the electrode material facilitated by its high surface area and mesoporous nature. It is clear that the EIS measurements support the assumption that the observed high specific capacitance for the SC-850 sample is due to a synergistic effect of the high surface area, mesoporous nature, and chemical and structural compositions.

It is important to test the cycling degradation of the supercapacitor electrode materials. The SC-850 sample displayed excellent cycling stability after 10,000 cycles at 5 A/g with a retention of specific capacitance ~100% as shown in Figure 4-10 (e, f). Interestingly, the specific capacitance slightly increased during the charge-discharge cycling as shown in Figure 4-10(a).

This increase in capacitance could be explained by the physical opening of clogged pores upon cycling. [65] The long cycle life of the tested electrodes reflects the reversibility of the Faradic redox process and high chemical and structural stability of the S-doped carbons, which make them potential candidates as a highly stable electrode material for supercapacitors.

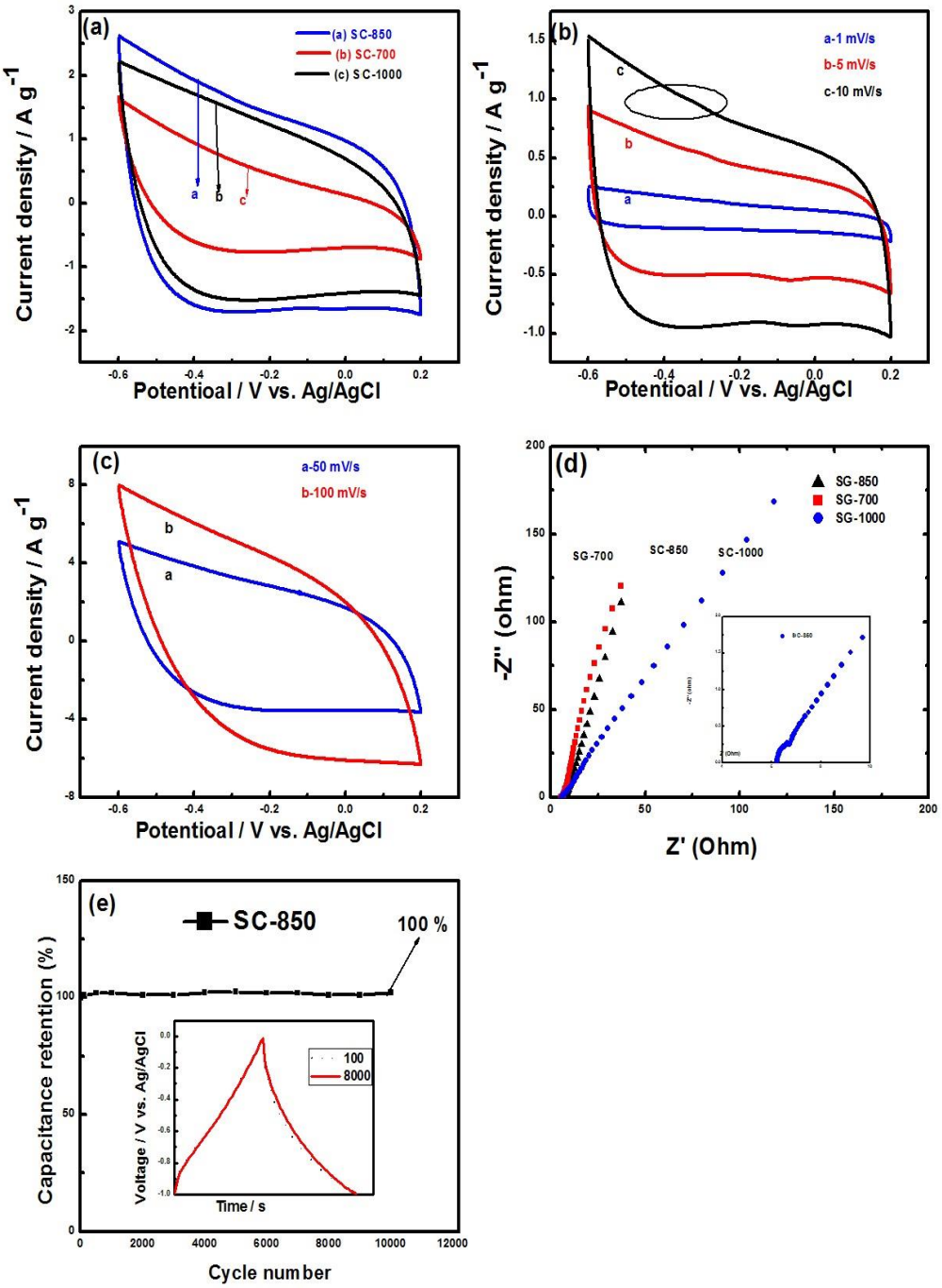

Figure 4-10: CV curves of SC-700, SC-850 and SC-1000 at 20 mV s-1 scan rate, (b) CV curves of SC-850 at scan rates of 1 to 10 mV s-1, (c) CV curves of SC-850 at different scan rate from 50 to 100 mV s-1, (d) Nyquist plot of SC-700, SC-850 and SC-1000, (e) The cycling performance of SC-850 (all experiments were performed in 1 M KOH electrolyte solution)

4.7.4. ORR results

We further investigated the capability of the SC-850 sample as a potential ORR electrocatalyst. The SC-850 sample was selected among the as-prepared sulfur self-doped carbon materials because of the optimum sample in point of supercapacitors. For comparison, commercial 20 % Pt/C catalyst was tested under the same conditions. The CV and linear sweep voltammetry (LSV) measurements were conducted in O_2 or N_2 saturated 0.1 M KOH aqueous electrolyte in order to assess the electrocatalytic activity of the SC-850 sample toward the ORR. As can be seen in Figure 11-(a), the collected CV curves using SC-850 as a working electrode material within the potential window +0.4 to -0.8 volts in O_2-saturated 0.1 M KOH solution, exhibited well-defined oxygen cathodic reduction peaks centered around -0.33 volts while the CV recorded in N_2- saturated 0.1 M KOH solution did not display any characteristic redox peaks (i.e., is featureless). The observed enhancement in the CV area demonstrates the electrochemical activity of the SC-850 towards the oxygen reduction reaction. This may be explained by the fact that sulfur doping provides extra catalytic sites for the ORR and ensures efficient electrolyte ion migration and electron transport. In addition, it is well known that the catalytic active sites in the N, P, B doped carbon are predominantly caused by atomic charge density due to the higher electroneutrality of N, P, B respect to carbon. On the other hand, because of close electroneutrality between C-S bonding , the defined redox cathodic peak in S-doped carbon may be caused by tailor spin density as it reported before by Huang et al.[10] In order to compare the CV plot of SC-850 with that of the commercially available Pt/C catalyst, the CV plot of 20 wt.% Pt/C was recorded under the same conditions as shown in Figure4-11 (b). The area under the CV curve of the commercial Pt/C catalyst is enhanced in the O_2 saturated electrolyte with respect to that obtained in the N_2 saturated electrolyte, and a characteristic oxygen reduction peak was observed around -0.37 V. The ORR peak for the SC-850

sample appeared at a more positive potential with respect to that recorded on the commercial Pt/C catalyst. In addition to the CV measurements, an LSV experiment was also carried out on rotational glassy carbon disk electrode at speeds from 500 to 2500 rpm in the potential range from 0.4 to -0.8 V at 5 mV s^{-1} scan rate. The LSV response of the SC-850 and Pt/C 20 wt.% at 5 mV s^{-1} scan rate is shown in Figure 4-11(d, e). The onset potentials are observed to be -0.17 and -0.06 V (Ag/AgCl) for the SC-850 and Pt/C, respectively. The SC-850 sample displayed a comparable limiting current to the Pt/C catalyst at the potential of -0.45 V and higher limiting current at a more negative potential. This finding indicates that the SC-850 sample has an excellent ORR activity.[66] The current density is directly proportional to rotational speed and the corresponding K-L curve shows good linearity between J^{-1} and the inverse of square root of rotational speed which indicates a first-order reaction toward O_2 reduction (Figure 4-11(f)).[67] Four-electron pathway for reducing O_2 is highly desirable to obtain optimum energy capacity for the ORR applications and to avoid hydrogen peroxide, which is poisonous to the catalyst, as an intermediate. The number of electrons transferred per amount O_2 during the oxygen reduction reaction was calculated from Equations 6 and 7. The transferred electron number (*n*) is calculated to be 3.4 to 2.7 in the potential range from -0.8 to -0.7 mV, respectively, which implying a four-electron oxygen reduction reaction. As previously reported, owing to an asymmetric atomic spin density between carbon and sulfur atoms, the resulting doped structure provides extra active sites for O_2 surface adsorption.[68] These favorable active sites for diatomic adsorption could efficiently weaken O-O bonding and enable the direct reduction of oxygen into OH via a four-electron process.[69,70]

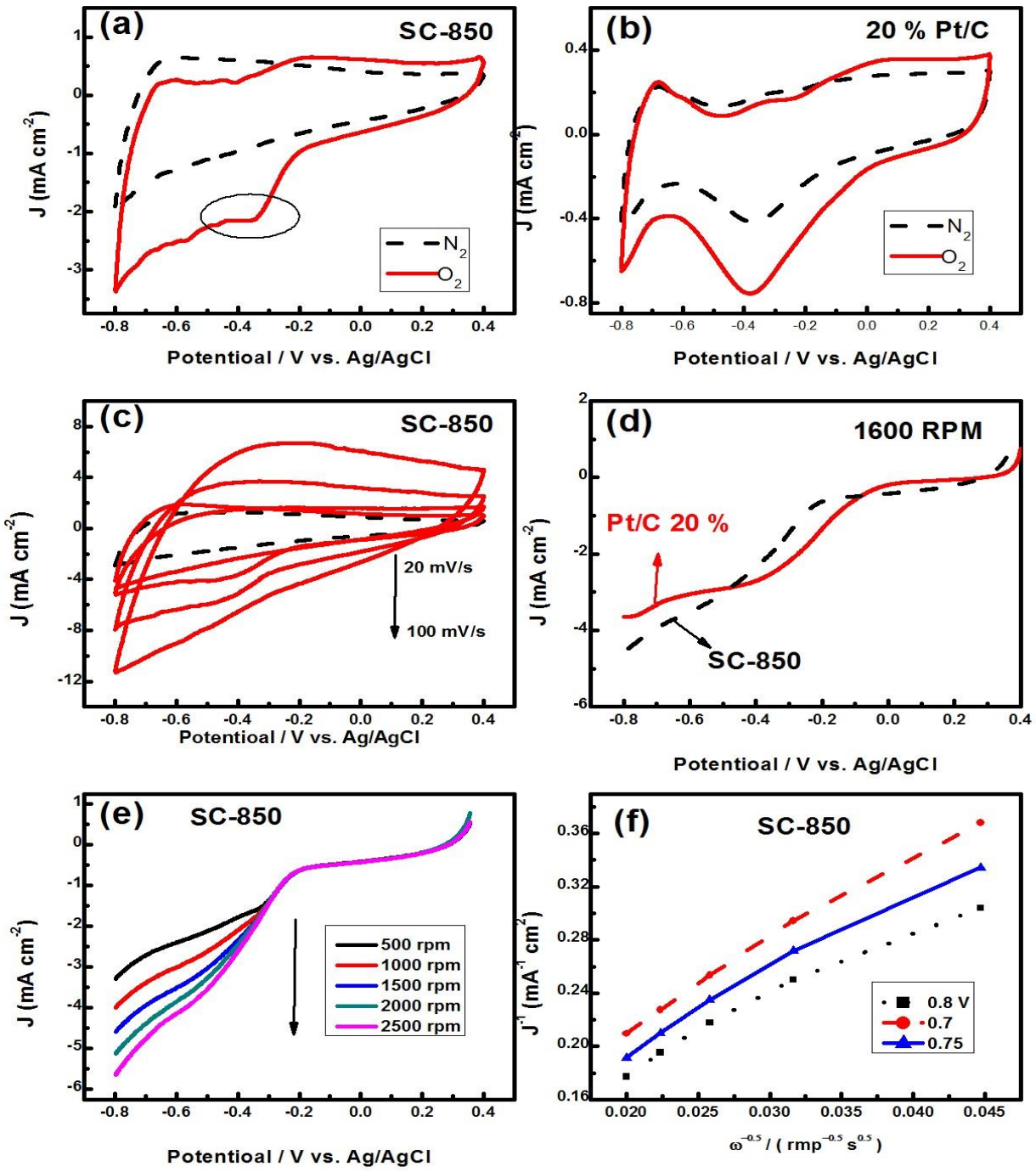

Figure 4-11: CV curves of (a) SC-850 (b) 20 wt.% Pt/C in N_2/O_2-saturated 0.1 M KOH electrolyte at 10 mV scan rate, (c) CV curve of SC-850 in N_2/O_2-saturated 0.1 M KOH electrolyte at variable scan rate, (d) RDE voltammograms for SC-850 and 20 wt.% Pt/C in O_2-saturated 0.1 M KOH electrolyte rotation speed of 1600 rpm, (e) RDE voltammograms in O_2-saturated 0.1 M KOH electrolyte (rotation speed from 500 to 2500 rpm, sweep rate 5 mV s-1), and (e) K–L plots derived from the RDE measurements at the potential between -0.6 to -0.8 V.

4.8. Conclusions

In this work, we have shown that sulfur self-doped carbon materials were successfully synthesized from commercially available lignin via hydrothermal carbonization followed by thermal annealing. A simple, inexpensive and environmentally benign synthesis pathway has been developed. The as-prepared SC-850 sample exhibits the high BET surface area (660 m^2/g) with abundant micro/meso porous structure. The SC-850 demonstrates an excellent capacitive behavior of 225 F/g at 0.5 A/g current density in 1.0 M KOH) and high durability up to 10,000 cycles at a harsh condition of 5 A/g current density. Furthermore, the SC-850 exhibited a well-defined cathodic peak and high electrochemical activity toward the ORR process in 0.1 M KOH electrolyte. In conclusion, the inexpensive and sustainable byproduct lignin has been easily converted into porous carbon, and the obtained material can further be utilized for energy storage and fuel cell application.

4.9 References

1. Choi, C. H.; Kwon, H. C.; Yook, S.; Shin, H.; Kim, H.; Choi, M., Hydrogen peroxide synthesis via enhanced two-electron oxygen reduction pathway on carbon-coated Pt surface. *The Journal of Physical Chemistry C* **2014,** *118* (51), 30063-30070.
2. Song, C.; Zhang, J., Electrocatalytic oxygen reduction reaction. In *PEM fuel cell electrocatalysts and catalyst layers*, Springer: 2008; pp 89-134.
3. (a) Chen, P.; Wang, L. K.; Wang, G.; Gao, M. R.; Ge, J.; Yuan, W. J.; Shen, Y. H.; Xie, A. J.; Yu, S. H., Nitrogen-doped nanoporous carbon nanosheets derived from plant biomass: an efficient catalyst for oxygen reduction reaction. *Energ Environ Sci* **2014,** *7* (12), 4095-4103; (b) Liu, X. J.; Zhou, Y. C.; Zhou, W. J.; Li, L. G.; Huang, S. B.; Chen, S. W., Biomass-derived nitrogen self-doped porous carbon as effective metal-free catalysts for oxygen reduction reaction. *Nanoscale* **2015,** *7* (14), 6136-6142.
4. Brun, N.; Wohlgemuth, S. A.; Osiceanu, P.; Titirici, M. M., Original design of nitrogen-doped carbon aerogels from sustainable precursors: application as metal-free oxygen reduction catalysts. *Green Chem* **2013,** *15* (9), 2514-2524.
5. Liang, H. W.; Wu, Z. Y.; Chen, L. F.; Li, C.; Yu, S. H., Bacterial cellulose derived nitrogen-doped carbon nanofiber aerogel: An efficient metal-free oxygen reduction electrocatalyst for zinc-air battery. *Nano Energy* **2015,** *11*, 366-376.

6. Wohlgemuth, S. A.; White, R. J.; Willinger, M. G.; Titirici, M. M.; Antonietti, M., A one-pot hydrothermal synthesis of sulfur and nitrogen doped carbon aerogels with enhanced electrocatalytic activity in the oxygen reduction reaction. *Green Chem* **2012,** *14* (5), 1515-1523.
7. Bashyam, R.; Zelenay, P., A class of non-precious metal composite catalysts for fuel cells. *Nature* **2006,** *443* (7107), 63-66.
8. Yu, X.; Park, S. K.; Yeon, S. H.; Park, H. S., Three-dimensional, sulfur-incorporated graphene aerogels for the enhanced performances of pseudocapacitive electrodes. *J Power Sources* **2015,** *278*, 484-489.
9. Kiciński, W.; Szala, M.; Bystrzejewski, M., Sulfur-doped porous carbons: Synthesis and applications. *Carbon* **2014,** *68*, 1-32.
10. Yang, Z.; Yao, Z.; Li, G.; Fang, G.; Nie, H.; Liu, Z.; Zhou, X.; Chen, X. a.; Huang, S., Sulfur-doped graphene as an efficient metal-free cathode catalyst for oxygen reduction. *Acs Nano* **2011,** *6* (1), 205-211.
11. Simon, P.; Gogotsi, Y., Materials for electrochemical capacitors. *Nature materials* **2008,** *7* (11), 845-854.
12. Candelaria, S. L.; Shao, Y.; Zhou, W.; Li, X.; Xiao, J.; Zhang, J.-G.; Wang, Y.; Liu, J.; Li, J.; Cao, G., Nanostructured carbon for energy storage and conversion. *Nano Energy* **2012,** *1* (2), 195-220.
13. Luo, H.; Liu, Z.; Chao, L.; Wu, X.; Lei, X.; Chang, Z.; Sun, X., Synthesis of hierarchical porous N-doped sandwich-type carbon composites as high-performance supercapacitor electrodes. *J Mater Chem A* **2015,** *3* (7), 3667-3675.
14. Wang, G.; Zhang, L.; Zhang, J., A review of electrode materials for electrochemical supercapacitors. *Chem Soc Rev* **2012,** *41* (2), 797-828.
15. Zhi, M.; Xiang, C.; Li, J.; Li, M.; Wu, N., Nanostructured carbon–metal oxide composite electrodes for supercapacitors: a review. *Nanoscale* **2013,** *5* (1), 72-88.
16. Wei, T. Y.; Wei, X. L.; Gao, Y.; Li, H. M., Large scale production of biomass-derived nitrogen-doped porous carbon materials for supercapacitors. *Electrochimica Acta* **2015,** *169*, 186-194.
17. (a) Yuan, C. Q.; Liu, X. H.; Jia, M. Y.; Luo, Z. X.; Yao, J. N., Facile preparation of N- and O-doped hollow carbon spheres derived from poly(o-phenylenediamine) for supercapacitors. *J Mater Chem A* **2015,** *3* (7), 3409-3415; (b) Liu, Q.; Duan, Y. X.; Zhao, Q. P.; Pan, F. P.; Zhang, B.; Zhang, J. Y., Direct Synthesis of Nitrogen-Doped Carbon Nanosheets with High Surface Area and Excellent Oxygen Reduction Performance. *Langmuir* **2014,** *30* (27), 8238-8245.
18. Xie, Q.; Bao, R.; Zheng, A.; Zhang, Y.; Wu, S.; Xie, C.; Zhao, P., Sustainable Low-Cost Green Electrodes with High Volumetric Capacitance for Aqueous Symmetric Supercapacitors with High Energy Density. *Acs Sustain Chem Eng* **2016**.
19. Zhang, L. L.; Zhao, X. S., Carbon-based materials as supercapacitor electrodes. *Chem Soc Rev* **2009,** *38* (9), 2520-2531.
20. Chen, X.; Chen, X. H.; Xu, X.; Yang, Z.; Liu, Z.; Zhang, L. J.; Xu, X. J.; Chen, Y.; Huang, S. M., Sulfur-doped porous reduced graphene oxide hollow nanosphere frameworks as metal-free electrocatalysts for oxygen reduction reaction and as supercapacitor electrode materials. *Nanoscale* **2014,** *6* (22), 13740-13747.
21. Wang, L.; Gao, Z.; Chang, J.; Liu, X.; Wu, D.; Xu, F.; Guo, Y.; Jiang, K., Nitrogen-Doped Porous Carbons As Electrode Materials for High-Performance Supercapacitor and Dye-Sensitized Solar Cell. *Acs Appl Mater Inter* **2015,** *7* (36), 20234-20244.
22. Zhang, D. Y.; Hao, Y.; Zheng, L. W.; Ma, Y.; Feng, H. X.; Luo, H. M., Nitrogen and sulfur co-doped ordered mesoporous carbon with enhanced electrochemical capacitance performance. *J Mater Chem A* **2013,** *1* (26), 7584-7591.
23. Cai, J.; Niu, H.; Li, Z.; Du, Y.; Cizek, P.; Xie, Z.; Xiong, H.; Lin, T., High-Performance Supercapacitor Electrode Materials from Cellulose-Derived Carbon Nanofibers. *Acs Appl Mater Inter* **2015,** *7* (27), 14946-14953.

24. Si, W. J.; Zhou, J.; Zhang, S. M.; Li, S. J.; Xing, W.; Zhuo, S. P., Tunable N-doped or dual N, S-doped activated hydrothermal carbons derived from human hair and glucose for supercapacitor applications. *Electrochimica Acta* **2013,** *107*, 397-405.
25. Deng, J.; Li, M.; Wang, Y., Biomass-derived carbon: synthesis and applications in energy storage and conversion. *Green Chem* **2016,** *18* (18), 4824-4854.
26. Yu, W. H.; Wang, H. L.; Liu, S.; Mao, N.; Liu, X.; Shi, J.; Liu, W.; Chen, S. G.; Wang, X., N, O-codoped hierarchical porous carbons derived from algae for high-capacity supercapacitors and battery anodes. *J Mater Chem A* **2016,** *4* (16), 5973-5983.
27. Jeon, J.-W.; Zhang, L.; Lutkenhaus, J. L.; Laskar, D. D.; Lemmon, J. P.; Choi, D.; Nandasiri, M. I.; Hashmi, A.; Xu, J.; Motkuri, R. K.; Fernandez, C. A.; Liu, J.; Tucker, M. P.; McGrail, P. B.; Yang, B.; Nune, S. K., Controlling Porosity in Lignin-Derived Nanoporous Carbon for Supercapacitor Applications. *Chemsuschem* **2015,** *8* (3), 428-432.
28. Graglia, M.; Pampel, J.; Hantke, T.; Fellinger, T.-P.; Esposito, D., Nitro Lignin-Derived Nitrogen-Doped Carbon as an Efficient and Sustainable Electrocatalyst for Oxygen Reduction. *Acs Nano* **2016,** *10* (4), 4364-4371.
29. Gargulak, J. D.; Lebo, S. E.; McNally, T. J., Lignin. In *Kirk-Othmer Encyclopedia of Chemical Technology*, John Wiley & Sons, Inc.: 2000.
30. Li, C.; Zhao, X.; Wang, A.; Huber, G. W.; Zhang, T., Catalytic Transformation of Lignin for the Production of Chemicals and Fuels. *Chemical Reviews* **2015**.
31. Fache, M.; Boutevin, B.; Caillol, S., Vanillin production from lignin and its use as a renewable chemical. *Acs Sustain Chem Eng* **2015**.
32. Katahira, R.; Mittal, A.; McKinney, K.; Chen, X.; Tucker, M.; Johnson, D. K.; Beckham, G. T., Base-catalyzed depolymerization of biorefinery lignins. *Acs Sustain Chem Eng* **2016**.
33. Liu, Q.; Wang, S.; Zheng, Y.; Luo, Z.; Cen, K., Mechanism study of wood lignin pyrolysis by using TG–FTIR analysis. *J Anal Appl Pyrol* **2008,** *82* (1), 170-177.
34. http://www.lignotech.com/.
35. Mullen, C. A.; Boateng, A. A., Catalytic pyrolysis-GC/MS of lignin from several sources. *Fuel Process Technol* **2010,** *91* (11), 1446-1458.
36. Demir-Cakan, R.; Baccile, N.; Antonietti, M.; Titirici, M.-M., Carboxylate-rich carbonaceous materials via one-step hydrothermal carbonization of glucose in the presence of acrylic acid. *Chemistry of Materials* **2009,** *21* (3), 484-490.
37. Gonen, M.; Nyankson, E.; Gupta, R. B., Boric acid production from colemanite together with ex-situ CO2 sequestration. *Ind Eng Chem Res* **2016**.
38. Ramsurn, H.; Kumar, S.; Gupta, R. B., Enhancement of biochar gasification in alkali hydrothermal medium by passivation of inorganic components using Ca (OH) 2. *Energy & Fuels* **2011,** *25* (5), 2389-2398.
39. Xie, Q. X.; Bao, R. R.; Zheng, A. R.; Zhang, Y. F.; Wu, S. H.; Xie, C.; Zhao, P., Sustainable Low-Cost Green Electrodes with High Volumetric Capacitance for Aqueous Symmetric Supercapacitors with High Energy Density. *Acs Sustain Chem Eng* **2016,** *4* (3), 1422-1430.
40. Long, C. L.; Jiang, L. L.; Wu, X. L.; Jiang, Y. T.; Yang, D. R.; Wang, C. K.; Wei, T.; Fan, Z. J., Facile synthesis of functionalized porous carbon with three-dimensional interconnected pore structure for high volumetric performance supercapacitors. *Carbon* **2015,** *93*, 412-420.
41. Zuo, Z. C.; Li, W.; Manthiram, A., N-heterocycles tethered graphene as efficient metal-free catalysts for an oxygen reduction reaction in fuel cells. *J Mater Chem A* **2013,** *1* (35), 10166-10172.
42. Wang, L.; Zheng, Y. L.; Zhang, Q. Y.; Zuo, L.; Chen, S. L.; Chen, S. H.; Hou, H. Q.; Song, Y. H., Template-free synthesis of hierarchical porous carbon derived from low-cost biomass for high-performance supercapacitors. *Rsc Adv* **2014,** *4* (93), 51072-51079.

43. Gu, W. T.; Sevilla, M.; Magasinski, A.; Fuertes, A. B.; Yushin, G., Sulfur-containing activated carbons with greatly reduced content of bottle neck pores for double-layer capacitors: a case study for pseudocapacitance detection. *Energ Environ Sci* **2013,** *6* (8), 2465-2476.
44. Sevilla, M.; Mokaya, R., Energy storage applications of activated carbons: supercapacitors and hydrogen storage. *Energ Environ Sci* **2014,** *7* (4), 1250-1280.
45. Huang, C.-h.; Doong, R.-a.; Gu, D.; Zhao, D., Dual-template synthesis of magnetically-separable hierarchically-ordered porous carbons by catalytic graphitization. *Carbon* **2011,** *49* (9), 3055-3064.
46. Sevilla, M.; Fuertes, A. B., Catalytic graphitization of templated mesoporous carbons. *Carbon* **2006,** *44* (3), 468-474.
47. Ma, G.; Yang, Q.; Sun, K.; Peng, H.; Ran, F.; Zhao, X.; Lei, Z., Nitrogen-doped porous carbon derived from biomass waste for high-performance supercapacitor. *Bioresource Technology* **2015,** *197*, 137-142.
48. Fiset, E.; Bae, J.-S.; Rufford, T. E.; Bhatia, S.; Lu, G. Q.; Hulicova-Jurcakova, D., Effects of structural properties of silicon carbide-derived carbons on their electrochemical double-layer capacitance in aqueous and organic electrolytes. *J Solid State Electr* **2013,** *18* (3), 703-711.
49. Demir, M.; Kahveci, Z.; Aksoy, B.; Palapati, N. K.; Subramanian, A.; Cullinan, H. T.; El-Kaderi, H. M.; Harris, C. T.; Gupta, R. B., Graphitic Biocarbon from Metal-Catalyzed Hydrothermal Carbonization of Lignin. *Ind Eng Chem Res* **2015,** *54* (43), 10731-10739.
50. Sun, G.-w.; Wang, C.; Zhan, L.; Qiao, W.-m.; Liang, X.-y.; Ling, L.-c., Influence of high temperature treatment of activated carbon on performance of supercapacitors. *Mater. Sci. Eng* **2008,** *2*, 41-48.
51. Hulicova-Jurcakova, D.; Seredych, M.; Lu, G. Q.; Bandosz, T. J., Combined Effect of Nitrogen-and Oxygen-Containing Functional Groups of Microporous Activated Carbon on its Electrochemical Performance in Supercapacitors. *Adv Funct Mater* **2009,** *19* (3), 438-447.
52. Gharehkhani, S.; Shirazi, S. F. S.; Jahromi, S. P.; Sookhakian, M.; Baradaran, S.; Yarmand, H.; Oshkour, A. A.; Kazi, S. N.; Basirun, W. J., Spongy nitrogen-doped activated carbonaceous hybrid derived from biomass material/graphene oxide for supercapacitor electrodes. *Rsc Adv* **2015,** *5* (51), 40505-40513.
53. Hayes, W. I.; Joseph, P.; Mughal, M. Z.; Papakonstantinou, P., Production of reduced graphene oxide via hydrothermal reduction in an aqueous sulphuric acid suspension and its electrochemical behaviour. *J Solid State Electr* **2015,** *19* (2), 361-380.
54. Liu, C.; Hu, G.; Gao, H., Preparation of few-layer and single-layer graphene by exfoliation of expandable graphite in supercritical N, N-dimethylformamide. *The Journal of Supercritical Fluids* **2012,** *63*, 99-104.
55. Ai, L. H.; Liu, X. M.; Jiang, J., Synthesis of loofah sponge carbon supported bimetallic silver-cobalt nanoparticles with enhanced catalytic activity towards hydrogen generation from sodium borohydride hydrolysis. *J Alloy Compd* **2015,** *625*, 164-170.
56. Paraknowitsch, J. P.; Thomas, A.; Schmidt, J., Microporous sulfur-doped carbon from thienyl-based polymer network precursors. *Chem Commun* **2011,** *47* (29), 8283-8285.
57. Zhao, X.; Zhang, Q.; Chen, C.-M.; Zhang, B.; Reiche, S.; Wang, A.; Zhang, T.; Schlögl, R.; Su, D. S., Aromatic sulfide, sulfoxide, and sulfone mediated mesoporous carbon monolith for use in supercapacitor. *Nano Energy* **2012,** *1* (4), 624-630.
58. Chen, F.; Zhou, W. J.; Yao, H. F.; Fan, P.; Yang, J. T.; Fei, Z. D.; Zhong, M. Q., Self-assembly of NiO nanoparticles in lignin-derived mesoporous carbons for supercapacitor applications. *Green Chem* **2013,** *15* (11), 3057-3063.
59. Wang, K. L.; Cao, Y. H.; Wang, X. M.; Castro, M. A.; Luo, B.; Gu, Z. R.; Liu, J.; Hoefelmeyer, J. D.; Fan, Q. H., Rod-shape porous carbon derived from aniline modified lignin for symmetric supercapacitors. *J Power Sources* **2016,** *307*, 462-467.
60. Hu, S. X.; Zhang, S. L.; Pan, N.; Hsieh, Y. L., High energy density supercapacitors from lignin derived submicron activated carbon fibers in aqueous electrolytes. *J Power Sources* **2014,** *270*, 106-112.

61. Zhang, W. L.; Zhao, M. Z.; Liu, R. Y.; Wang, X. F.; Lin, H. B., Hierarchical porous carbon derived from lignin for high performance supercapacitor. *Colloid Surface A* **2015,** *484*, 518-527.
62. Li, H.; Yuan, D.; Tang, C. H.; Wang, S. X.; Sun, J. T.; Li, Z. B.; Tang, T.; Wang, F. K.; Gong, H.; He, C. B., Lignin-derived interconnected hierarchical porous carbon monolith with large areal/volumetric capacitances for supercapacitor. *Carbon* **2016,** *100*, 151-157.
63. Saha, D.; Li, Y. C.; Bi, Z. H.; Chen, J. H.; Keum, J. K.; Hensley, D. K.; Grappe, H. A.; Meyer, H. M.; Dai, S.; Paranthaman, M. P.; Naskar, A. K., Studies on Supercapacitor Electrode Material from Activated Lignin-Derived Mesoporous Carbon. *Langmuir* **2014,** *30* (3), 900-910.
64. (a) Zhao, H. B.; Wang, W. D.; Lu, Q. F.; Lin, T. T.; Lin, Q. L.; Yang, H. J., Preparation and application of porous nitrogen-doped graphene obtained by co-pyrolysis of lignosulfonate and graphene oxide. *Bioresource Technology* **2015,** *176*, 106-111; (b) Qiang, Y. W.; Jiang, J. G.; Xiong, Y. C.; Chen, H.; Chen, J. Y.; Guan, S. Y.; Chen, J. D., Facile synthesis of N/P co-doped carbons with tailored hierarchically porous structures for supercapacitor applications. *Rsc Adv* **2016,** *6* (12), 9772-9778.
65. Lee, M.; Kim, G. P.; Song, H. D.; Park, S.; Yi, J., Preparation of energy storage material derived from a used cigarette filter for a supercapacitor electrode. *Nanotechnology* **2014,** *25* (34).
66. Zhang, H.; Chen, J.; Li, Y.; Liu, P.; Wang, Y.; An, T.; Zhao, H., Nitrogen-Doped Carbon Nanodots@ Nanospheres as An Efficient Electrocatalyst for Oxygen Reduction Reaction. *Electrochimica Acta* **2015,** *165*, 7-13.
67. Zhang, H. M.; Chen, J. Y.; Li, Y. B.; Liu, P. R.; Wang, Y.; An, T. C.; Zhao, H. J., Nitrogen-Doped Carbon Nanodots@Nanospheres as An Efficient Electrocatalyst for Oxygen Reduction Reaction. *Electrochimica Acta* **2015,** *165*, 7-13.
68. Yang, L.; Jiang, S.; Zhao, Y.; Zhu, L.; Chen, S.; Wang, X.; Wu, Q.; Ma, J.; Ma, Y.; Hu, Z., Boron-Doped Carbon Nanotubes as Metal-Free Electrocatalysts for the Oxygen Reduction Reaction. *Angewandte Chemie* **2011,** *123* (31), 7270-7273.
69. Choi, C. H.; Chung, M. W.; Park, S. H.; Woo, S. I., Additional doping of phosphorus and/or sulfur into nitrogen-doped carbon for efficient oxygen reduction reaction in acidic media. *Phys Chem Chem Phys* **2013,** *15* (6), 1802-1805.
70. Zhang, L.; Niu, J.; Dai, L.; Xia, Z., Effect of Microstructure of Nitrogen-Doped Graphene on Oxygen Reduction Activity in Fuel Cells. *Langmuir* **2012,** *28* (19), 7542-7550.

5. Chapter 5. Conclusion and Future Direction

The energy storage or converting devices such as Li-ion batteries, supercapacitor, and fuel cell has been used to store or convert such energy electrochemically so that the supply and demand are matched. Thus, developing inexpensive, sustainable, high-performance, durable electro active materials are the main set of priorities for energy storage and fuel cell research. In this context, this dissertation attempted to develope advance carbon materials derived from low cost and sustainable biomass precursors. The as-prepared carbon materials have been evaluated in the application of Li-ion batteries, energy storage, and fuel cells. The results and contributions of the dissertation are condensed below, and certain personal opinions and recommendations for future work are also provided.

The second chapter was targeted to develop lignin-derived carbon using a transitional metal as a supporting catalyst in relatively low temperature. The following outcomes were reported in this chapter. It was shown that byproduct lignin is successfully converted into porous carbon via simple and green method via hydrothermal carbonization (HTC) process following by annealing treatment. The as-prepared graphitic carbon exhibited micro/mesoporosity along with the BET surface area that was up to 256 m^2/g. Also, resulting carbon exhibits high electrical conductivity facilitating the rapid movement of electrons which can be utilized in anode material for Li-ion batteries. It is hypothesized that the formation of high graphitization carbon is thanks to transition metal catalyst. Specifically, It was found that manganese based catalyst is favorable for a higher degree of graphitization due to the d-shell orbital which is capable of forming strong bonds between metal catalyst and carbon. In addition, the FeNO3 is more capable of forming the high surface area carbon with larger pore volume. In short, chapter 2 concluded that the obtained lignin-

derived graphitic carbon exhibits high electrical conductivity which can be used for anode material for Li-ion batteries and can be extended other energy storage/conversion technology application.

Supercapacitors drastically enhance the energy density of traditional capacitors and offer practical solutions to energy storage and transfer problems in the system. This chapter attempted to modify energy storage materials in an effort to increase the specific capacitance of recent supercapacitor electrodes. In addition, the aim of this section was to illustrate the positive effect of nitrogen doping on lignin-derived biochar. With this aims, the following scientific outcomes were reported in chapter three. The HTC and annealing treatment has been found as versatile methods to develop nitrogen-doped carbon materials. The as-synthesized N-doped carbon reached a capacitance of 440 F/g at 1 mV s^{-1} scan rate and demonstrated excellent cyclic stability over 30000 cycles in 1 M KOH 267 F g^{-1}. It is hypothesized that the induced specific capacitance is due to two different phenomena. One contributor arises from the BET surface area -as high as 2957 m^2/g- with micro/meso pore structure which responsible for the charge accumulation, the role of decreasing the ion diffusion distance and in charge of ion-buffering reservoirs to store more electrolyte ions on the surface. The second contributor caused by a combination of EDLC with pseudo-capacitor which adds extra electrolyte storage in the surface. It has been thereby concluded that the proposed methodology offers a more efficient and economical utilization of lignin, and resulting N-doped carbon can be readily applied in the energy storage technology.

The primary objective of chapter 4 is to exploit the unique structural, surface and electronic properties of sulfur-doped carbon and reduced or eliminated Pt dependence catalyst for fuel cells. The following scientific outcomes were reported in this chapter, we have shown that sulfur self-doped carbon materials were successfully synthesized from commercially available lignin via hydrothermal carbonization followed by thermal annealing. The as-prepared SC-850 sample

exhibits the high BET surface area (660 m^2/g) with abundant micro/meso porous structure. The SC-850 demonstrates an excellent capacitive behavior of 225 F/g at 0.5 A/g current density in 1.0 M KOH) and high durability up to 10,000 cycles at a harsh condition of 5 A/g current density. Furthermore, the SC-850 exhibited a well-defined cathodic peak and high electrochemical activity toward the ORR process in 0.1 M KOH electrolyte. It is hypothesized that excellent performance of S-doped carbon as an electrode and ORR catalyst caused by electron distribution of sulfur molecules in the carbon framework.

Collectively, this thesis systematically unveils simple and effective strategies to achieve high-performance carbon materials derived from byproduct lignin. The obtained carbon materials were tested for Li-ion batteries, supercapacitors, and fuel cell.

Recommendations for future work

Several results reported here need further investigation for commercializing of lignin-derived carbon materials. Future work can potentially encompass the following suggestions;

- Investigate the recovery of metal nitrate catalyst after the graphitization.
- Investigate the effect of different metal nitrate ratios in bio-char/graphitic carbon in order to enhance the degree of graphitization.
- Investigate the duel hetero-doped atom effect which potentially may improve electrochemical activity for supercapacitor electrode and the ORR electrocatalyst. This will be in an effort to tailor the specific structural, electronic and atomic properties of the carbon framework in order to obtain a higher electrochemical activity.
- Investigate electrochemical activity of N-doped carbon in the acidic media.
- Investigate electrochemical activity of N-doped carbon in two electrode cell.

- Investigate the durability testing in order to investigate the stability of S-doped carbons toward the ORR in fuel cell systems. This will provide further insight into their applicability as cathodic electrocatalysts and moreover will elucidate potential degradation mechanisms.

6.1. Vita

Muslum Demir was born on April 24, 1987, in Nizip-Gaziantep-Turkey. He is originally Turkish citizen. He graduated from Yahya Altinbas High School in Nizip in 2004. He received his Bachelor of chemistry from the university of Cukurova, Adana Turkey in 2008. She received a Master of Chemistry from Rutgers University in 2013.

Publications:

1. **Demir, M**.; Gupta, R. B., *Carbonization methods of Lignin*" **Book chapter (invited)**
2. **Demir, M**.; Farghaly, Matthew J. Decuir, Sushil Kumar Saraswat, Collinson, M,; Gupta, R. B.,"*Supercapacitive and Oxygen Reduction Characteristics of the Sulfur Self-doped Carbon Derived from Lignin*" submitted)
3. Ashourirad, B.; **Demir, M**.; Gupta, R. B.; El-Kaderi.; '*Facile Synthesis of N-Doped Porous Carbons by $ZnCl_2$Activation of Inexpensive Organic Building Blocks and their Performance as Supercapacitor*' (submitted)
4. **Demir, M**.; Aksoy, B.; Palapati, N. K.; Subramanian, A.; Cullinan, H. T.; El-Kaderi, H. M.; Harris, C. T.; Gupta, R. B.,"*Lignin Biomass-derived N-doped Graphitic Carbon Electrode Material for Supercapacitors*" submitted (under correction)
5. Nyankson, E, **Demir, M**,; Gonen M, Gupta, R. B., "*Interfacially-Active Hydroxylated Soybean Lecithin Dispersant for Crude Oil Spill Remediation*" ACS Sustainable and Engineering Chemistry Research, 2016
6. Palapati, N. K**; Demir[1], M**.; Subramanian, A.;Gupta, R. B., '*Enhancing the Electronic Conductivity of Lignin- sourced, Sub-micron Carbon particles'*, IEEE, Nanotechnology Materials and Devices, 2015.([1]Equal contribution)

7. **Demir, M**.; Kahveci, Z.; Aksoy, B.; Palapati, N. K.; Subramanian, A.; Cullinan, H. T.; El-Kaderi, H. M.; Harris, C. T.; Gupta, R. B., '*Graphitic bio-carbon from metal-catalyzed hydrothermal carbonization of lignin.*' ACS Industrial & Engineering Chemistry Research **2015**;
8. **Demir, M.;** McKee, M. L.; Samokhvalov, A., '*Interactions of thiophenes with C300 Basolite MOF in solution by the temperature-programmed adsorption and desorption, spectroscopy and simulations.*' Adsorption **2014,** *20* (7), 829-842.

Conferences/Presentations/Talks

1. **Demir, M**.; Gupta, R. B.,' *Synthesis of Biomass-Derived Carbon Materials and Their Application on Energy Storage and Fuel Cell*' Meet the faculty candidate session, AIChE Annual Meeting, San Francisco, CA; 2016
2. **Demir, M**.; Gupta, R. B.,' *Lecithin-Derived N-Doped Carbons for Supercapacitor Electrode material*', AIChE Annual Meeting, San Francisco, CA; 2016
3. **Demir, M**.; Gupta, R. B.,' *Sulfur Self-doped Micro/Mesoporous Carbon Derived Lignin and Its Application on Supercapacitor and Oxygen Reduction Reactionl*', AIChE Annual Meeting, San Francisco, CA; 2016
4. Aksoy, B**. Demir, M**.; Altay, B. Cullinan, H. T; Joyce, M.; Gupta, R. B., A sustainable lignin based graphitic bio-carbon for printed electronics, 2016 FLEX California.
5. **Demir, M**.; Islamoglu T..; Aksoy, B.;, A.; Cullinan, H. T.; El-Kaderi, H. M.; Harris, C. T.; Gupta, R. B.,N-Doped Material for Supercapacitor from Lignin Biomass, AICHE Annual Meeting, Salt Lake City; 11/2015
6. **Demir, M**.; Kahveci, Z.; Aksoy, B.; Palapati, N. K.; Subramanian, A.; Cullinan, H. T.; El-Kaderi, H. M.; Harris, C. T.; Gupta, R. B., Graphitic Bio-Carbon from Lignin Biomass Synthesized with

Nickel Nitrate Catalyst, 2015 AICHE Annual Meeting, Salt Lake City; 11/2015

7. **Demir, M**.; Kahveci, Z.; Aksoy, B.; Palapati, N. K.; Subramanian, A.; Cullinan, H. T.; El-Kaderi, H. M.; Harris, C. T.; Gupta, R. B., Graphitic Bio-Carbon from Lignin Biomass, 2015 ACS Annual Meeting, Denver CO; 03/2015